“Designer Synthesis of Monodisperse Heterodimer and Ferrite Nanoparticles”

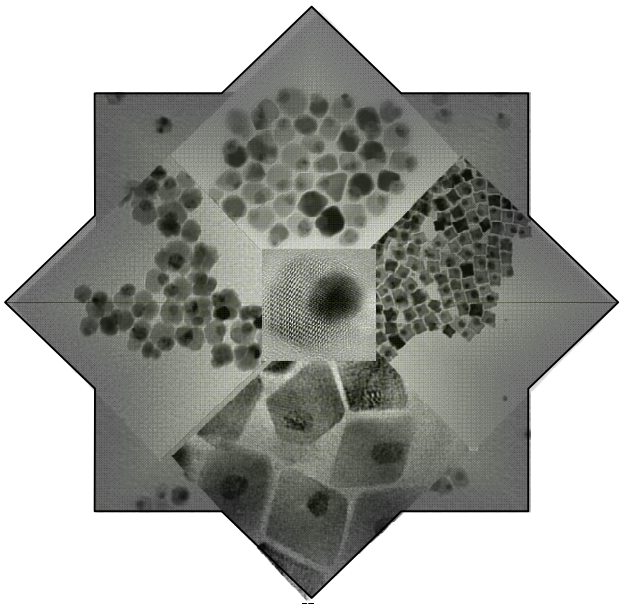

Dissertation

zur Erlangung des Grades
“Doktor der Naturwissenschaften”
Im Promotionsfach 09

am Fachbereich Chemie, Pharmazie und Geowissenschaften
der Johannes Gutenberg-Universität in Mainz

Bahar Nakhjavan, M.Sc.

geb. in Tehran, Iran

Mainz 2011

Abstract

The work presented in this doctoral thesis is a facile procedure, thermal decomposition, for the synthesis of different types of monodisperse heterodimer M@iron oxide (M= Cu, Co, Ni and Pt) and single ferrites, MFe_2O_4 (M= Cu and Co), nanoparticles. In the following chapter, we study the synthesis of these monodiperse nanoparticles with the similar iron precursor (iron pentacarbonyl) and different transition metal precursors such as metal acetate/acetylacetonate/formate precursors in the presence of various surfactants and solvents. According to their decomposition temperatures and reducing condition, a specific and suitable route was designed for the formation of Metal@Metal oxide or MFe_2O_4 nanoparticles (Metal/M=transition metal).

One of the key purposes in the formation of nanocrystals is the development of synthetic pathways for designing and controlling the composition, shape and size of predicted nanostructures. The ability to arrange different nanosized domains of metallic and magnetic materials into a single heterodimer nanostructure offers an interesting direction to engineer them with multiple functionalities or enhanced properties of one domain. The presence and role of surfactants and solvents in these reactions result in a variety of nanocrystal shapes. The crystalline phase, the growth rate and the orientation of growth parameters along certain directions of these structures can be chemically modulated by using suitable surfactants. In all novel reported heterodimer nanostructures in this thesis, initially metals were preformed and then by the injection of iron precursor in appropriate temperature, iron oxide nanoparticles were started to nucleate on the top or over the surfaces of metal nanoparticles. Ternary phases of spherical $Cu_xFe_{3-x}O_4$ and $CoFe_2O_4$ ferrites nanoparticles were designed to synthesis just by little difference in diffusion step with the formation of mentioned phase separated heterodimer nanoparticles. In order to use these magnetic nanoparticles in biomedical and catalysis applications, they should be transferred into the water phase solution, therefore they were functionalized by a multifunctional polymeric ligand. These functionalized nanoparticles were stable against aggregation and precipitation in aqueous media for a long time. Magnetic resonance imaging and catalytic reactivities are two promising applications which have been utilized for these magnetic nanoparticles in this thesis.

This synthetic method explained in the following chapters can be extended to the synthesis of other heterostructured nanomaterials such as Ni@MnO or M@M@iron oxide (M=transition metal) or to use these multidomain particles as building blocks for higher order structures.

Table of Content

1. Introduction

1.1. Nanotechnology

Nowadays scientists introduce nanotechnology as an interdisciplinary technology or science that can connect some scientific fields together such as chemistry, physics, material science and medicine [1-3]. Nanotechnology, one of the 21st century's most capable technologies, is playing a critical role in future technologies and addressing some of humanity's most difficult challenges e.g. environment, health and information storage [4-6]. This new technology can solve and answer to many questions inquired in regards to the dimension of materials. It involves the creation of material derived from the manipulation of particles as smaller than atoms. Manipulations of these microscopic particles allow scientists create all kinds of products that we use on a regular basis.

The two major approaches used in nanotechnology are called "bottom-up" and "top-down". In the "bottom-up" approach, materials and devices are built from molecular components that assemble themselves chemically by the principles of molecular recognition or chemical reaction. By using this method, researchers can synthesize nanoparticles in uniform size and shape, whereas this property does not achieve easily by the "top-down" method. In the "top-down" approach, nanoobjects are made from larger entities with various physical techniques [7].

Recently, nanochemists have been involved in a wide variety of nanotechnology including the synthesis of inorganic, organic and hybrid nanomaterials for use in nanodevices, the development of novel nano analytical techniques, the manipulation of biological molecules such as DNA and the evolution of molecular machines. The most studied research in chemistry already involves the control of nanodimensional objects and the self-assembly of molecules into larger structures.

Nanomaterials are defined as substances with at least one dimension in the size of nanometer (1 nm = 10^{-9} m) (Figure 1.1). One of the most important achievements in the nanometer scale is the development of these novel materials including their applications in a vast area due to their unique optical, magnetic, or electrical properties.

Nanoparticles exhibit unexpected, novel and unique physical and chemical properties due to their size and a large surface area in comparison to the constant physical properties of bulk material. The design and synthesis of novel nanoscale-engineered structures with a narrow

size distribution is a new scientific approach absorbing great interests due to their unique quantum size dependent properties [8]. One of the most important factors for the change in the physical and chemical properties of these small particles is the increased fraction of the surface atoms, which occur under special conditions (coordination number, symmetry of the local environment, etc.) differing from their bulk material counterparts.

Among the most widely used magnetic materials, ferrite/iron oxide particles in nano regime have been intensively pursued, not only for their special properties due to their low cost and high performance, but also for their many technological applications including magnetic fluids, catalysis, biotechnology/biomedicine, magnetic resonance imaging and data storage [9-13].

In spite of the advantages of nanoparticles, they have also shown some limitations. Their small size and large surface area can lead to particle agglomeration, which make physical manipulation of nanoparticles difficult in liquid and dry forms. For example, these small particles can result in limited drug loading and burst release in biomedicine application. In order to overcome these practical problems, we need to extend our research studies in this field before these nanoparticles can be used clinically or made commercially available.

This introduction focuses on the magnetic nanoparticles, different methods of synthesis, crystal formation mechanism and their specific application in magnetic resonance imaging as a contrast agent and in valuable chemical reactions as a catalyst.

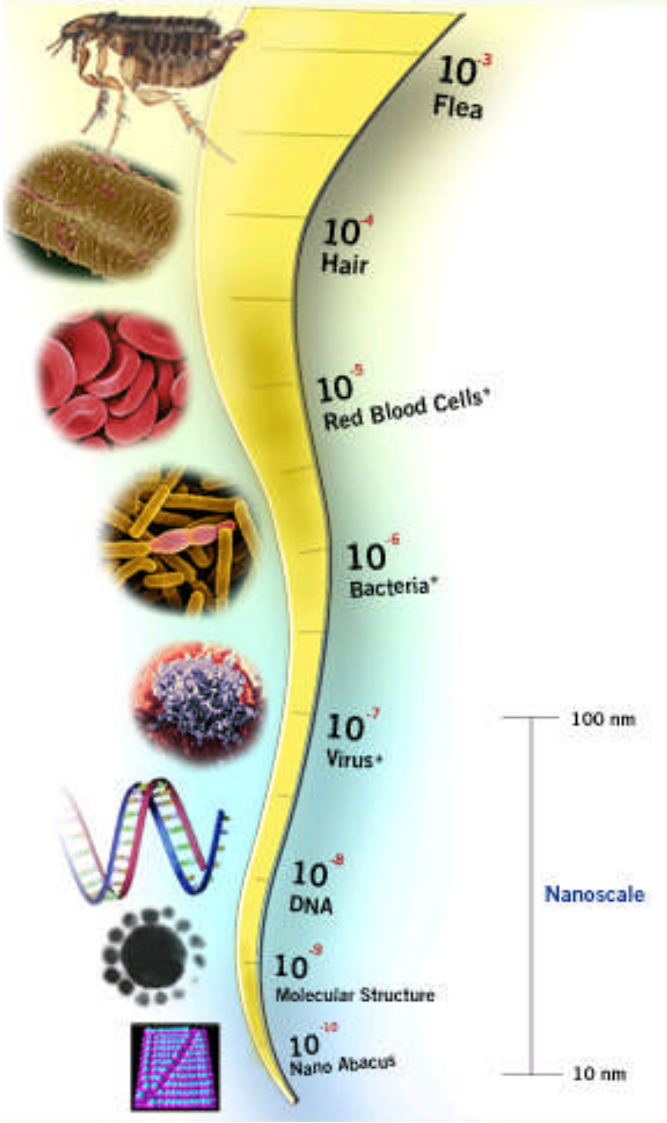

Figure 1.1. *Size comparison between naturally and artificially engineered materials.*

1.2. Magnetic Nanoparticles

Magnetic nanoparticles displaying a variety of unique magnetic phenomena that are drastically different from those of their bulk counterparts, are garnering significant interest since these properties can be advantageous for utilization in a variety of applications ranging from storage media for magnetic memory devices to probes and vectors in the biomedical sciences. Studying the magnetic properties of nanoparticles is interesting in view of both practical applications and fundamental understanding of magnetism. In the nanometer regime, the magnetic properties depend on the size of nanoparticles. Surface effects are also more

important than in the bulk due to a much larger surface-to-volume ratio. Therefore, magnetic nanoparticles are also an ideal system to study finite-size and surface effects, all of them yielding new phenomena and enhanced properties with respect to their bulk counterpart [14].

Their essential magnetic properties such as blocking temperature (T_b), spin lifetime (τ), coercivity (H_c) and susceptibility (χ) are strongly influenced by the nanoscaling laws and consequently, these scaling relationships can be leveraged to control magnetism from the ferromagnetic to the superparamagnetic regimes. Simultaneously, they can be used in order to tune magnetic values including H_c, χ and remanence (M_r). For example, the lifetime of magnetic spin is directly related to the magnetic anisotropy energy (K_uV) and also the size and volume of nanoparticles. Therefore, the nanoscaling laws of magnetic nanoparticles are important not only for understanding the behavior of existing materials but also for developing novel nanomaterials with advanced properties. These magnetic properties can be affected by many recognized factors such as chemical composition, type and degree of defectiveness in crystal lattice, particle size and shape, the morphology (for structurally in homogeneous particles), the interaction of the particle with the surrounding matrix and the neighboring particles.

1.3. Ferrites Nanoparticles

The existence of magnetic elements, Fe, Co, Ni and their derivatives in a complex or compound can cause magnetic properties in a magnetic field due to their spin orientation. By decreasing the size of magnetic materials or structures to nanoscale, they show a whole range of paramount properties because of reduced dimension. Ferrites nanoparticles are playing increasingly important roles in biotechnology and biomedicine. They have been used as carriers for magnetic drug targeting, as tags for biomolecular sensors, in biomolecule separation and purification, as well as for in vivo imaging and hyperthermia treatment. As these and other applications become more advanced, the precise control over particle composition, stability and surface functionality is crucial.

The ferrites materials with general formula MFe_2O_4 have attracted so much attention due to their various applications [15]. By adjusting and replacing different M^{2+}cations in this structural formula, the magnetic configurations of the spinel-type MFe_2O_4 can create a wide range of superior magnetic properties [16]. Various compositions of nanoferrites such as Fe_3O_4 [17], $NiFe_2O_4$ [18], $CoFe_2O_4$ [19], $ZnFe_2O_4$ [20], $CuFe_2O_4$ [21] and $MnFe_2O_4$ [22] have demonstrated interesting and attractive potential properties which is concerned to diffusion of

each metal in ferrite crystal structures. In the normal spinel structure, the oxygen ions form a cubic close packed structure. Half of the octahedral sites are occupied by the trivalent ions and one fourth of the tetrahedral sites by the divalent ions. In inverse spinels, the divalent ions switch places with the equivalent number of trivalent ions. Hence, one fourth of both the tetrahedral and the octahedral sites are occupied by the trivalent ions and another fourth of the octahedral sites by the divalent ions.

1.4. Magnetic Heterodimer Nanoparticles

Heterodimer nanoparticles are composed of two nano components with distinctive surfaces. They can be formed in different shapes and morphology such as core-shell [23], dumbbell-like [24], nanorod [25], nanocorn [26] and etc. The synthesis of heterodimer nanoparticles builds upon the extensive knowledge accumulated on the controlled synthesis of single component nanocrystals. However, new properties can be attained by combining several materials on the same nanosystem, where due to the small size, the effect of synergetic properties of the separate components may become a dominant factor. For example, the optical and electronic properties of these multicomponent nanostructures often show interesting deviations from their single components, such as a shift in the plasmon resonance of noble metal nanocrystals or a decrease in the photoluminescence intensity of semiconductor nanocrystals. Figure 1.2 shows a gallery of heterodimer nanoparticles combing different material components into the same structure reported in this doctoral thesis.

In order to achieve magnetic heterodimer nanoparticles, the presence of only one magnetic component can create this property in these nanostructures. Magnetite (Fe_3O_4), hematite (α-Fe_2O_3), maghemite (Fe_2O_3, γ-Fe_2O_3) are the common iron oxides nanoparticles and important classes of half metallic nanomaterials that in combination with nano transition metals have been synthesized and used in multifunctional applications in recent years.

Furthermore, functionalized magnetic nanoparticles are very promising candidates for application in magnetic resonance imaging, catalysis, biolabeling and bioseparation.

Today, there are several chemical synthetic methods available to produce magnetic nanostructures with different size, shape and compositions [27].

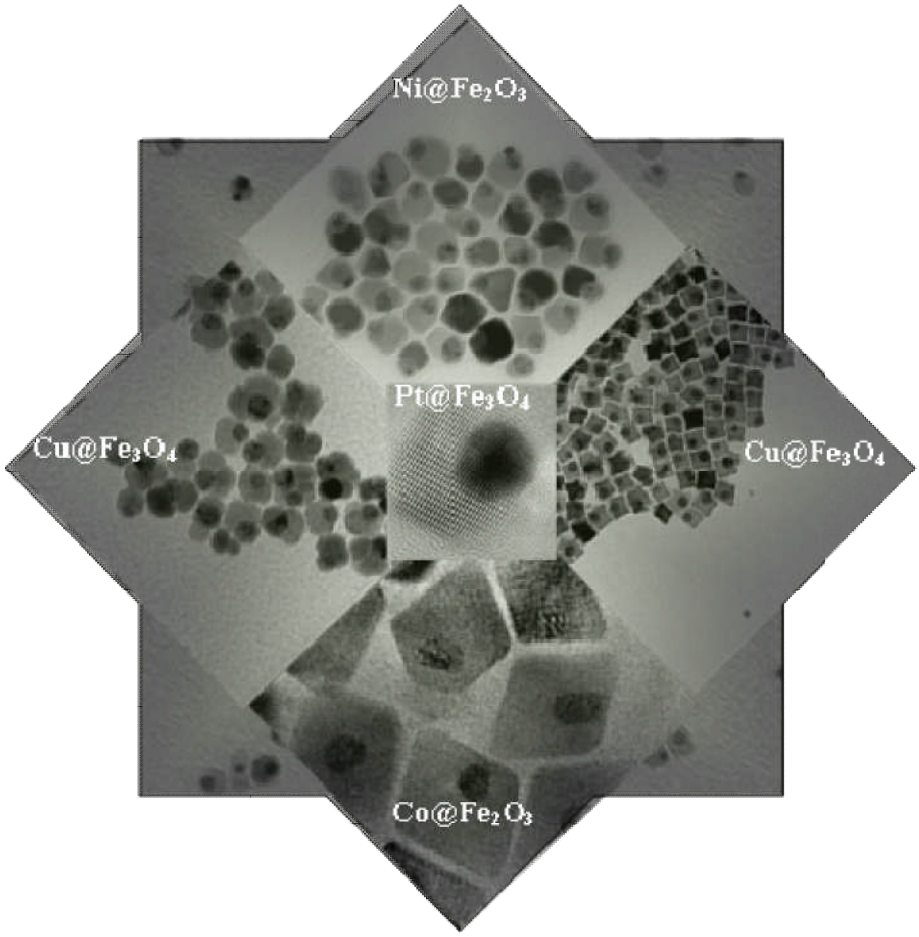

Figure 1.2. *A gallery of heterodimer nanoparticles including $Cu@Fe_3O_4$, $Co@Fe_2O_3$, $Ni@Fe_2O_3$ and $Pt@Fe_3O_4$.*

1.5. Synthesis of Magnetic Nanoparticles

The importance of this topic becomes obvious by a quick look at the number of publications concerning to these materials in recent years. The development of magnetic nanomaterials is based on the necessity of novel synthesizing techniques that can form these structures in different shape, size and morphology. Magnetic nanoparticles have been synthesized in different phases, forms and with numerous compositions. Thermal decomposition, co-precipitation, microemulsion and hydrothermal procedures are some popular methods, which have been developed, for the synthesis of iron oxides, pure metal, spinel-type ferromagnets and alloys in the last couple of years.

Shape-controlled, well-defined, high stability and monodispersity are essential parameters that researchers follow in these reactions. A successful synthesis depends on the correct

knowledge and precise understanding of the reaction mechanism. Controlling the reaction condition and manipulating the reaction chemistry are the most promising factors that can create a predicted nanostructure. In addition, it is very important to mention that the synthetic procedures should be relatively simple, inexpensive and reproducible.

The synthesis of hybrid nanoparticles requires the combination of two or more dissimilar materials in one system. Therefore, the formation of these nanostructures requires more precise and detailed understanding of system synergetic properties comparing with single component nanoparticles. In synthesis topic, some important concepts such as nucleation and growth should be emphasized because they can guide the formation of nanostructures with specific size and shape.

1.5.1. Thermal Decomposition

Monodisperse magnetic nanocrystals with smaller size can be synthesized through the thermal decomposition of organometallic compounds and metal surfactant compounds in high-boiling organic solvents containing stabilizing surfactants [28-30]. The popular precursors which generally have been used in this technique are metal acetylacetonates, [$M(acac)_n$], (M = Fe, Mn, Co, Ni, Cr; n = 2 or 3, acac = acetylacetonate) and metal cupferronates [M^xCup_x](M = metal ion; Cup = N-nitrosophenylhydroxylamine, $C_6H_5N(NO)O$-) or carbonyls [31, 32], whereas metal acetates, [$M(ac)_2$], (M = Cu, Co, Ni) have mostly been applied in my thesis. Fatty acids, oleic acid, oleylamine and hexadecylamine are frequently used surfactants [33]. The reaction temperature, reaction time and aging period are vital and essential criteria for a precise control of size and morphology by this method.

Thermal decomposition method is one of the most applicable procedures, which have often being used due to the high crystallinity, monodispersity and high dispersion properties of synthesized magnetic nanoparticles. In addition, this method has several advantages for theshaped controlled synthesis of nanoparticles including separation between nucleation and growth steps and facile controllability of growth parameters by variation of surfactant, solvent, monomer concentration and temperature.

1.5.2. Co-precipitation

One of the easy and recognized routes for producing iron oxides (either Fe_3O_4 or g-Fe_2O_3) from aqueous Fe^{2+}/Fe^{3+} salt solutions is co-precipitation by addition of a base under the inert atmosphere at room temperature or at higher temperature. In this method, the size, shape and

composition of the magnetic nanoparticles very much depends on the precursors and reaction condition such as salts (e.g. chlorides, sulfates, nitrates), the Fe^{2+}/Fe^{3+} ratio, the reaction temperature, the pH value and ionic strength of the media [27]. Reproducibility and simplicity are well-known advantages of this method introducing it into a high quality pathway. In order to reduce the polydispersity as negative phenomena in these reactions, one suitable surfactant or stabilizer should be used.

1.5.3. Microemulsion

A thermodynamically stable isotropic dispersion of two immiscible liquids is microemulsion, where an interfacial film of surfactant molecules stabilizes the microdomain of either or both liquids. Therefore, Spinel ferrites can be successfully synthesized in microemulsions and inverse micelles. For example, $MnFe_2O_4$ nanoparticles with controllable sizes from about 4–15 nm are synthesized through the formation of water-in-toluene inverse micelles with sodium dodecylbenzenesulfonate (NaDBS) as surfactant [34].

However, several kinds of magnetic nanostructres in different categories have been generated by this method and the results lead to the wide size distribution, variety of shapes and lower yield in comparison with other methods. Nowadays, microemulsion has not being used as a very popular system due to the large amount of required solvents and difficulties to scale-up.

1.5.4. Hydrothermal

Hydrothermal synthesis includes the various techniques of crystallizing substances from high-temperature aqueous solutions at high vapor pressures; it has also known as "hydrothermal method" [35]. Hydrothermal synthesis can be defined as a method of synthesis of single crystals that depends on the solubility of minerals in hot water and high pressure. A wide range of nanostructures with various properties can be produced under hydrothermal condition. This procedure is based upon a phase transfer and separation among liquid, solid and solution phases. Very narrow size distribution, well-controlled shape and simplicity are the major advantages of hydrothermal synthesis.

Up to now, magnetic nanostructures which have been formed by thermal decomposition and co-precipitation methods are the best candidates due to their unique and improved properties.

1.6. Formation Mechanism of Magnetic Nanoparticles

However, numerous chemical techniques have been developed to synthesize monodisperse nanoparticles, achieving a comprehensive understanding of the crystallization procedure (nucleation and growth), is still very challenging. A short burst of nucleation, subsequent slow controlled growth and separation between nucleation and growth steps are important parameters for synthesizing monodisperse nanoparticles. Therefore, studying in this area and obtaining enough information about them help the synthetic chemists to have control over the experiments. Herein, we discuss three key steps in the crystal formation mechanism.

1.6.1. Nucleation

LaMer and his colleagues pioneered in preparation of various oil aerosols and sulfur hydrosols and they studied and explained the concept of burst nucleation for the first time [36, 37]. In nucleation, many nuclei are formed simultaneously, and then these nuclei initiate to grow. The presence of “burst-nucleation” enabling a control of size distribution in particle formation is a vital point in synthesizing the monodisperse and highly uniform nanocrystals. In order to develop the synthetic techniques for crystallization of nanoparticles, one of homogeneous or heterogeneous nucleations occurs as an initial step.

In the homogeneous nucleation process, all nuclei emerge in a homogeneous solution at the same time and subsequent growth step will come without any additional nucleation. The separation between nucleation and growth processes leads to a homogeneous nucleation and then monodisperse nano-sized particles. Moreover, it should be mentioned that the required energy barrier for nucleation is high because of change phase from homogeneous to heterogeneous unexpectedly. In order to overcome this large energy barrier, a driving force such as high temperature, a strong reductant agent and supersaturated solution should exist in this condition.

The seed mediated growth is the popular method used in the crystal formation process, wherein the nucleation is physically separated from the growth by using preformed nanocrystals as seed nuclei. However, chemists prefer to use homogeneous nucleation due to the above reasons, seed mediated growth uses also heterogeneous nucleation to stop the formation of additional nuclei [38]. Preformed nuclei are injected into the reaction solution and then monomer start to precipitate on the surface of the existing nuclei in this method.

Hot injection and heating up methods are the techniques usually utilized for synthesizing

monodisperse nanocrystal with homogeneous nucleation [39, 28].

In the heterogeneous nucleation process, not all the nuclei start to form at the same time and in the same way. Therefore, they can result in different shape and size but if this procedure can be controlled and guided in correct conditions, it will create a wide range of hybrid or multicomponent structures such as core-shell nanocrystals.

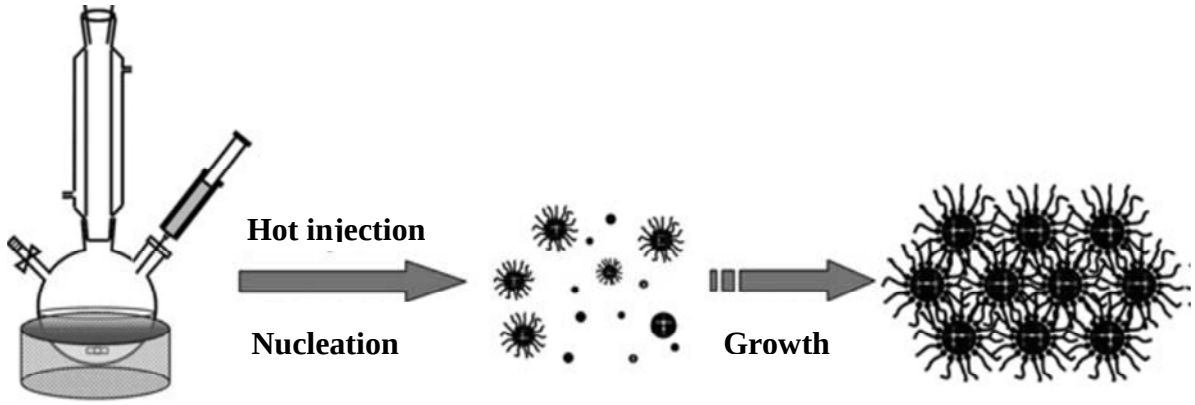

Figure 1.3. *Hot injection method showing nucleation and growth steps [40].*

1.6.2. Growth

Crystal growth is the second step of the crystallization process occurring subsequent to thenucleation step and generally without additional nucleation can create a narrow size distribution of the ensemble of nanoparticles. In this slower process, the elements generating the motif add to the growing crystal in a prearranged system (the crystal lattice). The growing step is continuing as long as the monomer solution is supersaturated.

Surface energy, growth rate, capping molecules and temperatures are important issues that affect on the growth process and subsequently the size and morphology of nanocrystals.

Nanocrystal growth can be explained by the following three significant stages: (1) a quick enhancement for monomer concentration in the reaction solution results in nuclei formation, (2) by an aggregation of monomer on the nuclei, crystal growth can start which cause the reduction of monomer concentration and (3) surface stabilization with suitable capping agents controls the physical properties in nanocrystals [41].

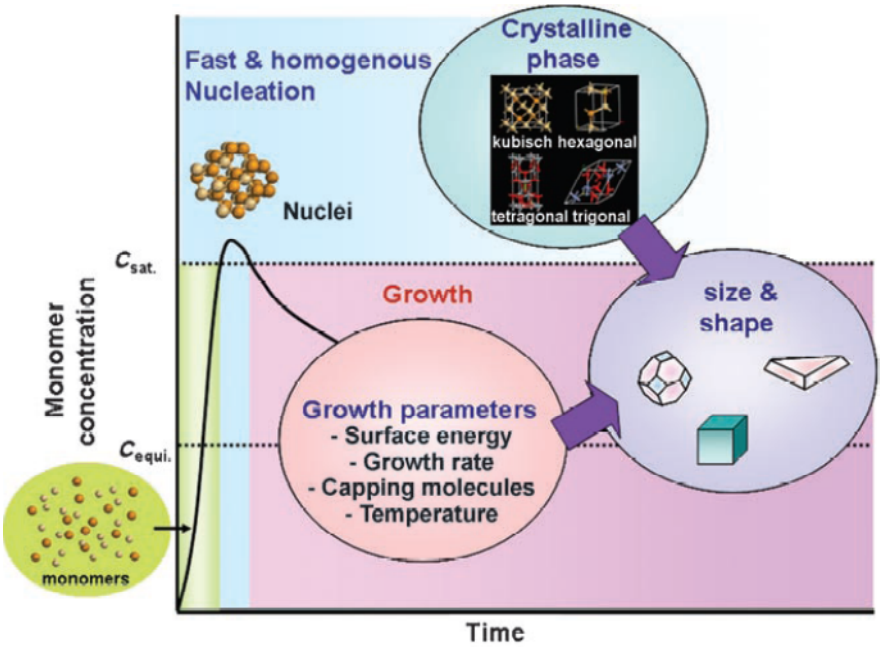

Figure 1.4. *Crystallization procedure including nucleation, growth and aging steps [41].*

1.6.3. Aging

The aging process is the following step coming after growth step to arrange the formation of crystal with specific size, shape and morphology. This last step can change the size distribution of generated nanocrystals and keep them in the same or even narrow size distribution.

In the aging stage, two main processes, Ostwald ripening and aggregation, may happen. Ostwald ripening is a physical phenomenon happening in duration of the crystallization process and can be very effective size, shape and even monodispersity of the samples [42, 43]. This process refers to the growth of larger crystals from those of smaller size that have a higher solubility than the larger ones [44, 45]. Aggregation of nanoparticles is where they stick together which is not generally desirable for synthetic chemists. However, if they can be oriented in the same direction, this step also will lead to the production of anisotropic nanoparticles (e.g., elongated particles) in the high yield and with size control. Oriented aggregation offers the potential to tune material properties by controlling defect concentrations, morphology, and size as well as size distribution [46, 47].

1.7. Applications of Magnetic Nanoparticles

Although there have been many significant developments in the synthesis and characterization of different structure magnetic nanoparticles, functionalization of these particles and keeping their solubility and stability for a long time without agglomeration or precipitation is an important issue in their application topic. A wide variety of applications has been envisaged for magnetic nanoparticles including catalysis, biomedicine, magnetic resonance imaging, data storage and etc. Since magnetic nanoparticles have unique magnetic properties and their size are comparable with biological important objects, they can be used in biomedical science especially in magnetic resonance imaging due to their response to external magnetic field [48, 49]. Catalytic activity of magnetic nanoparticles is one of the most active researches that has already pursued and showed great promises in the future [50, 51]. In this thesis, these two wide used applications have been studied for the synthesized magnetic nanoparticles.

1.7.1. Magnetic Nanoparticles in Magnetic Resonance Imaging

Magnetic resonance imaging (MRI) is a useful technique for analyzing the body tissue in the presence of an external magnetic field. This clinical method has developed by using some specific complexes [52] for improvement of diagnosis and therapy in patients. Initially, these drugs must enter to a patient body to make a contrast between normal and diseased tissue and secondly show the status of tissue functions or blood flow [53]. Today there are various contrast agents available which have been introduced as magnetic resonance imaging.

Commercially, gadolinium chelate complexes such as gadolinium diethylenetriaminepentaacetate (Gd-DTPA) are the most widely used in commercial MRI contrast agents [54]. Their main clinical applications are concerned with detecting changes in vascularity, flow dynamics and perfusion. Their limitations are very short blood circulation time and non-specific biodistribution. Nanoparticles can be employed to overcome these limitations. For example, the blood circulation times can be increased significantly by size control and surface modification of nanomaterials and by conjugating targeting molecules (e.g. antibodies or peptides) to their surface.

Manganese dipyridoxyldiphosphate, Mn-DPDP, is one of manganese chelates that can be used in magnetic resonance imaging as a contrast agent. In this case, the specific signal can be enhanced and have been used specifically for the detection of lesions and tumors. In order to identification these diseased tissue, Mn-DPDP effects on T_1 signal and consequently the enhancement of T_1 make the healthy tissue brighter [55].

There are two types of iron oxide contrast agents: Superparamagnetic Small Particles of Iron Oxide (SPIO) and Superparamagnetic Ultra Small Particles of Iron Oxide (USPIO). After injection of these magnetic materials to a specific tissue, the related signals can be reduced and then be monitored by the MRI instrument [56]. According to the iron concentration used in this measurement, signals can increase or decrease. These contrast agents have been used regularly for magnetic resonance imaging in comparison with other contrast agents.

Gd chelate and MnO nanoparticle based contrast agents accelerate the longitudinal (T_1) relaxation of water protons and therefore exhibit bright contrast [57, 58]. On the other hand, superparamagnetic Fe_3O_4 accelerate the transverse (T_2) relaxation of water protons and exhibit dark contrast [59].

The accurate imaging of medical targets becomes increasingly desirable for understanding metabolic processes and for a non-ambiguous diagnosis of diseases [60]. Therefore, one goal is to replace the current state-of-the-art single-modal imaging methods by multimodal imaging techniques. This could be achieved by combining different imaging methods such as magnetic resonance imaging (MRI)/positron emission tomography (PET), MRI/optical or PET/near-infrared optical fluorescence (NIRF) [61].

1.7.2. Magnetic Nanoparticles as Recycleable Catalysts

Catalysts are widely used in the large-scale manufacture of chemicals and in the production of fine chemicals and pharmaceuticals. One of the interesting scientific and technological challenges associated with the use of nanoparticles as catalysts is the understanding of how the composition and atomic-scale structure of nanoparticles produce the best catalytic activity. The second challenge is to synthesize these particles with maximum control over the composition and structure. Modern nanotechnology methods clearly offer great potential for future developments in both characterization and synthesis of heterogeneous catalysts based on supported nanoparticles. The enhancement of the surface to the volume area is not the only reason for using nanoparticles as heterogeneous catalysts.

Nowadays, magnetic nanoparticles with special properties such as good stability that they have shown will be great interest in catalysis application. They can be catalytically active for several chemical reactions and very useful to assist an effective separation of catalysts [62]. Magnetic nanoparticles especially with the core-shell morphology such as $Pt@Fe_2O_3$ NPs have been recognized as improved types of catalysts [63]. As an example, core-shell cobalt-platinum nanoparticles are superparamagnetic at room temperature and the magnetic core, Co,

can play the role of separation and recycling of catalyst, while platinum atoms are accessible for the reagents and responsible for hydrogenation of unsaturated organic molecules [64]. The presence of both catalytic and magnetic nanostructures in one nanostructure accelerates the quality and the quantity of reactions and also provides a suitable combination for catalytic activities [65].

1.8. References

[1] C. P. Collier, T. Vossmeyer and J. R. Heath, *Annu. Rev. Phys. Chem.***1998**, *49*, 371.

[2] M. Brust and C. J. Kiely, *Colloids Surf. A* **2002**, *202*, 175.

[3] E. V. Shevshenko, D. V. Talapin, N. A. Kotov, S. O'Brien and C. B. Murray, *Nature* **2006**, *439*, 55.

[4] J. Livage, M. Henry and C. Sanchez, *Prog. Solid State Chem.* **1988**, *18*, 259.

[5] W. L. Shi, Y. Sahoo, H. Zeng, Y. Ding, Z. L. wang, M. T. Swihart and P. N. Prasad, *Adv. Mater.* **2006**, *18*, 1889.

[6] S. A. Majetich and Y. Jin, *Sience* **1999**, *284*, 470.

[7] (a) G. Schmid, *Nanoparticles: From Theory to Application*; Wiley-VCH: Weinheim **2004**. (b) K. J. Klabunde, *Nanoscale Materials in Chemistry*; Wiley-Interscience: New York, **2001**. (c) A. L. Rogach, D. V. Talapin, E. V. Shevchenko, A. Kornowski, M. Hasse and H. Weller, *Adv. Funct. Master.* **2002**, *12*, 653.

[8] G. A. Ozin, *Adv. Mater.* **1992**, *4*, 612.

[9] S. Chikazumi, S. Taketomi, M. Ukita, M. Mizukami, H. Miyajima, M. Setogawa and Y. Kurihara, *J. Magn. Magn. Mater.* **1987**, *65*, 245.

[10] A.-H. Lu, W. Schmidt, N. Matoussevitch, H. Bonnermann, B. Spliethoff, B. Tesche, E. Bill, W. Kiefer and F. Schuth, *Angew. Chem.* **2004**, *116*, 4403; *Angew. Chem. Int. Ed.* **2004**, *43*, 4303.

[11] A. K. Gupta and M. Gupta, *Biomaterials* **2005**, *26*, 3995.

[12] S. Mornet, S. Vasseur, F. Grasset, P. Verveka, G. Goglio, A. Demourgues, J. Portier, E. Pollert and E. Duguet, *Prog. Solid State Chem.* **2006**, *34*, 237.

[13] T. Hyeon, *Chem. Commun.* **2003**, 927.

[14] X. Batlle and A. Labarta, *J. Phys D: Appl. Phys.* **2002**, *35*, R15.

[15] B. Nakhjavan, M. N. Tahir, H. Gao, K. Schneider, T. Schladt, F. Natalio, I. Ament, R. Branscheid, S. Weber, U. Kolb, C. Sönnichsen, L. M. Schreiber and W. Tremel, *J. Mater. Chem.* **2011**, *21*, 8605.

[16] U. Haefeli, W. Schuett, J. Teller and M. Zborowski, *Scientific and Clinical Applications of Magnetic Carriers*; Plenum: New York, **1997**.

[17] R. C. O' Handley, *Modern Magnetic Materials: Principles and Applications*; Wiley: New York, **2000**.

[18] V. Sepelak, I. Bergmann, A. Feldhoff, P. Heitjans, F. Krumeich, D. Menzel, F. J.

Litterst, S. J. Campbell and K. D. Becker. *J. Phys. Chem. C* **2007**, *111*, 5026.

[19] A. J. Rondinone, A. C. S. Samia and Z. J. Zhang, *J. Phys. Chem. B* **1999**, *103*, 6876.

[20] C. Yao, Q. Zeng, G. F. Goya, T. Torres, J. Liu, H. Wu, M. Ge, Y. Zeng, Y. Wang and J. Z. Jiang, *J. Phys. Chem. C* **2007**, *111*, 12274.

[21] B. Nakhjavan, M. N. Tahir, M. Panthöfer, H. Gao, T. D. Schladt, T. Gasi, V. Ksenofontov, R Branscheid, S. Weber, U. Kolb, L. M. Schreiber and W. Tremel, *J. Mater. Chem.* **2011**, *21*, 6901.

[22] J. Lee, Y.-M. Huh, Y. Jun, J. Seo, J. Jang, H. Song, S. Kim, E. Cho, H. Yoon, J. Suh and J. Cheon, *Nat. Med.* **2007**, *13*, 95.

[23] J. L. Lyon, D. A. Fleming, M. B. Stone, P. Schiffer and M. E. Williams, *Nano Lett.* **2004**, *4*, 719.

[24] T. Mokari, E. Rothenberg, I. Popov, R. Costi and U. Banin, *Science* **2004**, *304*, 1787.

[25] S. Kudera, L. Carbone, M. F. Casula, R. Cingolani, A. Falqui, E. Snoeck, W. J. Parak and L. Manna, *Nano Lett.* **2005**, *5*, 445.

[26] T. Teranishi, Y. Inoue, M. Nakaya, Y. Oumi and T. Sano, *J. Am. Chem. Soc.* **2004**, *126*, 9914.

[27] A.-H. Lu, E. L. Salabas and F. Schüth, *Angew. Chem. Int. Ed.* **2007**, *46*, 1222.

[28] J. Park, K. An, Y. Hwang, J.-G. Park, H.-J. Noh, J.-Y. Kim, Park, N.-M. Hwang and T. Hyeon, *Nat. Mater.* **2004**, *3*, 891.

[29] S. Sung, H. Zeng, D. B. Robinson, S. Raoux, P. M. Rice, S. X. Wang and G. Li, *J. Am. Chem. Soc.* **2004**, *126*, 273.

[30] F. X. Redl, C. T. Black, G. C. Papaefthymiou, R. L. Sandstorm, M. Yin, H. Zeng, C. B. Murray and S. P. O'Brien, *J. Am. Chem. Soc.* **2004**, *126*, 14583.

[31] J. Rockenberger, E. C. Scher and A. P. Alivisatos, *J. Am. Chem. Soc.* **1999**, *121*, 11595.

[32] D. Farrell, S. A. Majetich and J. P. Wilcoxon, *J. Phys. Chem. B* **2003**, *107*, 11022.

[33] N. R. Jana, Y. Chen and X. Peng, *Chem. Mater.* **2004**, *16*, 3931.

[34] C. Liu, B. Zou, A. J. Rondinone and Z. J. Zhang, *J. Phys. Chem. B* **2000**, *104*, 1141.

[35] H. Deng, X. Li, Q. Peng, X. Wang, J. Chen and Y. Li, *Angew. Chem.* **2005**, *117*, 2841; *Angew. Chem. Int. Ed.* **2005**, *44*, 2782.

[36] V. K. LaMer and R. H. Dinegar, *J. Am. Chem. Soc.* **1950**, *72*, 4847.

[37] T. Sugimoto, *Adv. Colloid Interface Sci.* **1987**, *28*, 65.

[38] (a) N. R. Jana, L. Gearheart and C. J. Murphy, *Chem. Master.* **2001**, *13*, 2313. (b) H. Yu, P. C. Gibbons, K. F. Kelton and W. E. Buhro, *J. Am. Chem. Soc.* **2001**, *123*, 9198.

[39] D. V. Talapin, A. L. Rogach, A. Kornowski, M. Hasse and H. Weller, *Nano lett.* **2001**, *1*, 207.

[40] J. Park, J. Joo, S. Kwon, Y. Jang and T. Hyeon, *Angew. Chem. Int. Ed.* **2007**, *46*, 4630.

[41] Y. Jun, J. Choi and J. Cheon, *Angew. Chem. Int. Ed.* **2006**, *45*, 3414.

[42] H. G. Yang and H. C. Zeng, *J. Phys. Chem. B* **2004**, *108*, 3492.

[43] B. Liu and H. C. Zeng, *Small* **2005**, *1*, 566.

[44] W. Z. Ostwald, *Phys. Chem.* **1897**, *22*, 289.

[45] W. Z. Ostwald, *Phys. Chem.* **1900**, *34*, 495.

[46] V. M. Yumono, N. D. Burrows, J. A. Soltis and R. L. Penn, *J. Am. Chem. Soc.* **2010**, *132*, 2163.

[47] R. L. Penn, J. J. Erbs and D. M. Gulliver, *J. Cryst. Growth* **2006**, *293*, 1.

[48] S. Mornet, S. Vasseur, F. Grasset, P. Verveka, G. Goglio, A. Demourgues, J. Portier, E. Pollert and E. Duguet, *Prog. Solid state Chem.* **2006**, *34*, 237.

[49] Z. Li, L. Wie, M. Y. Gao and H. Lei, *Adv. Mater.* **2005**, *17*, 1001.

[50] A.-H. Lu, W. Schmidt, N. Matoussevitch, H. Bonnermann, B. Spliethoff, B. Tesche, E. Bill, W. Kiefer and F. Schuth, *Angew. Chem.* **2004**, *116*, 4403; *Angew. Chem. Int. Ed.* **2004**, *43*, 4303.

[51] S. C. Tsang, V. Caps, I. Paraskevas, D. Chadwick and D. Thompsett, *Angew. Chem.* **2004**, *116*, 5763; *Angew. Chem. Int. Ed.* **2004**, *43*, 5645.

[52] J. Kim, Y. Piao and T. Hyeon, *Chem. Soc. Rev.* **2009**, *38*, 372.

[53] Y. Ayant, E. Belorizky, J. Alizon and J. Gallice, *J. Phys.* **1975**, *A36*, 991.

[54] A. Kawamata, Z. X. Na and Y. Fujiki, *Oral. Radiol.* **1992**, *8*, 111.

[55] M. G. Harisinghani, K. S. Jhavery, R. Weissleder, W. Schima, S. Saini, P. F. Hahn and P. R. Mueller, *Clinical Radiology* **2001**, *56*, 714.

[56] H. Nakamura, N. Ito, F. Kotake, Y. Mizokami and T. Matsuoka, *J. Gastroenterol.* **2000**, *35*, 849.

[57] P. Caravan, J. J. Ellison, T. J. McMurry and R. B. Lauffer, *Chem. Rev.* **1999**, *99*, 2293.

[58] H. B. Na, J. H. Lee, K. An, Y. I. Park, M. Park, I. S. Lee, D.-H. Nam, S. T. Kim, S.-H. Kim, S.-W. Kim, K.-H. Lim, K.-S. Kim, S.-O. Kim and T. Hyeon, *Angew. Chem. Int. Ed*. **2007**, *46*, 5397.

[59] M. H. Mendonca Dias and P. C. Lauterbur, *Magn. Reson. Med.* **1986**, *3*, 328.

[60] T. F. Massoud and S. S. Gambhir, *Gene. Dev*. **2003**, *17*, 545.

[61] J. S. Choi, J. C. Park, H. Nah, S. Woo, J. Oh, K. M. Kim, G. J. Cheon, Y. Chang, J. Yoo

and J. Cheon, *Angew. Chem. Int. Ed.* **2008**, *47*, 6259.

[62] S. Giri, B. G. Trewyn, M. P. Stellmaker and V. S.-Y. Lin, *Angew. Chem.* **2005**, *117*, 5166; *Angew. Chem. Int. Ed.* **2005**, *44*, 5038.

[63] X. Teng, D. Black, N. J. Watkins, Y. Gao and H, Yang, *Nano Lett.* **2003**, *3*, 261.

[64] J.-I. Park and J. Cheon, *J. Am. Chem. Soc.* **2001**, *123*, 5743.

[65] R. B. Bedford, M. Betham, D. W. Bruce, S. A. Davis, R. M. Frost and M. Hird, *Chem. Commun.* **2006**, 1398.

1.9. Objectives of Thesis

The design, synthesis and properties of magnetic nanoscale-engineered advanced materials and supramolecular systems have been of much interest due to their unusual structure and properties. Specially two or more than two components in one structure beside each other have shown some unique and interesting properties arising from interface interactions. Among these nanoparticles, ferrites and hybrid nanoparticles with the base of iron oxide exhibit an essential role due to their magnetic properties. Although there are numerous synthetic methods that have been applied for nanoparticles until now such as co-precipitation, hydrothermal and sol-gel, the thermal decomposition procedure reported here is well known as a simple, low cost and fast in comparison with the others.

Here in this thesis, we present some novel and unique single and heterodimer nanoparticles. They are $Cu@Fe_3O_4$ heterodimer nanoparticles in two forms, cube and cloverleaf shaped, monodisperse $Cu_xFe_{3-x}O_4$ nanoparticles, $Co@Fe_2O_3$ heteroparticles and the ternary phase $CoFe_2O_4$, heterodimeric dumbbell-like $Ni@Fe_2O_3$ and $Pt@Fe_3O_4$ nanoparticles. Afterward, they were functionalized by a multidentate copolymer carrying catechol anchor groups and PEG-linkers ($M_r \approx 800$) with free amino groups for further surface conjugation.

Due to their magnetic properties and solubility in physiological media, they have been used as novel contrast agents in magnetic resonace imaging or innovative catalysts in valuable reactions in this thesis.

1.10. Outline

Chapter 1 presents an introduction about nanotechnology and magnetic nanoparticles.

Chapter 2 presents the synthesis of $Cu@Fe_3O_4$ heteroparticles with distinct morphologies from organometallic reactants. They demonstrate magnetic and optical properties that are useful for simultaneous magnetic and optical detection. After functionalization, the $Cu@Fe_3O_4$ heterodimers can be used for the formation of nitric oxide (NO) and as contrast agents in MRI.

Chapter 3 reports the synthesis and functionalization of monodisperse copper ferrite $Cu_xFe_{3-x}O_4$ nanoparticles. These uniform and non-aggregated nanoparticles were synthesized by decomposing of two suitable precursors in convenient conditions. These $Cu_xFe_{3-x}O_4$ nanoparticles were functionalized by using hydrophilic polymeric ligand. Their stability and solubility in water solution over several weeks and fluorescent magnetic properties enables them to be applied in bioimaiging.

Chapter 4 demonstrates the synthesis of phase separated $Co@Fe_2O_3$ heteroparticles and the ternary phase $CoFe_2O_4$ by controlling the diffusion path in the nucleation step. Co and Fe_2O_3 domains can be functionalized selectively. We functionalized the NPs with a multidentate copolymer carrying catechol anchor groups and PEG-linkers ($M_r \approx 800$) with free amino groups for further surface conjugation. Moreover, They display magnetic properties that are useful for magnetic MRI detection.

Chapter 5 describes a facile synthesis of heterodimeric dumbbell-like $Ni@Fe_2O_3$ nanoparticles based on thermal decomposition method. Subsequently, the synthesis of these nanoparticles followed by the polymer functionalization. In addition, they can deactivate and remove environmental hazardous halogenated pollutants in the form of catalytic application.

Chapter 6 reports the simplified synthesis of monodisperse dumbbell-like $Pt@Fe_3O_4$ nanoparticles. Then, the surfactant molecules on the surface of nanoparticles were replaced by a multidentate copolymer. In order to use these nanoparticles in MRI scanner, magnetic resonance signals were measured and then showed a good contrast for aqueous solutions of functionalized nanoparticles.

Chapter 7 Conclusions and Outlook.

Chapter 8 Methods and Instrumentations.

Chapter 9 (appendix) presents a list of figures, a list of schemes, abbreviations and supplementary information.

2. Phase Separated $Cu@Fe_3O_4$ Heterodimer Nanoparticles from Organometallic Reactants

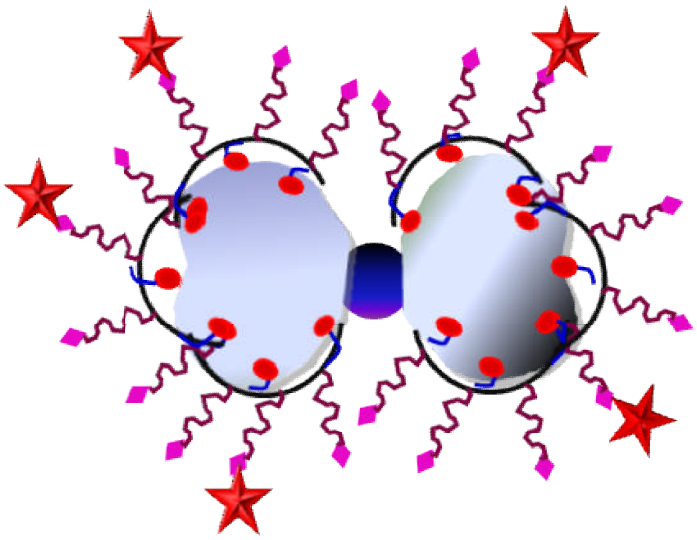

Bahar Nakhjavan[a], Muhammad Nawaz Tahir[a], Filipe Natalio[a], Haitao Gao[a], Kerstin Schneider[a], Thomas Schladt[a], Irene Ament[b], Robert Branscheid[b], Stefan Weber[c], Ute Kolb[b], Carsten Sönnichsen[b], Laura Maria Schreiber[c], Wolfgang Tremel[a*]

[a]Institut für Anorganische Chemie und Analytische Chemie, Johannes Gutenberg-Universität, Duesbergweg 10-14, D-55099 Mainz, Germany. Fax: +49 6131 39-25605; Tel: +49 6131 39-25135; E-mail: tremel@uni-mainz.de

[b]Institut für Physikalische Chemie, Johannes Gutenberg-Universität, Welderweg 11, 55099 Mainz, Germany.

[c]Bereich Medizinische Physik, Klinik und Poliklinik für diagnostische und interventionelle Radiologie, Klinikum der Johannes Gutenberg-Universität Mainz. Langenbeckstraße, 1, 55131, Mainz, Germany.

J. Mater. Chem. **2011**, *21*, 8605-8611

2.1. Introduction

The design, synthesis and properties of nanoscale engineered advanced materials and supramolecular systems have been of much interest due to their unusual structure and properties [1, 2]. Small metal or semiconductor particles have electronic and optical properties determined by the size of the particles and the extent of confinement of the valence electrons [3, 4]. Preparing metals or metal oxides in nanocrystalline form can lead to new physical properties and/or enhanced chemical reactivity [2]. The enhanced properties of nanocomposites over those expected from simple composite mixtures along with the short length scale of the particle size raises the interesting question of when does a nanocomposite become a new compound. To explore this question and to understand the relationships between properties and the size of crystallites it is necessary to prepare composites with a narrow crystallite sizes distribution and to explore how the physical and chemical properties change as a function of crystallite size.

A synthetic challenge is the preparation of nano engineered materials with controlled structures, e.g. with an anisotropic phase segregated structure [5] or a regular periodicity rather than with a broad range of interparticle distances. Artificially structured materials, including superlattices [6], multilayers [7, 8], amorphous alloys [9], quasicrystals [10], metastable crystalline alloys [11] or granular metals [12] have been extensively studied in recent years. These manmade solids contain intricate structures and extra degree of freedom, which can be exploited for fundamental studies and tailoring properties. In solid state science, such heterostructures with low impurity and defect densities, important parameters for device applications, are prepared using molecular beam epitaxy [7, 11].

In addition to vapor, deposition based synthetic approaches, chemists have developed a number of synthetic approaches to nanoscale materials by wet chemical methods [13, 14]. The strategy to stabilize these non-equilibrium phases is in most cases to gain kinetic control of the reaction by eliminating diffusion as a rate-limiting step. This leaves nucleation as the crucial reaction step [15]. In a more general sense, exploiting differences in diffusion rates is a general synthetic philosophy used in all areas of chemistry. For example, organic chemists use bulky “protecting groups” to limit diffusion of reactants to sites, they do not want to react. Expanding on this theme, very slow diffusion rates are often exploited to trap reactive species. In principle, this approach allows studying the kinetics of solid state reactions, i.e. most nano engineered materials are contain “kinetically trapped” non-equilibrium components coexisting

in the subsolidus regime of the respective phase diagrams.

Seminal papers in the 90's reported the preparation of core/shell semiconducting nanoparticles (NPs) based on epitaxial growth, where a wide band gap semiconducting shell provided electronic and physical passivation of the core [16, 17]. The shell material was chosen here for its energy level mismatch and provided little more than electronic and physical passivation, i.e. the particle can be considered monofunctional.

However, when the inorganic cores include two or more chemical species with a combination of metals and metal chalcogenides [18] or metal oxides [19-22], the composition and distribution of each species provide additional parameters that must be controlled. A single particle can display several types of structures depending on the distribution of the components: (i) a chemically disordered alloy, (ii) a layered core/shell, or (iii) an anisotropic phase-segregated structure. In general, NPs with two chemical species obtained by conventional chemical syntheses have an isotropic alloy or a core/shell structure.

Anisotropic phase segregated NPs (e.g. noble metal@metal oxide nanoparticles like Pt@Fe_3O_4 [19], Au@Fe_3O_4 [20], Ag@Fe_3O_4 [21] or Au@MnO [22] nanoparticles have recently become accessible and received much attention. The close coupling of different components on the nanoscale may significantly improve the application performance or even create new properties: (i) multifunctionality, e.g. by a combination of magnetic and plasmonic NPs [19-22], (ii) directed self-assembly, achieved by modifying different functional ligands on each surface [20b,d], (iii) efficient charge separation at the hetero-interface in a single NP [23].

However, the ternary phase diagram Au-Fe-O does not contain any ternary phases. Therefore, the formation of heteroparticles like Au@Fe_3O_4 [20], by phase separation is not surprising.

In this contribution, we report the synthesis of Cu@Fe_3O_4 heterodimer nanoparticles with different morphologies. Copper is known to form very stable binary oxides such as Cu_2O [24] and CuO [25] or stable ternary phases such as copper ferrite ($CuFe_2O_4$) [26], copper substituted Fe_3O_4 [27] or the delafossite-type $CuFeO_2$ [28] however, the formation of heterodimers is unexpected.

The both Cu and Fe_3O_4 domains of Cu@Fe_3O_4 heterodimer nanoparticles can be functionalized with multifunctional polymeric ligands. After surface functionalization, these nanoparticles were transferred to water phase and were stable over several weeks. Moreover, the presence of nanodomains with different composition within the same nanoparticle allows separated features such as (i) nitric oxide (NO) formation, a very important molecule studied

in environmental and biological sciences, promoted by the Cu domain and (ii), easy removal of nanoparticles from reaction medium by making use of its magnetic properties derived from the Fe_3O_4 domain.

2.2. Results and Discussion

The formation of the phase separated $Cu@Fe_3O_4$ heteroparticles indicates that the low temperature solution synthesis presents a simple approach to the kinetically controlled synthesis of solids where nucleation of a crystalline solid is the rate limiting step whereas diffusion plays only a minor role. The key synthetic intermediate is a metal nanoparticle formed by decomposition of an "organometallic" precursor (Scheme. 2.1). In contrast, a direct solid-state reaction between two components would be limited by the interdiffusion of the components. Moreover, high temperatures and long reaction times are usually necessary for reactions between bulk components/elements as a result of the high activation energies of diffusion in the solid state.

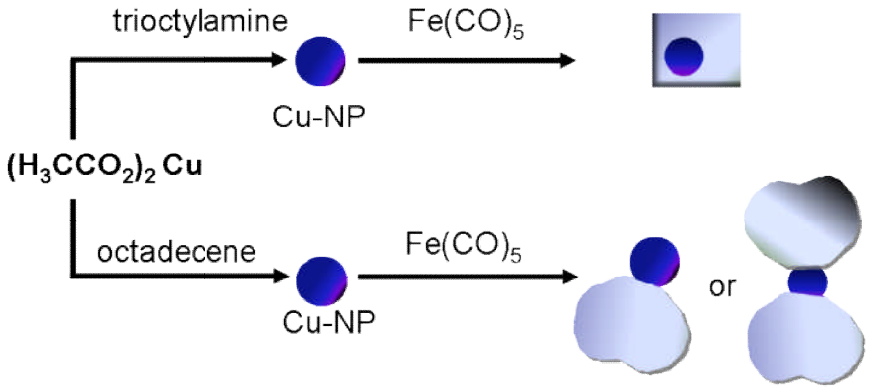

Scheme 2.1. *Schematic representation of the formation of $Cu@Fe_3O_4$ heterodimers with different morphologies in the presence of different solvents during the synthesis. A cube shaped heterodimer morphology is formed in the presence of polar solvent whereas particles with a cloverleaf shaped morphology are formed in apolar solvent.*

Scheme 2.1 demonstrates the synthesis of $Cu@Fe_3O_4$ heterodimer nanoparticles with a cubic and a cloverleaf morphologies by an appropriate choice of precursor compounds, temperature and solvent. Copper nanoparticle intermediates were formed in situ by decomposition reduction of copper acetate precursor in the presence of oleylamine and oleic acid at temperatures around 100 °C. This can be monitored visually from the color change. Fe_3O_4 nanoparticles were grown by subsequent injection of $Fe(CO)_5$ at slightly elevated temperature

(~ 200°C). Cu@Fe_3O_4 heterodimers with cubic morphology were obtained using polar trioctylamine as solvent, whereas Cu@Fe_3O_4 heteroparticles with a cloverleaf morphology were obtained when apolar octadecane was used as a solvent.

Figure 2.1a and b show the transmission electron microscopy (TEM) and high resolution (HR)TEM images of the cube shaped Cu@Fe_3O_4 heterodimer nanoparticles with a spherical Cu component (Ø ≈ 8-10 nm, darker part) attached to Fe_3O_4 cubes (Ø ≈ 18-20 nm, brighter part). Figure 2.1c and d show cloverleaf shaped Cu@Fe_3O_4 nanoparticles obtained in apolar solvents such as octadecane; here the copper cores have diameters of about 10-15 nm, while the iron oxide petals are 18-22 nm in diameter. The initial phase analysis of the iron oxide phase was carried out with electron diffraction. The resulting Debye-Scherrer rings shown in Figure 2.2 (from 1-4: [111], [220], [113] and [002] planes) indicate the presence of face-centered cubic (*fcc*) magnetite (Fe_3O_4). It is worth mentioning that in spite of the different particle morphologies obtained in polar and apolar solvents; the electron diffraction patterns indicates, in both cases, the presence of Fe_3O_4.

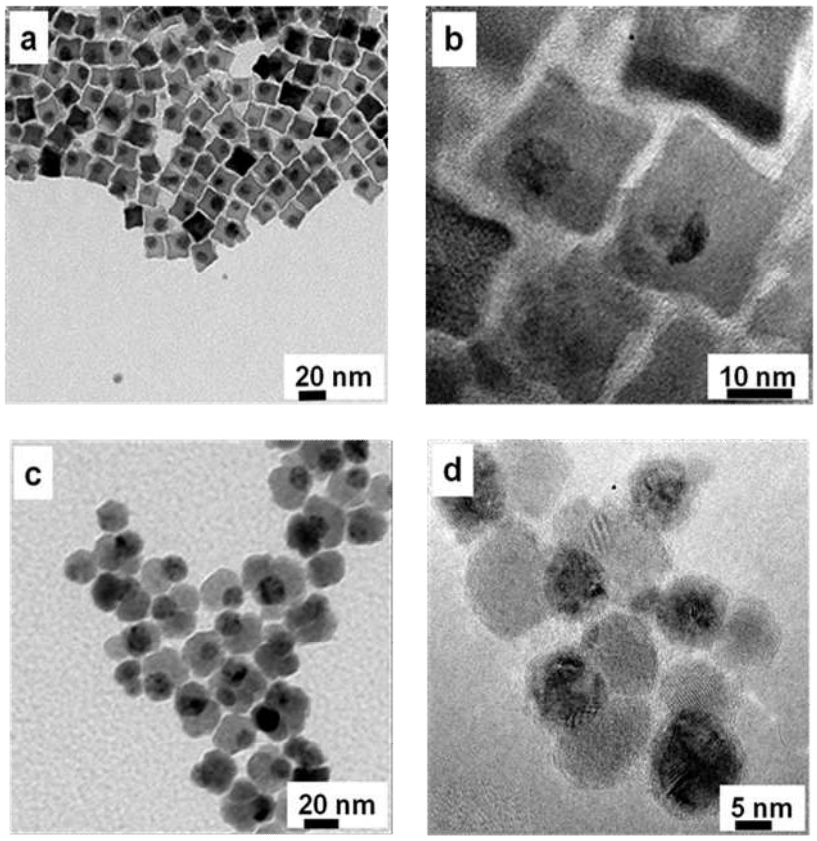

Figure 2.1. *Transmission electron microscopy (TEM) images of (a) cube shaped $Cu@Fe_3O_4$ heteroparticle obtained using trioctylamine as a solvent and (b) correspondent (HR)TEM image. (c) Overview image of cloverleaf shaped $Cu@Fe_3O_4$ heterodimer particles obtained using octadecene and (d) corresponding HRTEM image.*

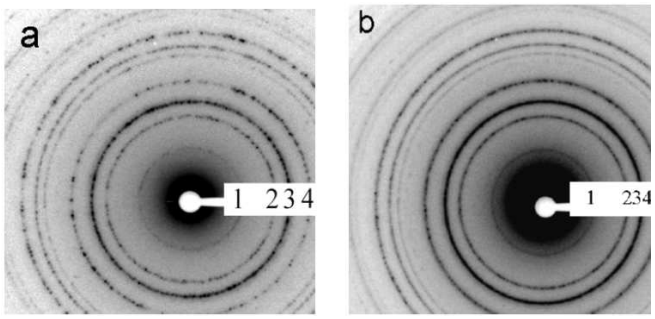

Figure 2.2. *Electron diffraction pattern of the magnetite component in (a) cube shaped and (b) cloverleaf shaped $Cu@Fe_3O_4$ nanoparticles.*

The elemental composition was determined by both, line scan EDX and elemental mapping using scanning transmission electron microscopy (STEM) combined with energy dispersive x-ray spectroscopy (EDS). Due to its higher electron density copper showed brighter spots compared to magnetite which appears darker in the STEM image in Figure 2.3a. It was also confirmed from the EDX-mapping (Figure 2.3a) that yellow spots (copper) correspond to the brighter areas of the STEM image in (Figure 2.3a) and darker areas are composed of Fe and O which appears orange brown and red in the EDS elemental mapping. Figure 2.3b and c represent the EDX line scan profiles of the $Cu@Fe_3O_4$ heterodimers with cubic and cloverleaf morphologies as shown in the respective insets. Again, the relative positions of the peaks in the brighter areas correspond to copper, surrounded by iron oxide.

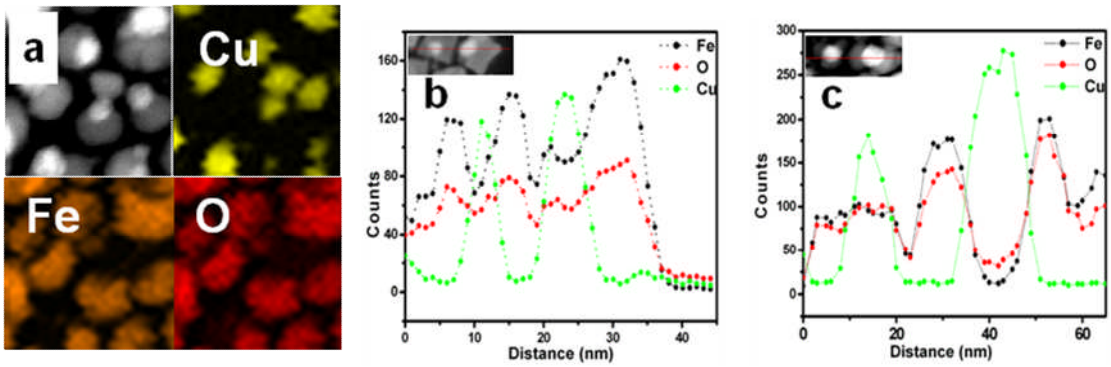

Figure 2.3. *Elemental mapping of coverleaf like $Cu@Fe_3O_4$ heterodimer nanoparticles synthesized in octadecane. (a) STEM mode image and corresponding elemental maps of Cu (yellow), Fe (orange) and O (red) obtained by recording spatial distribution. (b and c) EDS line scan profiles confirm the presence of copper, iron and oxygen.*

Representative XRD patterns of as synthesized $Cu@Fe_3O_4$ heterodimer nanoparticles are presented in Figure 2.4. The positions and relative intensities of the reflections match well with those of standard Fe_3O_4 and Cu powder diffraction data, indicating that the synthesis yielded a nano-heterodimer consisting of magnetite (space group 227, Fd-3m) and Cu (space group 225, Fm-3m). The powder XRD data of both types of $Cu@Fe_3O_4$ heterodimers (cubes and cloverleafs) were essentially identical.

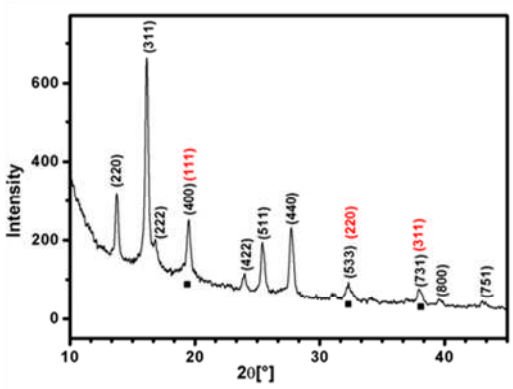

Figure 2.4. *X-ray diffraction patterns of Cu@Fe_3O_4 nanoparticles.*

The magnetic properties of the Cu@Fe_3O_4 heterodimers were investigated to evaluate the effect of the diamagnetic Cu cores on the Fe_3O_4 domains. Figure 2.5a and b show magnetic hysteresis loops of the cube shaped Cu@Fe_3O_4 heterodimer nanoparticles (Ø of the Cu cores ≈ 8-10 nm, Ø of the Fe_3O_4 domains ≈ 18-20 nm, recorded at 5 K and 300 K) and the cloverleaf shaped Cu@Fe_3O_4 heteroparticles (Ø of the Cu cores ≈ 10-15 nm, Ø of the Fe_3O_4 domains ≈ 18-22 nm, recorded at 5 K and 300 K). The interface communication between the nanoscale Cu and Fe_3O_4 components also leads to the change of magnetization behavior of the Fe_3O_4 nanoparticles. The Cu@Fe_3O_4 heteroparticles have shown superparamagnetic behavior at room temperature with no coercivity for both morphology (Figure 2.5).

The saturation magnetizations of the cube shaped Cu@Fe_3O_4 heterodimer nanoparticles and cloverleaf shaped Cu@Fe_3O_4 at room temperature are 32 emu/g and 15 emu/g (Figure 2.5), which are significantly smaller than the bulk magnetization of Fe_3O_4 (82 emu/g) [29] and, for the Cu@Fe_3O_4 cloverleafs, are comparable to those of nanosized copper ferrite (≈ 45 emu/g) [30] although the presence of copper ferrite can be excluded safely based on the mössbauer data (Figure 2.6 & Appendix 1). Several effects might be responsible for the reduced moment of the magnetite component: (i) coupling between the magnetite domains via the Cu block or surface spin canting of the particle blocks, or (ii) the crystallinity of the magnetite blocks. Comparable values have been reported for iron oxide nanoparticles prepared by ultrasonic decomposition of iron carbonyl [31] and laser pyrolysis [32], which lead to lower crystallinity particles due to the mechanism of formation, by aggregation. The difference in the magnetic moments at 300 K and 5 K can be explained based on the temperature dependence of the magnetization. In the bottom right insets of Figure 2.5a and b we show the temperature dependence of the magnetization for the field cooled (FC) and zero field cooled (ZFC) curves

of $Cu@Fe_3O_4$ heterodimers under applied magnetic fields of 100 Oe. The blocking temperature well above room temperature can be attributed to the size of the nanoparticles.

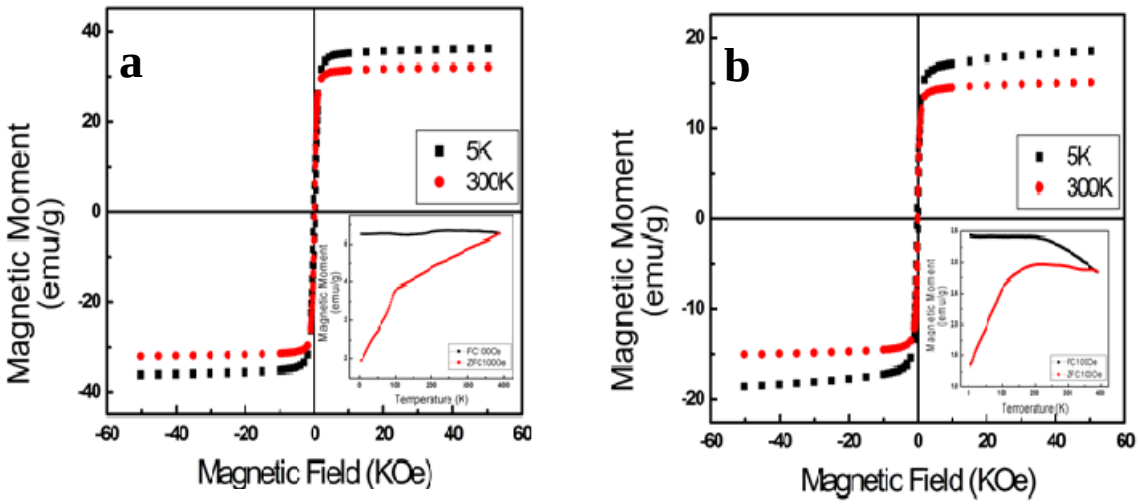

Figure 2.5. *Magnetic hysteresis loops at 5 K and 300 K and (a) cube shaped $Cu@Fe_3O_4$ heterodimer nanoparticles and (b) $Cu@Fe_3O_4$ cloverleaf shaped heterodimer nanoparticles. Temperature dependence of the magnetization in field cooling (FC) and zero field cooling (ZFC) modes are given in insets.*

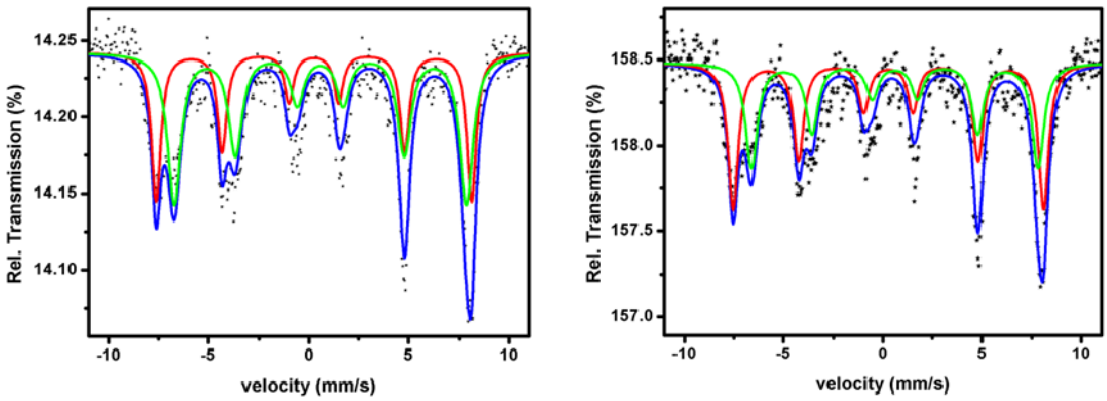

Figure 2.6. *^{57}Fe Mössbauer spectra of the $Cu@Fe_3O_4$ heterodimer nanoparticles at 300 K. Left panel is from cube shaped and right one is cloverleaf shaped $Cu@Fe_3O_4$ heterodimer nanoparticles.*

The light scattering efficiency of single particle was explored in an optical microscope with white light illumination in total internal reflection mode using a Koheras Super K Power

white light source (at 50% power, beam diameter approx. 1 mm). The particles were immobilized on the bottom of a flat glass capillary filled with hexane. The particles appeared as reddish spots to the eye (Figure 2.7) with a few white to green spots under the microscope. The red spots probably correspond to the $Cu@Fe_3O_4$ particles. The single particle spectra of the $Cu@Fe_3O_4$ nanoparticles show a resonance peak as expected for plasmonic nanoparticles (Appendix 2).

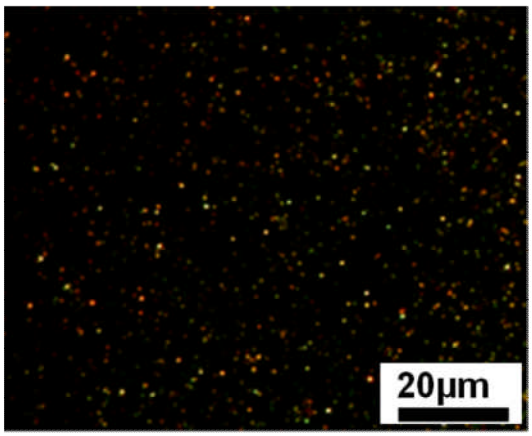

Figure 2.7. *Real color picture of immobilized $Cu@Fe_3O_4$ nanoparticles under dark field illumination.*

Both $Cu@Fe_3O_4$ (cube shaped and cloverleaf shaped) heterodimer nanoparticles were functionalized using multifunctional polymeric ligands, carrying catechol anchor groups and PEG-linkers ($M_r \approx 800$) with free amino groups for further surface conjugation and improve the solubility in polar solvents. The structure of the polymer is shown in Figure 2.8a. The polymer functionalized $Cu@Fe_3O_4$ nanoparticles were stable against aggregation and precipitation in deionized water for several days as shown in Figure 2.8b.

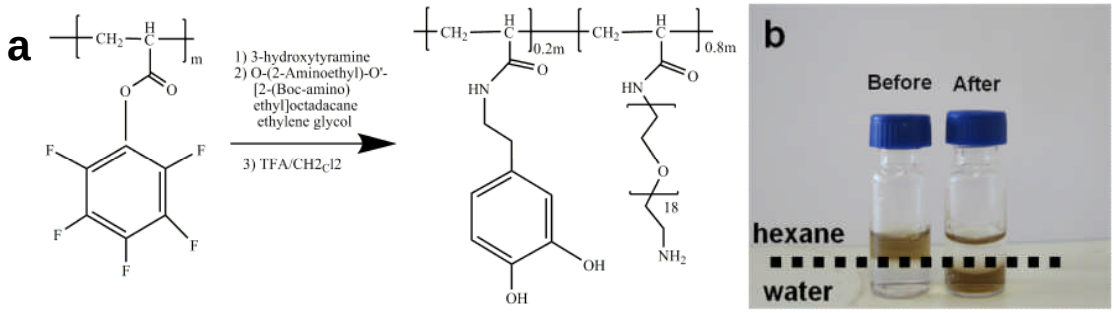

Figure 2.8. *(a) Schematic representation of multifunctional copolymer containing 3-hydroxy-tyramine (dopamine) as an anchor group for the binding of Fe_3O_4 domain. Polymer functionalization. (b) Digital photograph of Cu@Fe_3O_4 solutions before (left) and after (right) surface functionalization in hexane (top layer) and in water (bottom layer).*

One of the potential applications of Cu@Fe_3O_4 nanoparticles was exploited due to the presence of different domains within the same nanoparticle. For this purpose, the Cu domain was assessed by its ability to generate nitric oxide (NO) [33] where the Fe_3O_4 domains would provide the possibility of magnetic separation of nanoparticles from the reaction mixture. Within this view, the focus was made on activity of Cu domain. On the first set of experiments, 20 μg of nanoparticles (final concentration) were tested in the presence of low concentrations of nitric acid (HNO_3) ranging from 5-250 μM (final concentration) and left for 15 min at room temperature. Afterwards, NO formation was detected by co-incubating a dye (2,3-Diaminonaphthalene, DAN) that specifically detects NO by forming a triazole product of NO N- nitrosation yielding strong fluorescence. DAN (0.31 mM prepared in DMSO) was left to react with different vials containing different concentrations of HNO_3 for 5 min at room temperature and under dark conditions. Finally, the solutions were brought to slight alkaline pH values through addition of NaOH, as the fluorescence is only possible to be observed under these conditions [34]. For measuring the fluorescence, the samples were excited at 365 nm and the emission measured at 450 nm. From Figure 2.9a, it can be observed a direct relation between the fluorescence and concentration of HNO_3 present in the reaction vessel, i.e., the fluorescence increases with the increase of HNO_3. The background as well as the control experiments (without nanoparticles) was measured and no fluorescence was observed. In another set of experiments, the concentration of Cu@Fe_3O_4 nanoparticles was varied ranging from 1-100 μg (final concentration) keeping the concentration of HNO_3 constant (10 μM). After incubation for 15 min at room temperature and further addition and co-incubation

of DAN (5 min, room temperature and under dark conditions) the fluorescence was measured as described above for the other experiments. Figure 2.9b shows the same trend as found before for HNO_3 variation, i.e., the higher is concentration of nanoparticles, higher is the fluorescence observed. The inset from Figure 2.9b shows a digital image of the final product (10 μM of HNO_3 and 100 μg of nanoparticles) under 365 nm excitation lamp confirming that the reaction occurs indeed. In addition, in this case, the background and the control experiments were measured and no fluorescence was observed. These results indicate that these heterodimers can be used to generate NO in a HNO_3 and nanoparticle solution in a controlled manner.

For reutilization purposes, the Cu@Fe_3O_4 heterodimer nanoparticles (50μg) were incubated with HNO_3 (50 μM) for 15 min at room temperature. Making use of the Fe_3O_4 domain, a magnet was placed with the side wall of the reaction vial, the nanoparticles get attracted towards magnet (Figure 2.9c). The supernatant was removed and recovered nanoparticles were incubated once more with HNO_3 (50 μM) for 15 min at room temperature. The nanoparticles were again recovered using magnet and the supernatant was tested for the formation of NO. The experiment was repeated for 6 consecutive cycles. Figure 2.9d shows a periodic decrease in the fluorescence intensity which shows the decrease in the concentration of copper being used for the formation of NO.

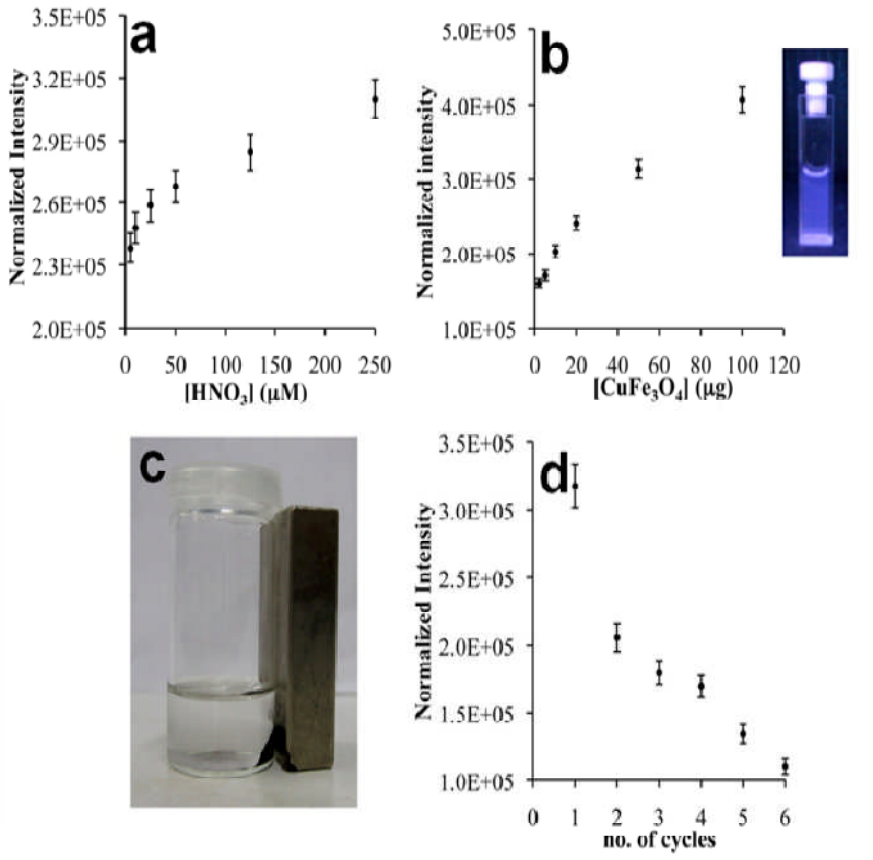

Figure 2.9. *Cu domain was used for the formation of nitric oxide (NO). NO generation was screened by N-nitrosation of 2,3-Diaminonaphthalene(trizole formation) yielding a strong fluorescence under slightly alkaline conditions. The fluorescence was measured at 365 nm (excitation) and 450 nm (emission) (a) Nanoparticles (20 μg) incubated with different concentrations of nitric acid (HNO_3) ranging from 5-250 μM (final concentration). A clear increase on NO is observed in the presence of higher concentrations of HNO_3. (b) Keeping HNO_3 concentration constant (10 μM final concentration) and varying the Cu@Fe_3O_4 heterodimers concentration. (1-100 μg). Again, a clear increment is observed in a nanoparticle dependent manner. Inset: digital image of a solution containing 10 μM of HNO_3 and 100 μg of Cu@Fe_3O_4 (slightly alkaline pH) under a UV lamp (excitation 365 nm). A bluish fluorescence is observed. (c) Magnetic properties of Cu@Fe_3O_4 nanoparticles for recovering after the reaction by making use of Fe_3O_4 domain. (d) Cycles of reutilization of nanoparticles for the formation of nitric oxide (NO). A significant decrease can be observed during consecutive cycles.*

Moreover, the T_1 and T_2-weighted MR image of 3 different concentrations of polymer functionalized cloverleaf and cube shaped Cu@Fe_3O_4 heterodimer nanoparticles, respectively are shown in Figure 2.10. The functionalized nanoparticles were dissolved in saline solution ranging from 0.011 to 0.045 mM for cloverleaf and 0.015 to 0.063 mM for cube shaped Cu@Fe_3O_4 nanoparticles. T_1 and T_2 measurements revealed T_1 and T_2 relaxivities of 28.53 and 333.89 $mM^{-1}s^{-1}$ for the cloverleaf and 19.22 and 74.04 $mM^{-1}s^{-1}$ for cube shaped Cu@Fe_3O_4 heterodimer nanoparticles, respectively.

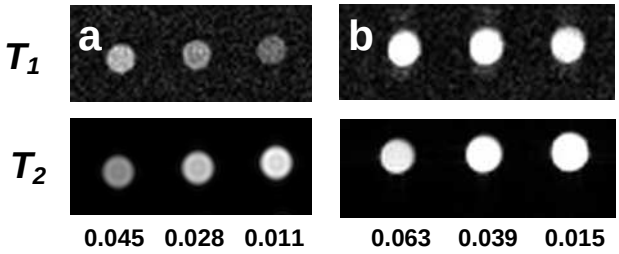

Figure 2.10. *T_1 and T_2-weighted MRI images of solutions containing polymer functionalized Cu@Fe_3O_4 nanoparticles (concentrations in mM) with cloverleaf and cube shaped morphologies, respectively.*

2.3. Summary and Outlook

In summary, we have presented a facile method to synthesize Cu@Fe_3O_4 heterodimer nanoparticles with distinct morphologies. The formation of these nanoparticles is very unexpected, because (i) Cu is not a noble metal and (ii) stable binary copper oxides and several ternary Cu-Fe-O compounds such as $CuFe_2O_4$ [26] or $CuFeO_2$ [27] are known. Thus, different from the formation of heteroparticles such as Au@Fe_3O_4 [20] or Au@MnO [22], where phase separation is the expected process, the formation of Cu@Fe_3O_4 can be considered the intermediate product of a kinetically controlled solid-state reaction, where nucleation of the ternary phase has not yet taken place. In fact, Cu@Fe_3O_4 may be viewed a "snapshot" of the scaling reaction of copper and iron. The Cu@Fe_3O_4 heteroparticles are magnetically and optically active and therefore useful for simultaneous magnetic and optical detection. The special advantage in the application of these heterodimer nanoparticles lies in the fact that nanodomains of different composition can be addressed separately and specifically. This synthetic method can be extended to the synthesis of new nanostructures that have not been reported yet.

2.4. Experimental Section

Methods and Material

Iron(0) pentacarbonyl ($Fe(CO)_5$, 99.5%, Acros), copper acetate monohydrate ($Cu(ac)_2.H_2O$, 99%, Fluka), oleic acid (90%, Aldrich), oleylamine (90%, Acros), 1-octadecene (ODE, 90% Acros), tri n-octylamine (98%, Acros), di-tert-butyl dicarbonate ($(Boc)_2O$, >99%, Aldrich), dioxane (p.A. Fisher), $H_2N\text{-}PEG_{(800)}\text{-}NH_2$ (Aldrich), triethylamine (>99%, Aldrich), 3-hydroxy tyramine hydrochloride (Dopamine.HCl) (98%, Aldrich), trifluoroacetic acid (TFA) (99%, Aldrich), ethanol (99.8%, Roth), toluene (>99%, Aldrich), hexane (p.A. Fisher), dichloromethane DCM (p.A. Fisher), dimethylformamide (DMF) (extra dry, >99.8%, Acros), diethyl ether (p.A. Fisher) were used as received without further purification.

Synthesis of Cube Shaped $Cu@Fe_3O_4$ Heterodimer Nanoparticles

Under a constant flow of argon (Ar), 1 mmol copper acetate, $Cu(ac)_2$, 3 mmol oleic acid, 3 mmol oleylamine and 10 ml trioctylamine were mixed. The solution was heated to 120ºC with a constant rate of 3ºC/min. After reaching to this temperature, $Fe(CO)_5$ was added and the temperature was raised to 200ºC and kept at this temperature for 30 minutes. The product was precipitated by addition of excess of ethanol and collected by centrifugation (9000 rpm, 10 min, RT). The nanoparticles were repeatedly washed by dissolving them in hexane, precipitating them with ethanol and centrifugation (9000 rpm, 10 min, RT). Finally, the product was dissolved in toluene, flushed with argon (Ar) and stored at +4ºC.

Synthesis of Cloverleaf Shaped $Cu@Fe_3O_4$ Heterodimer Nanoparticles

The synthesis of cloverleaf shaped heteroparticles of $Cu@Fe_3O_4$ was achieved by the same procedure. 1-octadecene was used as a solvent instead of trioctylamine.

Synthesis of Boc Protected Bis-Amine $PEG_{(800)}$ ($NBoc\text{-}PEG_{(800)}\text{-}NH_2$)

A solution of $(Boc)_2O$ (0.02 mol) in 30 mL of anhydrous dioxane was added drop wise to a solution of $NH_2\text{-}PEG_{(800)}\text{-}NH_2$ (0.1 mol) in 50 mL anhydrous dioxane. The resulting solution was stirred overnight at room temperature. The solvent was evaporated and the oily product obtained was dissolved in 50 mL of water and extracted thrice using 50 mL of CH_2Cl_2. The combined organic phases were washed with a conc. solution of NaCl and dried over anhydrous Na_2SO_4. The resulting organic phase was concentrated by rotary evaporation and viscous, colorless oil was obtained. Further purification was achieved by flash chromatography on silica using a CH_2Cl_2/ethanol mixture (2:1) as eluent.

Preparation of the Polymer

The poly (active ester) poly(pentafluorophenyl acrylate) (PFA) was prepared as reported earlier [34]. GPC analysis of the obtained polymer (THF, light scattering detection) gave the following values: M_n = 16,390 g/mol, with PDI = 1.39, with an average of 70 repeating units.

For the synthesis of the multifunctional poly(acrylamides), poly(active ester) poly(pentafluorophenyl acrylate) (700 mg, 2.94 mmol repeating units) was dissolved in a mixture of 9 mL of dry DMF and 0.7 ml of triethylamine. After that, 3-hydroxytyramine hydrochloride (24 mg) dissolved in 3 mL DMF and 0.4 ml triethylamine was added and the reaction mixture was stirred for 3 hours at 50°C. In the final step the remaining active ester groups were substituted using an excess of NBoc-$PEG_{(800)}$-NH_2 (dissolved in 3 mL dry DMF) and stirring for 5 h at 50°C. The solution was concentrated to about 2 mL and the polymeric ligand was precipitated by addition of cold ethyl ether. The precipitated polymer was centrifuged (9000 rpm, 10 min and RT) and the solvent was decanted. Upon drying, 286 mg of colorless oil was obtained.

Cleavage of the Boc Group

The polymer obtained above was dissolved in CH_2Cl_2 (30 mL). After that, trifluoroacetic acid (2.0 mL) was added and the mixture was stirred at room temperature for 2 h. After that, the reaction solution was treated with mixture of water and hexane (30 mL/50 mL) and vigorously stirred for 30 minutes. The aqueous phase containing the polymer was separated and concentrated to 2 mL and dialysed against deionized water for 2 days at room temperature (cellulose membrane, MWCO = 3,500). Finally, the water was evaporated and the product was redissolved in $CHCl_3$ and to make a stock solution, which was kept at +4ºC.

Functionalization of the Fe_3O_4 Domains in the Cu@Fe_3O_4 Heterodimer Nanoparticles

Cu@Fe_3O_4 heterodimer nanoparticles (10 mg) were dispersed in 15 ml of $CHCl_3$ by slowly dropping over 1 h into the above synthesized polymeric ligand solution (20 mg/10 mL, chloroform). The reaction was continuously stirred overnight at room temperature, under inert conditions. The functionalized nanoparticles were precipitated by addition of hexane and separated from unbound polymer and surfactants by centrifugation. The Cu@Fe_3O_4 nanoparticles were washed twice by dissolving them in chloroform and precipitating them with hexane. Finally, the particles were stored in or DMF at +4ºC.

Nitric Oxide (NO) Formation Using Cu@Fe_3O_4 Heterodimers

Polymeric ligand functionalized Cu@Fe_3O_4 heterodimer nanoparticles were assayed for nitric oxide formation by a modifying a standard methodology [35]. Nanoparticles (20 μg final

concentration) were incubated with different concentrations of nitric acid (HNO_3) ranging from 5 to 250μM (final concentration) for 15 min at room temperature. In another experiment, the concentration of nanoparticles were changed (1-100 μg) while keeping HNO_3 concentration (10 μM) constant and the reaction was left for 15 min at room temperature. As controls, the incubation was performed in the absence of nanoparticles in parallel. In both cases, the experiments were performed in triplicate and treated as follows. A solution of 2,3-Diaminonaphthalene (0.31 mM prepared in DMSO) (DAN) (Cat. No. 88461, Bioreagent, ≥98.0% HLPC, Sigma) was added (20 μL) to the reaction mixture and left to react for 5 min at room temperature under dark conditions. Then NaOH (2 μL, 2.0 M) was added and 100 μL of this solution diluted with 2 mL of distilled water. The fluorescence was measured using excitation wavelength of 365 nm and emission at 450 nm. Fluorescence spectra (emission) were acquired in a semi-micro cuvette with a Bruins Instruments Omega 20 spectrophotometer and a Jobin-Ivon Spex Fluoromax-2 spectrofluorometer. Fluorescence spectra were corrected for wavelength dependence of the fluorimeter as well as for the inner filter effect both for excitation and emission [36].

Recovery and Reutilization of Heterodimers

The polymer functionalized heterodimers were recovered to access their ability to promote formation of nitric oxide in several subsequent cycles. Cu@Fe_3O_4 heterodimers (50μg) HNO_3 (50μM) was added and left for 15 min at room temperature. The Cu@Fe_3O_4 heterodimer nanoparticles were recovered using magnetic separation with the help of a magnet and tested for the formation of NO. Six cycles were carried out. The experiments were performed in triplicate.

Physical Characterization

Electron Microscopy

The size and morphology of the naked and surface functionalized Cu@Fe_3O_4 nanoparticles were investigated using transmission electron microscopy (TEM, Philips EM 420 instrument with an acceleration voltage of 120 kV). Samples for transmission electron microscopy were prepared by placing a drop of dilute nanoparticle solution in hexane on a carbon coated nickel grid. Low-resolution TEM images were recorded on a Philips EM420 microscope operating at an acceleration voltage of 120 kV. High-resolution TEM data and ED patterns were obtained on a FEI Tecnai F30 S-TWIN with a 300 kV field emission gun.

X-Ray Diffraction

XRD measurements were performed on a Bruker D8 Advance diffractometer equipped with a

Sol-X energy-dispersive detector and operating with Mo Kα radiation.

Mössbauer Spectroscopy and Superconducting Quantum Interference Device

Mössbauer spectra were obtained at room temperature 110 K and 80 K with a constant acceleration transmission mössbauer spectrometer and ^{57}Co (Rh) source. A α-Fe foil was used to calibrate the mössbauer spectrometer in a velocity range of ±12 mms^{-1}. Magnetic measurements were carried out using a Quantum Design MPMS-XL SQUID magnetometer.

Light Scattering

The light scattering efficiency of single particles was explored in an optical microscope with white light illumination in total internal reflection mode using a Koheras Super K Power white light source (at 50% power, beam diameter approx. 1 mm).

Magnetic Resonance Imaging

To investigate the magnetic resonance imaging, different concentrations of polymer functionalized Cu@Fe_3O_4 nanoparticles dissolved in saline solution were performed on a clinical 3.0 Tesla scanner (Magnetom Trio, Siemens Medical Solutions, Erlangen, Germany) by means of a T_1 and T_2 measurement using a centric reordered saturation recovery (SR) prepared snapshot fast low angle shot (SR-TurboFLASH) pulse sequence with different preparation times (TI) ranging from 20 ms up to 8000 ms. Other pulse sequence parameters were as follows: repetition time (TR) = 3.4 ms, echo time (TE) = 1.5 ms, flip angle = 20°.

2.5. References

[1] G. A. Ozin, *Adv. Mater*. **1992**, *4*, 612.

[2] H. Gleiter and P. Marquardt, *Z. Metallkd.* **1984**, *75*, 263.

[3] M. Bawendi, M. L. Steigerwald and L. E. Brus, *Annu. Rev. Phys. Chem.* **1990**, *41*, 477.

[4] L. E. Brus, *J. Phys. Chem.* **1986**, *90*, 2555.

[5] T. Kato, *Science* **2002**, *295*, 2414.

[6] D. V. Talapin, J.-S. Lee, M. V. Kovalenko and E. V. Shevchenko. *Chem*. *Rev*. **2010**, *110*, 389.

[7] M. Noh and D. C. Johnson, *Angew*. *Chem.* **1996**, *108*, 2805; *Angew*. *Chem. Int. Ed.* **1996**, *35*, 2666.

[8] C. M. Falco and B. N. Engel, *Physica B* **1991**, *169*, 293.

[9] J. Das, M. B. Tang, K. B. Kim, R. Theissmann, F. Baier, W. H. Wang and J. Eckert, *Phys. Rev. Lett*. **2005**, *94*, 205501/1.

[10] D. Shechtman, I. Blech, D. Gratias and J. W. Cahn, *Phys. Rev. Lett.* **1984**, *53*, 1951.

[11] M. D. Hornbostel, E. J. Hyer, J. P. Thiel and D. C. Johnson, *J. Amer. Chem. Soc*. **1997**, *119*, 2665.

[12] I. S. Beloborodov, A. V. Lopatin, V. M. Vinokur and K. B. Efetov, *Rev. Mod. Phys*. **2007**, *79*, 469.

[13] J. Park, J. Joo, S. G. Kwon, Y. Jang and T. Hyeon, *Angew. Chem.* **2007**, *119*, 4714; *Angew*. *Chem. Int. Ed*. **2007**, *46*, 4630.

[14] C. S. Birkel, E. Mugnaioli, M. Panthöfer, U. Kolb and W. Tremel, *J. Am. Chem. Soc.* **2010**, *132*, 9881.

[15] N. Zink, H. A. Therese, J. Pansiot, A. Yella, F. Banhart and W. Tremel, *Chem*. *Mater*. **2008**, *20*, 65.

[16] B. O. Dabbousi, J. Rodriguez-Viejo, F. V. Mikulec, J. R. Heine, H. Mattoussi, R. Ober, K. F. Jensen and M. G. Bawendi, *J. Phys. Chem. B* **1997**, *101*, 9463.

[17] M. A. Hines and P. Guyot-Sionnest, *J. Phys. Chem*. **1996**, *100*, 468.

[18] (a) T. Mokari, E. Rothenberg, I. Popov, R. Costi and U. Banin, *Science* **2004**, *304*, 1787. (b) H. Gu, R. Zheng, X. Zhang and B. Xu, *J. Am. Chem. Soc.* **2004**, *126*, 5664. (c) T. Mokari, C. G. Sztrum, A. Salant, E. Rabani and U. Banin, *Nat*. *Mater*. **2005**, *4*, 855. (d) T. Teranishi, M. Saruyama, M. Nakaya and M. Kanehara, *Angew*. *Chem*. **2007**, *119*, 1743; *Angew*. *Chem. Int. Ed*. **2007**, *46*, 1713.

[19] C. Wang, H. Daimon and S. Sun, *Nano Lett*. **2009**, *9*, 1493.

[20] (a) H. Yu, M. Chen, P. M. Rice, S. X. Wang, R. L. White and S. Sun, *Nano Lett.* **2005**, *5*, 379. (b) Y. Wei, R. Klajn, A. O. Pinchuk and B. A. Grzybowski, *Small* **2008**, *4*, 1635. (c) C. Xu, J. Xie, D. Ho, C. Wang, N. Kohler, E. G. Walsh, J. R. Morgan, Y. E. Chin and S. Sun, *Angew. Chem.* **2008**, *120*, 179. *Angew. Chem. Int. Ed*. **2008**, *47*, 173. (d) Y. Wei, K. J. M. Bishop, J. Kim, S. Soh and B. A. Grzybowski, *Angew. Chem*. **2009**, *121*, 9477. *Angew. Chem. Int. Ed*. **2009**, *48*, 9477.

[21] G. Lopes, J. M. Vargas, S. K. Sharma, F. Beron, K. R. Pirota, M. Knobel, C. Rettori and R. D. Zysler, *J. Phys. Chem. C* **2010**, *114*, 10148.

[22] T. D. Schladt, M. I. Shukoor, M. N. Tahir, F. Natalio, K. Schneider, I. Ament, J. Becker, F. Jochum, S. Weber, P. Theato, L. M. Schreiber, C. Sönnichsen, H. C. Schröder, W. E. G. Müller and W. Tremel, *Angew. Chem.* **2010**, *122*, 4068; *Angew. Chem. Int. Ed.* **2010**, *49*, 3976.

[23] L. Carbone, A. Jakab, Y. Khalavka and C. Sönnichsen, *Nano Lett.* **2009**, *9*, 3710.

[24] R. D. Schmidt-Whitley, M. Martinez-Clemente and A. Revcolevschi, *J. Cryst. Growth* **1974**, *23*, 113.

[25] (a) A. E. Rakhshani, *Solid State Electron* **1986**, *29*, 7. (b) J. B. Forsyth, P. J. Brown and B. M. Wanklyn, *J. Phys. C* **1988**, *21*, 2917. (c) B. X. Yang, T. R. Thurston, J. M. Tranquada and G. Shirane, *Phys. Rev. B* **1989**, *39*, 4343.

[26] (a) J. L. Snoek, *Rev. Tech. Philips* **1946**, *8*, 359. (b) E. F. Bertaut *J. Phys. Radium* **1951**, *12*, 252. (c) K. Stierstadt, *Z. Phys*. **1956**, *146*, 169. (d) J. B. Goodenough and A. L. Loeb, *Phys. Rev*. **1953**, *98*, 391. (e) X. X. Tang, A. Manthiram and J. B. Goodenough, *J. Solid State Chem.* **1989**, *79*, 250.

[27] E. Mugnier, I. Pasquet, A. Barnabé, L. Presmanes, C. Bonningue and P. Tailhades, *Thin Solid Films* **2005**, *493*, 49.

[28] (a) R. D. Shannon, D. B. Rogers and C. T. Prewitt, *Inorg. Chem.* **1971**, *10*, 713. (b) C. T. Prewitt, R. D. Shannon and D. B. Rogers, *Inorg. Chem.* **1971**, *10*, 719. (c) D. B. Rogers, R. D. Shannon, C. T. Prewitt and J. L. Gillson, *Inorg. Chem.* **1971**, *10*, 723. (d) K. O'Grady and A. Bradbury, *J. Magn. Magn. Mater*. **1983**, *39*, 91. (e) R. Seshadri, C. Felser, K. Thieme and W. Tremel, *Chem. Mater*. **1998**, *10*, 2189.

[29] K. O' Grady and A. Bradbury, *J. Magn. Magn. Mater*. **1983**, *39*, 91.

[30] S. J. Stewart, M. J. Tueros, G. Cernicchiaro and R. B. Scorzelli, *Solid State Commun*. **2004**, *129*, 347.

[31] K. V. P. M. Shafi, S. Wizel, T. Prozorov and A. Gedanken, *Thin Solid Films* **1998**, *318*, 38.

[32] M. P. Morales, O. Bomati-Miguel, R. Perez de Alejo, J. Ruiz-Cabello, S. Veintemillas-Verdaguer and K. O'Grady, *J. Magn. Magn. Mater.* **2003**, *266*, 102.

[33] F. A. Cotton and G. Wilkinson, *Advanced Inorganic Chemistry*; John Wiley & Sons: New York, **1988**.

[34] (a) P. Theato, *J. Polym. Sci. Part A: Polym. Chem.* **2008**, *46*, 6677. (b) M. I. Shukoor, F. Natalio, M. N. Tahir, M. Wiens, M. Tarantola, H. A. Therese, M. Barz, S. Weber, M. Terekhov, H. C. Schröder, W. E. G. Müller, A. Janshoff, P. Theato, R. Zentel, L. M. Schreiber and W. Tremel, *Adv. Funct. Mater*. **2009**, *19*, 285.

[35] A. M. Miles, Y. Chen, M. W. Owens and M. B. Grisham, *Methods: a companion to methods in enzymology*; Academic Press: New York, **1995**.

[36] J. R. Lakowicz, *Principles of Fluorescence Spectroscopy*; Kluwer Academic/Plenum Publisher: New York, **1999**.

3. Synthesis, Characterization and Functionalization of nearly Monodisperse Copper Ferrite $Cu_xFe_{3-x}O_4$ Nanoparticles

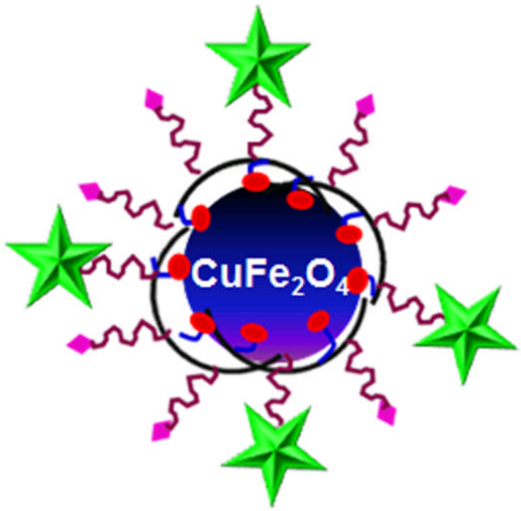

Bahar Nakhjavan[a], Muhammad Nawaz Tahir[a], M. Panthöfer[a], Haitao Gao[a], Thomas D. Schladt[a], Teuta Gasi[a], Vadim Ksenofontov[a], Robert Branscheid[b], Stefan Weber[c], Ute Kolb[b], Laura Maria Schreiber[c], Wolfgang Tremel[*a]

[a]Institut für Anorganische Chemie und Analytische Chemie, Johannes Gutenberg-Universität, Duesbergweg 10-14, D-55099 Mainz, Germany. Fax: +49 6131 39-25605; Tel: +49 6131 39-25135; E-mail: tremel@uni-mainz.de

[b]Institut für Physikalische Chemie, Johannes Gutenberg-Universität, Welderweg 11, 55099 Mainz, Germany.

[c]Bereich Medizinische Physik, Klinik und Poliklinik für diagnostische und interventionelle Radiologie, Klinikum der Johannes Gutenberg-Universität Mainz. Langenbeckstraße, 1, 55131, Mainz, Germany.

J. Mater. Chem. **2011**, *21*, 6909-6915

3.1. Introduction

Magnetic nanoparticles (MNPs) are playing increasingly important roles in biotechnology and biomedicine [1]. MNPs have been used as carriers for magnetic drug targeting [2], as tags for biomolecular sensors [3, 4], in biomolecule separation and purification [5-7], as well as for *in vivo* imaging [8-10] and hyper-thermia treatment [11, 12]. As these and other applications become more advanced, precise control over particle composition, stability and surface functionality is crucial. Among the magnetic materials, the ferrites with general formula MFe_2O_4 have been used in many applications. By adjusting the M^{2+} cation, the magnetic configurations of the spinel-type MFe_2O_4 can be engineered to provide a wide range of magnetic properties [13]. Several studies on pure nanoferrites such as Fe_3O_4 [14], $NiFe_2O_4$ [15], $CoFe_2O_4$ [16], $ZnFe_2O_4$ [17] and $MnFe_2O_4$ [18, 19] have demonstrated the interplay of composition [20], cation distribution [21, 22] and size [23] in view of their properties and applications.

Among the ferrites, $CuFe_2O_4$ has received significant attention in recent years [24, 25]. $CuFe_2O_4$ coatings based on highly aggregated nanoparticles were prepared using electrochemical methods [26]. Plate-like $CuFe_2O_4$ particles were obtained using reverse micelle and hydrothermal methods [27]. Nanocrystalline $CuFe_2O_4$ was prepared by co-precipitation [28], mechanical milling [29], sol-gel methods [30], or precipitation in a polymer matrix [31]. Goya et al. [32] who synthesized $CuFe_2O_4$ by high-energy ball milling showed that the milling process reduces the average grain size of $CuFe_2O_4$ but induces severe cation redistribution between tetrahedral and octahedral sites.

Ferrites are among the most important and interesting oxides owing to their wide variety of applications in sensors, electronics and catalysts [33, 34]. e.g. as abatement of gaseous pollutants [35] and the water gas shift reaction [36]. Recently, copper ferrites have been proposed as a reforming catalyst for hydrogen production from oxygenated hydrocarbons [37-40]. In spite of the availability of different synthetic methods and promising potential applications, the synthesis of highly monodisperse and non-aggregated $CuFe_2O_4$ nanoparticles has not been mastered so far. Previous reports based on high temperature or hydrothermal procedures described the synthesis of agglomerated and mostly polydisperse material, where the question of site preference could only partially be addressed and resolved [24-32]. Here we demonstrate a facile and simple method for the synthesis of uniform and non-aggregated ($x \approx 0.32$) nanoparticles by using two suitable precursors in a hot organic solvent. The Cu_xFe_{3-}

$_xO_4$ copper ferrite particles can be functionalized with a multifunctional polymeric ligand to yield highly water soluble and fluorescent magnetic nanoparticles that may be used for bioimaging.

3.2. Results and Discussion

The transmission electronic microscopy (TEM) measurements performed for the nanoparticles show the presence of spherical non-aggregated uniform nanoparticles homogeneously dispersed in hexane. A TEM image of the nanoparticles is shown in Figure 3.1 as a representative example. The size distribution as obtained from TEM measurements shows that the mean size value of the nanoparticles is centered at 7.2 nm (Figure 3.1c). The crystallinity and phase identity of the nanoparticles was demonstrated by the electron diffraction pattern as shown an inset in Figure 3.1b. The electron diffraction pattern can be indexed to the cuprospinel structure ($CuFe_2O_4$) with the lattice parameters a = 8.4, α = 90°and space group (SG) $Fd\bar{3}m$ (No. 227). Moreover, *d*-values reported by the Debye-Scherrer rings (2.9326, 2.5253, 1.7109, 1.6103, 1.4826, 1.2763, 1.2055, 1.0905) confirm this structure (inset Figure 3.1b). The sample contains approx. 1%wt. Cu and 9.8%wt. Cu_2O. The final structure model of "$CuFe_2O_4$" points towards only a partial substitution of Fe by Cu on the *8c* site exclusively (occ_{16c} (Cu) = 0.0(1) and occ_{8c} (Cu) = 0.32(9)).

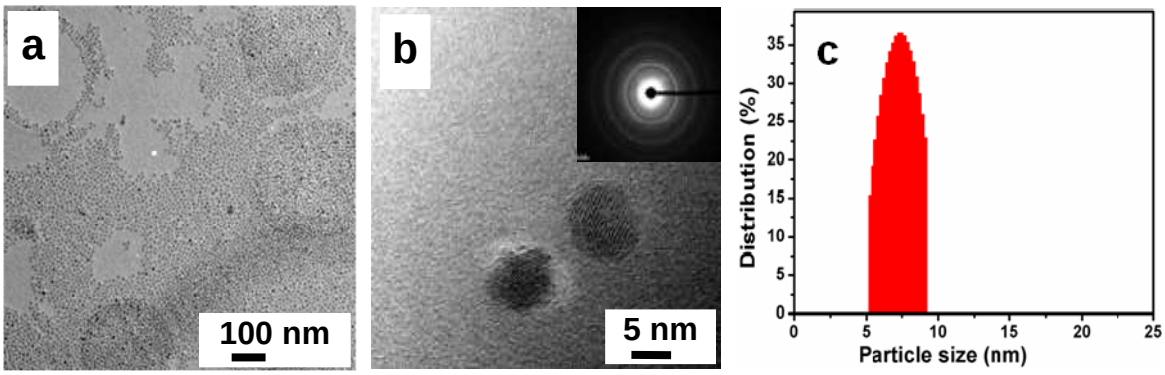

Figure 3.1. *(a) TEM image of a representative sample and (b) HRTEM image of two individual copper ferrite nanoparticles (the inset shows the electron diffraction pattern). (c) Particle size distribution obtained by averaging the sizes of approx. 100 nanoparticles.*

X-ray diffraction data were acquired in order to characterize phase purity of the final product (see Figure 3.2). Particle sizes were estimated by deconvolution of the peak-broadening within the framework of the fundamental parameter approach; they are in good agreement with the values obtained from TEM analysis (average values from approx. 100 individual particles). The observed intensities match well with the cuprospinel structure of $CuFe_2O_4$ (SG 227, $Fd\bar{3}m$); no other phases were detected. XRD analysis provides information on crystallite size rather than particle size (particles could be formed of several crystallite grains). Furthermore, XRD provides an average particle size from a volume average across the whole sample, rather than specific particles. TEM, on the other hand, provides particle size analysis from individual particles observed in a transmission electron micrograph. It provides localized size information from the areas of sample where the images are obtained and the results are number-averaged rather than volume-averaged. For discrete particles, the results of both techniques should match.

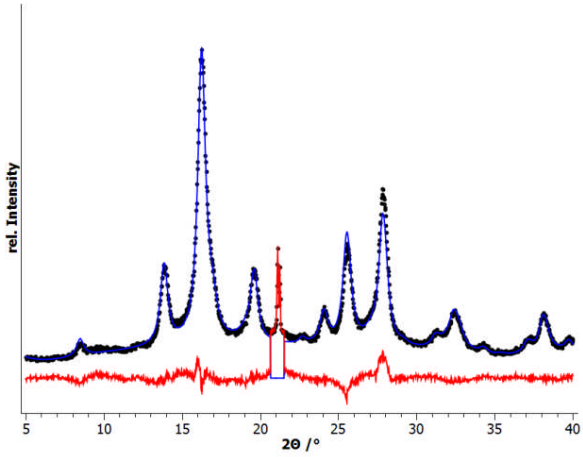

Figure 3.2. *XRD diffraction pattern (black), Rietveld-refinement (blue) and difference curve (red) of "$CuFe_2O_4$" (Bragg maxima at $2\Theta \approx 21°$ are due to the (220) reflection of the Si single crystal used a sample holder).*

Figure 3.3a shows hysteresis loops of 5-7 nm copper ferrite nanoparticles measured at 5 K and at room temperature. With a coercivity of 122 Oe, the nanoparticles show ferrimagnetic properties at 5 K. They are superparamagnetic with no coercivity at room temperature. The magnetization curves in Figure 3.3a exhibit saturation magnetization values of 36.1 (5 K) and 30.5 emu/g (295 K), respectively. These values are somewhat lower than those reported for the bulk material (33.3 emu/g at 300 K) [41, 42]. In bulk $Cu_xFe_{3-x}O_4$, the total saturation moment per formula unit, is related with the degree of inversion δ by $\mu_S = \mu_{Cu} + 2\delta(\mu_{Fe}-\mu_{Cu})$,

where μ_{Fe} and μ_{Cu} are the Fe^{3+} and Cu^{2+} moments, respectively. Taking $\mu_{Fe} = 5\mu_B$ and $\mu_{Cu} = 1$ μ_B, we have $\mu_S = (8\delta + 1)\ \mu_B$ and thus small changes in δ lead to large increments in μ_S (for the exchange of one B-site Cu^{2+} by one A-site Fe^{3+} and vice versa, we have $\delta = 0.125$ and the saturation moment rises from 1 to 2 μ_B.) The magnetic data from Figure 3.3 show that the μ_S values is about 1 μ_B pointing to a degree of inversion of $\delta \approx 0.32$, about 30% of inversion. The inversion is believed to be related to the preparation method, as samples annealed at high temperature exhibit a negligible degree of inversion. Deviations of the thermal and spatial magnetization from the bulk behavior are attributed to size-dependent effects such as surface magnetic disorder [43].

Figure 3.3b shows the zero field-cooled (ZFC)/field-cooled (FC) magnetization curves in the range of 4-300 K. For the ZFC experiment, the sample is cooled in zero field and then heated in a field of (100 Oe) while the net magnetization of the sample is recorded. The FC data are obtained by cooling the sample under the same magnetic field of (100 Oe) after the ZFC experiments and recording the change in net sample magnetization with temperature. The ZFC curve shows a narrow peak at 60 K, indicating the blocking temperature of nanoparticles with mean size. The FC and ZFC curves coincide at high temperatures and start to separate at 67 K, indicating the blocking temperature of the largest particles. The closeness of the blocking temperature and the temperature of the ZFC/FC curves separation indicates the presence of nanoparticles with a narrow size distribution.

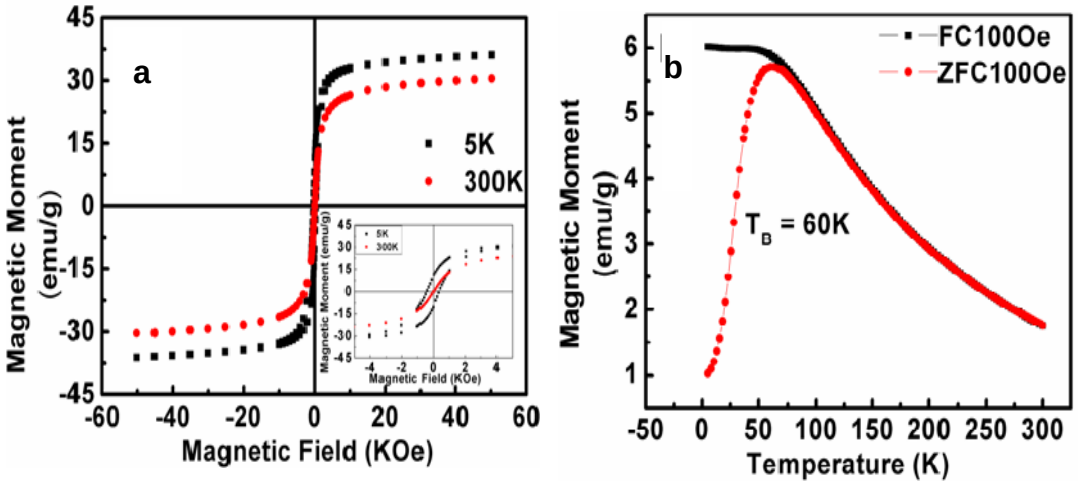

Figure 3.3. *(a) Hysteresis loop of $CuFe_2O_4$ nanoparticles, (b) temperature dependence of magnetization in field cooling (FC) and zero field cooling (ZFC).*

The mössbauer spectrum at room temperature in Figure 3.4a shows a doublet, which is due to the superparamagnetic relaxation effect of the nanoparticles. At 80 K, the relaxation slows down and the spectrum consists of a doublet and a distribution of magnetic sextets (Figure 3.4b). This points towards two different contributions: (i) from superparamagnetic particles and (ii) from particles below the blocking temperature. This is dueto the sharp, yet not singular particle size distribution of (7 ±1) nm. The mössbauer spectra at 4.2 K were fitted using a hyperfine magnetic field distribution model considering the presence of two charge states of Fe atoms (Figure 3.4c). Values of isomer shifts (IS) and average hyperfine magnetic fields (H_{hf}) indicate mainly two sites with IS_1 = 0.507 mms^{-1}, H_{hf1} = 509.9 kOe and IS_2= 0.614 mms^{-1}, H_{hf2} = 468.4 kOe and a very weak, negligible doublet with relative intensities according to S_1 = 53(1)%, S_2 = 45(1)% and S_3 = 2(1)%.

$Cu_xFe_{3-x}O_4$, crystallizes in the magnetite structure type (*cF*56, *Fd*-3*m*) with the metal cations situated in the tetrahedral (8*b*) and octahedral voids (16*c*). At T = 4.2 K the mössbauer spectrum with H_{hf1} = 509.9 kOe and IS_1 = 0.507 mms^{-1}corresponds to iron in tetrahedral coordination in a valence state Fe^{3+}. A subspectrum with IS_2 = 0.614 mms^{-1}, H_{hf2} = 468.4 kOe stems from valence states $Fe^{2.5+}$ which are due to the electronic exchange between Fe^{2+} and Fe^{3+} in the octahedral voids [44].

Taking the pairwise coupling of Fe^{3+} and Fe^{2+} in the octahedral voids into account, one may rewrite the general composition $Cu_xFe_{3-x}O_4$ as $\{Cu^{2+}_{1-y}Fe^{3+}_{y}\}_{tet}\{Fe^{2.5+}_{2(y-z)}Fe^{3+}_{2-2y+z}Cu^{2+}_{z}\}_{oct}O_4$. Only a part of the Fe^{3+} species on the octahedral sites, namely *(y-z)*, is coupled to Fe^{2+}. The remaining Fe^{3+} ions couple into the contribution of Fe^{3+} on the tetrahedral sites. Thus, the intensity ratio of the $Fe^{2.5+}$ and Fe^{3+} fractions in the mössbauer spectrum at 4.2 K corresponds to

$$\frac{S_2}{S_1} = \frac{2(y-z)}{2-y+z}$$

According to the x-ray diffraction data, the fraction of Cu^{2+} in the tetrahedral positions is *(1-y)* = 0.32(8). With S_2/S_1 = 0.85(3) the amount of Cu^{2+} in the octahedral voids is *z* = 0.08(6), which is in fair agreement with the value of 0.0(1) determined from the x-ray structure analysis. In summary, the sample is best described as a Cu-doped Fe_3O_4: $(Cu^{2+}_{0.32}Fe^{3+}_{0.68})_A(Fe^{2+}_{0.6}Fe^{3+}_{1.32}Cu^{2+}_{0.08})_BO_4$.

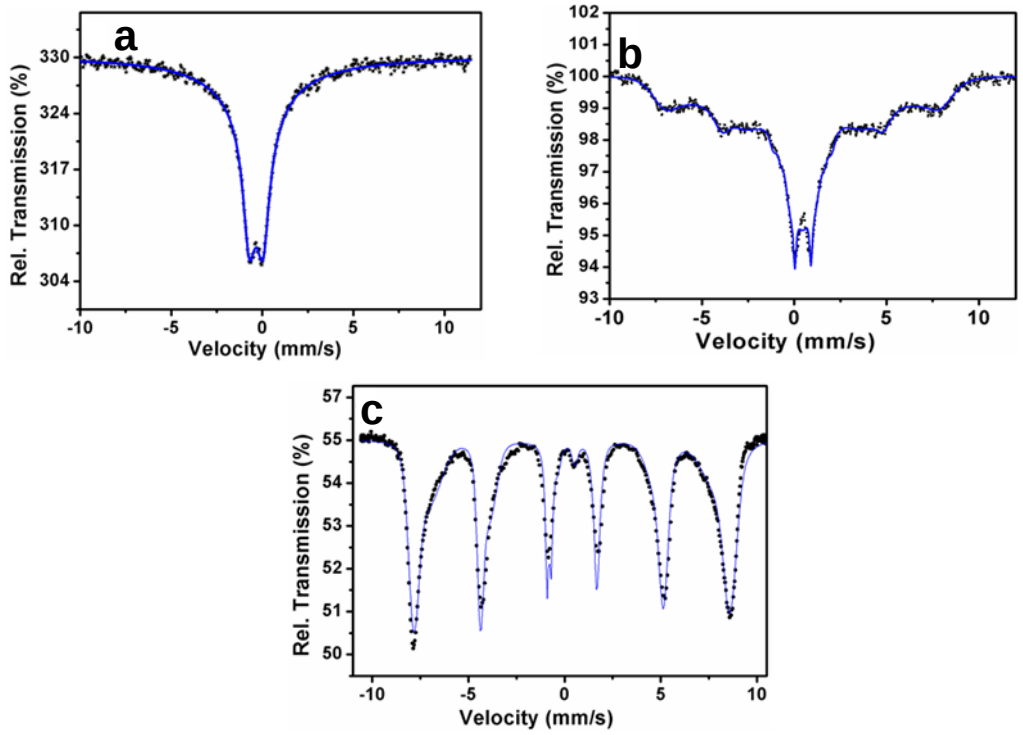

Figure 3.4. *^{57}Fe Mössbauer spectra of a nanopowder $Cu_xFe_{3-x}O_4$ recorded at (a) 295 K, (b)80 K and (c) 4.2 K.*

To explore the potential applications of the $Cu_xFe_{3-x}O_4$ magnetic nanoparticles, their surface was tailored using a multifunctional polymeric ligand which contains dopamine as an anchor group for metal oxide surface [45-48], amine groups for further immobilization of biomolecules and *7*-nitrobenzofurazan (NBD) as fluorophore (Figure 3.5a). After the surface functionalization processes, the $Cu_xFe_{3-x}O_4$ nanoparticles showed good water solubility and stability at room temperature (Figure 3.5b). These spherical nanoparticles were characterized by epiflurescence microscopy to confirm the polymer functionalization with the aid of the NBD fluorophore conjugated to the backbone of the polymeric ligand. The respective emission can be seen visually and almost all nanoparticles emit green color (Figure 3.5c). The fluorescence of the dye molecules was excited at 513 nm and detected at 540 nm using a 20 fold dry objective. Furthermore, the surface functionalization was confirmed using FT-IR measurements as demonstrated in Appendix 3. As prepared $Cu_xFe_{3-x}O_4$ nanoparticles (black line) exhibit characteristic vibrational bands of the oleate group. Most notably, the asymmetric and symmetric stretching bands of the $RCOO^-$ group appear at 1543 and 1400 cm^{-1}, respectively. However, these bands are

absent in the spectra of polymeric ligand functionalized $Cu_xFe_{3-x}O_4$ nanoparticles respectively, indicating a complete replacement of the oleate layer by the hydrophilic ligands. Furthermore, the appearance of vibrational bands at 1677 cm^{-1}, 1296, 1251 and 1098 cm^{-1} in the spectra functionalized nanoparticles spectra, which can be assigned to the stretching modes of C=O of amide groups present in the polymeric ligand and C–O–C ether groups in PEG also present in the polymeric ligands.

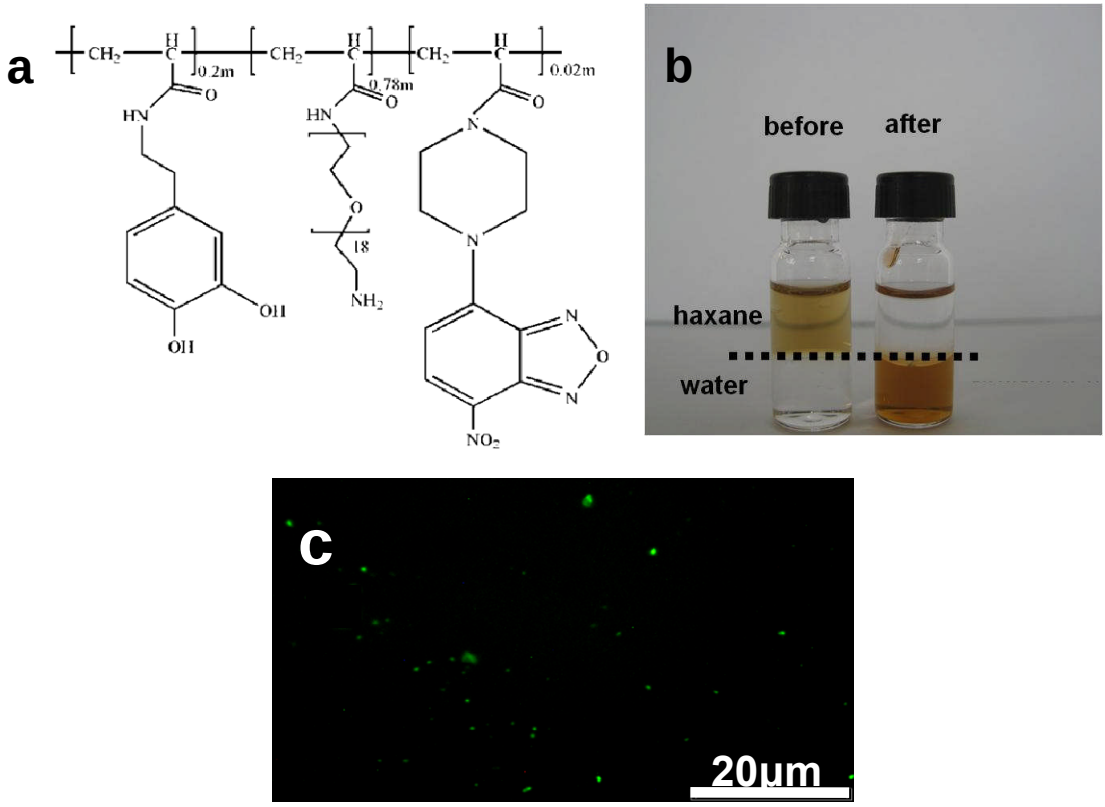

Figure 3.5. *(a) Schematic representation of multifunctional copolymer containing 3-hydroxytyramine (dopamine) as an anchor group for the binding of metal oxides, pip-NBD as a fluorophore and PEG chains containing amine group to improve the solubility of functionalized nanoparticles. (b) Digital photograph of $Cu_xFe_{3-x}O_4$ solutions before (left) and after (right) ligand exchange in hexane (top layer) and in water (bottom layer). (c) Fluorescence microscope images of NBD-polymer functionalized $Cu_xFe_{3-x}O_4$ nanoparticles (green fluorescence).*

The ^{1}H-NMR relaxometry characterization (i.e., NMR dispersion profile) was performed at room temperature by measuring the longitudinal and the transverse nuclear relaxation times

T_1 and T_2, in the frequency range 10 kHz ≤ ν ≤ 65 MHz for T_1 and 15 MHz ≤ ν ≤ 60 MHz for T_2 (see experimental part). Measurements at room and physiological temperatures gave identical results within 10%. The efficiency of the MRI contrast agents is determined by measuring the nuclear relaxivities $r_{1,2}$ defined as $r_i = [\ (1/T_i)_{meas} - (1/T_i)_{dia}\ ]/c$ (i = 1,2) where $(1/T_i)_{meas}$. Figure 3.6 shows T_1 and T_2-weighted MR images for 3 different concentrations of polymer functionalized $Cu_xFe_{3-x}O_4$ nanoparticles and saline solution (0.9% NaCl) for comparison. Their concentrations in saline solution were 0.0091, 0.0229 and 0.0366 mM, respectively. The r_1 and r_2 relaxitivities of polymer functionalized nanoparticles are 0.0267 and 0.259 ($s^{-1}mM^{-1}$), respectively. Such values for r_1 and r_2 show that the polymer functionalized copper ferrite $Cu_xFe_{3-x}O_4$ nanoparticles can act both as T_1 and T_2 contrast agents. Our system of $Cu_xFe_{3-x}O_4$ nanoparticles, with respect to size and surface functionalities, is similar to the one reported by Weller and coworkers in showing both T_1 and T_2 contrast [49]. Thus, after appropriate surface functionalization, $Cu_xFe_{3-x}O_4$ nanoparticles may be considered a promising candidate for molecular imaging when addressed to specific cells.

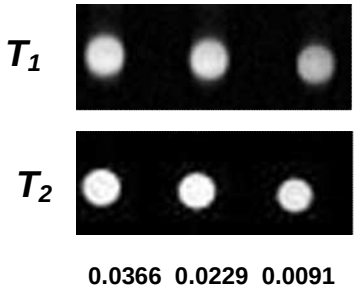

Figure 3.6. *T_1 and T_2 weighted MRI images of solutions containing polymer functionalized $Cu_xFe_{3-x}O_4$ nanoparticles (concentrations in mM Fe).*

3.3. Summary and Outlook

In summary, non-agglomerated and monodisperse superparamagnetic copper ferrite $Cu_xFe_{3-x}O_4$ nanoparticles were prepared and characterized by electron microscopy, x-ray diffractometery, magnetic susceptibility measurements and mössbauer spectroscopy. The detailed composition of the nanoparticles as well as the site preference of the metal atoms could be determined by a combination of the diffraction, magnetometry and mössbauer spectroscopy. The inversion is believed to

be related to the preparation method, as samples annealed at high temperature exhibit a negligible degree of inversion. The $Cu_xFe_{3-x}O_4$ particles could be functionalized using hydrophilic polymeric ligand. Efficient surface binding of the ligand molecules was confirmed by FT-IR and UV-Vis analysis. In comparison to the previously reported nanoparticles, the present nanoparticles are monodisperse, size controlled and present good stability due to the covalent anchorage of the PEG-polymer to the surface of the nanoparticles. Finally, we demonstrated that by virtue of their magnetic properties functionalized $Cu_xFe_{3-x}O_4$ nanoparticles exhibit a moderate T_1 and a strong T_2 contrast enhancement effect for MRI. These results certify that our approach is a promising way towards new superparamagnetic MRI contrast agents which by virtue of the multifunctional polymer coating can be designed for the specific targeting of cells.

3.4. Experimental Section

Methods and Material

Iron(0) pentacarbonyl ($Fe(CO)_5$, 99.5%, 1-octadecene (ODE, 90%, Acros), copper(II) formate $Cu(HCOO)_2$, (99%, Fluka), oleic acid (90%, Aldrich), oleylamine (90%, Acros), di-tert-butyl dicarbonate ($(Boc)_2O$), >99%, Aldrich), dioxane (p.A. Fisher), $H_2N\text{-}PEG_{(800)}\text{-}NH_2$ (Aldrich), triethylamine (>99%, Aldrich), 3-hydroxy tyramine hydrochloride (Dopamine·HCl, 98%, Aldrich), NBD chloride (98%, Fluka), trifluoroacetic acid (TFA) (99%, Aldrich), ethanol (99.8%, Roth), toluene(>99%, Aldrich), hexane (p.A. Fisher), dichloromethane (DCM) (p.A. Fisher), *N*,*N*-dimethylformamide ((DMF) extra dry, >99.8%, Acros), diethyl ether (p.A. Fisher) were used as received without further purification.

Synthesis of $Cu_xFe_{3-x}O_4$ Nanoparticles

In a typical synthesis, under highly inert conditions 5 mL of octadecane, 0.195 mL of oleylamine and 0.5415 mL of oleic acid were mixed and heated to 100 ºC for 45 min. In a separate flask were added 2 mL of oleylamine and 550 mg of $Cu(HCOO)_2$ and the flask was placed in a liquid metal bath at room temperature and programmed to reach 75ºC at a heating rate 3ºC/min. At this temperature, $Cu(HCOO)_2$ solution from this flask was injected into the other flask containing mixed surfactant solution and the temperature was increased with the same rate. After reaching to 120ºC, 0.975 mL of $Fe(CO)_5$ were injected into the mixture. Subsequently, the solution was heated to 200ºC and kept at this temperature for 1 h. Throughout this period Ar was kept flowing through the flask and the mixture was stirred

mechanically. Finally, the mixture was cooled to room temperature, the product was separated by precipitation with ethanol and centrifugation using 9000 rpm for 10 min and re-dispersed in hexane several times.

Synthesis of the Dopa-PEG-Polymer (DA-PEG-PP)

N-Boc-NH_2-$PEG_{(800)}$-NH_2. N-Boc-NH_2-$PEG_{(800)}$-NH_2 was synthesized according to procedure as described [50]. The poly (active ester) poly(pentafluorophenyl acrylate) (PFA) was prepared as reported earlier [51-54]. GPC analysis of the obtained polymer (THF, light scattering detection) gave the following values: M_n = 16,390 g/mol, PDI = 1.39, with an average of 70 repeat units. For the synthesis of the multifunctional poly(acrylamides), poly(active ester) poly(pentafluorophenyl acrylate) (700 mg, 2.94 mmol repeating units) was dissolved in a mixture of 9 mL of dry DMF and 0.7 mL of triethylamine. 12 mg of pip-NBD was added to the solution and stirred for 2 h. Subsequently, 3-hydroxytyramine hydrochloride (24 mg) dissolved in 3 mL of DMF and 0.4 mL of triethylamine was added and the reaction mixture was stirred for 3 h at 50°C. In the final step the remaining active ester groups were substituted using an excess of N-Boc-$PEG_{(800)}$-NH_2 (dissolved in 3 mL of dry DMF) and stirring for 5 h at 50°C. The solution was concentrated to about 2 mL and the polymeric ligand was precipitated by addition of cold ethyl ether. The precipitated polymer was centrifuged and the solvent was decanted. Upon drying, 486 mg of colorless oil was obtained.
The polymer obtained above was dissolved in CH_2Cl_2 (30 mL). Subsequently, trifluoroacetic acid (2.0 mL) was added and the mixture was stirred at room temperature for 2 h. Afterwards the reaction solution was treated with a mixture of water and hexane (30 mL/50 mL) and stirred vigorously for 30 min. The aqueous phase containing the polymer was separated and concentrated to 2 mL and dialyzed against deionized water for 2 days (cellulose bag, MWCO = 3,500). Finally, the water was evaporated and the product was re-dissolved in chloroform to make a stock solution which was kept in the refrigerator.

DA-PEG-NH_2. Conjugation of N-Boc-PEG-NH_2 to 3,4 dihydroxyhydrocinnamic acid (DA) was performed by a common DCC coupling reaction under inert conditions. First, 3,4-dihydroxyhydrocinnamic acid (5 mmol) and HOBt (5.1 mmol) were dissolved in 10 ml of dry DMF and stirred at room temperature. After 10 minutes DCC (5.1 mmol in 10 ml of dry DMF) were added and the solution was stirred for another 10 minutes before NHS (5.1 mmol in 10 ml of dry DMF) was added dropwise over a period of 30 minutes. The reaction was continued for 2 hours. The resulting DA-NHS ester was subsequently added to a stirred solution of NBoc-PEG-NH_2 (5 mmol) in 15 ml of dry DMF over a period of 45 minutes. The

solution was stirred overnight at room temperature. After removal of the urea side product by filtration the crude product was transferred to chloroform. The organic solution was extracted several times with a saturated NaCl solution and washed with deionized water. The solvent was evaporated and the oily residue redissolved in dichloromethane. Cleavage of the BOC protection group was accomplished by addition of trifluoroacetic acid and stirring at room temperature for two hours. After removal of DCM the product was dissolved in 40 ml of chloroform and washed with a saturated aqueous $NaHCO_3$ solution and deionized water. The organic phase was dried over $MgSO_4$ and the solvent removed *in vacuo* to produce a light brown oil.

Functionalization of the $Cu_xFe_{3-x}O_4$ Nanoparticles

10 mg of $Cu_xFe_{3-x}O_4$ nanoparticles dispersed in 15 mL of chloroform were dropped slowly over 1 h into the above synthesized polymeric ligand solution (20 mg in 10 mL of chloroform). The reaction was stirred continuously at room temperature, overnight under inert conditions. The functionalized nanoparticles were precipitated by addition of hexane und separated from unbound polymer and surfactants by centrifugation. The nanoparticles were washed twice by dissolving them in chloroform and precipitation with hexane. Finally, the particles were stored in DMF in a refrigerator.

The functionalized $Cu_xFe_{3-x}O_4$ nanoparticles were characterized by TEM and Fourier Transform Infrared (FT-IR) spectroscopy (Mattson Instruments 2030 Galaxy-FT-IR spectrometer). Unless mentioned differently, all nanoparticle concentrations are referred to the Fe concentration measured with AAS.

Physical Characterization

Electron Microscopy

The size and morphology of the naked and surface functionalized $Cu_xFe_{3-x}O_4$ nanoparticles were investigated using transmission electron microscopy (TEM, Philips EM 420 instrument with an acceleration voltage of 120 kV). Samples for transmission electron microscopy were prepared by placing a drop of dilute nanoparticle solution in hexane on a carbon coated nickel grid. Low-resolution TEM images were recorded on a Philips EM420 microscope operating at an acceleration voltage of 120 kV. High-resolution TEM data and ED patterns were obtained on a FEI Tecnai F30 S-TWIN with a 300 kV field emission gun.

X-Ray Diffraction

X-ray powder diffraction measurements were performed on a Bruker D8 Advance powder diffractometer operating with Mo-Kα radiation and a Sol-X energy-dispersive detector. Samples were prepared as loose powder on nearly background free Si-single crystal plates. Full pattern profile fits were performed with TOPAS Academic V4.1 applying the fundamental parameter approach [55, 56] according to the structure models of Cu_2O [57], Cu [58] and $CuFe_2O_4$ [59]. Background, lattice parameters, crystallite sizes, scale factors and the partial occupation factors of Cu and Fe on the 8*b* and 16*c* sites of $CuFe_2O_4$ were refined. In order to avoid local minima, the latter ones were repeatedly attributed to random numbers between 0 and 1 and refined in a set of overall 10^6 iterations.

Mössbauer Spectroscopy and Superconducting Quantum Interference Device

Mössbauer spectra were obtained at room temperature 110 K and 80 K with a constant acceleration transmission mössbauer spectrometer and ^{57}Co (Rh) source. A α-Fe foil was used to calibrate the mössbauer spectrometer in a velocity range of ±12 mms^{-1}. Magnetic measurements were carried out using a Quantum Design MPMS-XL SQUID magnetometer.

Magnetic Resonance Imaging

MR signal enhancement effects were measured for the aqueous solutions of functionalized $Cu_xFe_{3-x}O_4$ nanoparticles at different Fe concentrations (measured with AAS) on a clinical 3.0 T MRI scanner (Magnetom Trio, Siemens Medical Solutions, Erlangen, Germany). Signal reception and radio frequency (RF) excitation was performed using 8-channel knee coil. For T_1-measurement, a saturation prepared (SR) snapshot fast low angle shot (SR-TurboFLASH) pulse sequence with repetition time (T_R) / echo time/ flip angle = 3.0 ms/1.5 ms/20° was used with varying saturation times starting from 20 ms up to 8000 ms. For measuring the T_2 relaxation time, a multi-echo spin-echo pulse sequence (CPMG, Carr-Purcell-Meiboom-Gill) with a total of 32 echos and T_R = 5000 ms was used, the echo time was varied from 7 ms to 224 ms. In a second T_2 measurement T_E was varied from 15 ms up to 480 ms.

3.5. References

[1] Q. A. Pankhurst, N. K. T. Thanh, K. Jones and J. Dobson, *J. Phys. D: Appl. Phys*. **2009**, *42*, 224001.

[2] M. Arruebo, R. Fernández-Pacheco, M. R. Ibarra and J. Santamaría, *Nanotoday* **2007**, *2*, 22.

[3] J. M. Perez, F. J. Simeone, Y. Saeki, L. Josephson and R. Weissleder, *J. Am. Chem. Soc.* **2003**, *125*, 10192.

[4] D. L. Graham, H. A. Ferreira and P. P. Freitas, *Trends Biotechnol.* **2004**, *22*, 455.

[5] S. Bucak, D. A. Jones, P. E. Laibinis and T. A. Hatton, *Biotechnol. Prog.* **2003**, *19*, 477.

[6] (a) H. Gu, P. L. Ho, K. W. T. Tsang, L. Wang and B. Xu, *J. Am. Chem. Soc.* **2003**, *125*, 15702. (b) M. I. Shukoor, F. Natalio, A. Krasko, H. C. Schröder, W. E. G. Müller and W. Tremel *Chem. Commun.* **2007**, *44*, 4677.

[7] J. W. M. Bulte, T. Douglas, B. Witwer, S.-C. Zhang, E. Strable, B. K. Lewis, H. Zywicke, B. Miller, P. Van Gelderen, B. M. Moskowitz, L. D. Duncan and J. A. Frank, *Nat. Biotechnol.* **2001**, *19*, 1141.

[8] M. Lewin, N. Carlesso, C.-H. Tung, X. W. Tang, D. Cory, D. T. Scadden and R. Weissleder, *Nat. Biotechnol.* **2000**, *18*, 410.

[9] R. Hiergeist, W. Andra, N. Buske, R. Hergt, I. Hilger, U. Richter and W. Kaiser, *J. Magn. Magn. Mater*. **1999**, *201*, 420.

[10] (a) Y.-W. Jun, Y.-M. Huh, J.-S. Choi, J.-H. Lee, H.-T. Song, S. Kim, S. Kim, S. Yoon, K.-S. Kim, J.-S. Shin, J.-S. Suh and J. Cheon, *J. Am. Chem. Soc*. **2005**, *127*, 5732. (b) Z. Medarova, W. Pham, C. Farrar, V. Petkova and A. Moore, *Nat. Med.* **2007**, *13*, 172.

[11] A. Jordan, R. Scholz, P. Wust, H. Fahling and R. Felix, *J. Magn. Magn. Mater*. **1999**, *201*, 413.

[12] I. Hilger, R. Hiergeist, R. Hergt, K. Winnefeld, H. Schubert and W. Kaiser, *Invest. Radiol.* **2002**, *37*, 580.

[13] U. Haefeli, W. Schuett, J. Teller and M. Zborowski, *Scientific and Clinical Applications of Magnetic Carriers*; Plenum: New York, **1997**.

[14] R. C. O'Handley, *Modern Magnetic Materials: Principles and Applications*; Wiley: New York, **2000**.

[15] V. Sepelak, I. Bergmann, A. Feldhoff, P. Heitjans, F. Krumeich, D. Menzel, F. J. Litterst, S. J. Campbell and K. D. Becker. *J. Phys. Chem.* C **2007**, *111*, 5026.

[16] (a) A. J. Rondinone, A. C. S. Samia and Z. J. Zhang, *J. Phys. Chem. B* **1999**, *103*, 6876. (b) C. Liu, B. Zou, A. J. Rondinone and Z. J. Zhang, *J. Am. Chem. Soc.* **2000**, *122*, 6263.

[17] (a) C. Yao, Q. Zeng, G. F. Goya, T. Torres, J. Liu, H. Wu, M. Ge, Y. Zeng, Y. Wang and J. Z. Jiang, *J. Phys. Chem. C* **2007**, *111*, 12274. (b) M. Sivakumar, T. Takami, H. Ikuta, A. Towata, K. Yasui, T. Tuziuti, T. Kozuka, D. Bhattacharya and Y. Iida, *J. Phys. Chem. B* **2006**, *110*, 15234.

[18] (a) A. J. Rondinone, C. Liu and Z. J. Zhang, *J. Phys. Chem. B* **2001**, *105*, 7967. (b) S. Sun, H. Zeng, D. B. Robinson, S. Raoux, P. M. Rice, S. X. Wang and G. Li, *J. Am. Chem. Soc.* **2004**, *126*, 273. (c) H. Deng, X. Li, Q. Peng, X. Wang, J. Chen and Y. Li. *Angew. Chem. Int. Ed.* **2005**, *44*, 2782. (d) E. Kang, J. Park, Y. Hwang, M. Kang, J.-G. Park and T. Hyeon, *J. Phys. Chem. B* **2004**, *108*, 13932.

[19] (a) J. Lee, Y.-M. Huh, Y. Jun, J. Seo, J. Jang, H. Song, S. Kim, E. Cho, H. Yoon, J. Suh and J. Cheon, *Nat. Med.* **2007**, *13*, 95. (b) C. Liu, B. Zou, A. J. Rondinone and Z. J. Zhang, *J. Phys. Chem. B* **2000**, *104*, 1141.

[20] (a) J. B. Goodenough, *Magnetism and the Chemical Bond*; Wiley: New York, **1963**. (b) J.-T. Jang, H. Nah, J.-H. Lee, S. H. Moon, M. G. Kim and J. Cheon, *Angew. Chem. Int. Ed*. **2009**, *48*, 1234.

[21] C. M. B. Henderson, J. C. Charnock and D. A. Plant, *J. Phys.: Condens. Matter* **2007**, *19*, 076214/1.

[22] M. H. Nilsen, C. Nordhei, A. L. Ramstad, D. G. Nicholson, M. Poliakoff and A. Cabanas, *J. Phys. Chem. C* **2007**, *111*, 6252.

[23] D. Vollath, *Nanomaterials*; Wiley-VCH: Weinheim, **2008**.

[24] J. A. Gomes, M. H. Sousa, G. J. da Silva, F. A. Tourinho, J. Mestnik-Filho, R. Itri and J. Depeyrot, *J. Magn. Magn. Mater.* **2006**, *300*, e213.

[25] Z. Huang, Y. Zhu, J. Zhang and G. Yin, *J. Phys. Chem. C* **2007**, *111*, 6821.

[26] J. Q. Qi, W. P. Chen, M. Leu, Y. Wang, H. Y. Tian, L. T. Li and H. L. W. Chan, *Nanotechnology* **2005**, *16*, 3097.

[27] J. Du, Z. Liu, W. Wu, Z. Li, B. Han and Y. Huang, *Mater. Res. Bull.* **2005**, *40*, 928.

[28] (a) M. Banerjee and A. Rai, *J. Nanosci. Nanotechnol.* **2007**, *7*, 1990. (b) N. S. Gajbhiye, G. Balaji, S. Bhattacharyya and M. Ghafari, *Hyperfine Interact.* **2004**, *57*, *156.* (c) D. Thapa, N. Kulkarni, S. N. Mishra, P. L. Paulose and P. Ayyub, *J. Phys. D: Appl. Phys.* **2010**, *43*, 195004.

[29] G. F. Goya, *J. Mater. Sci. Lett.* **1997**, *16*, 563.

[30] (a) N. Rajic, M. Ceh, R. Gabrovsek and V. Kaucic, *J. Am. Ceram. Soc.* **2002**, *85*, 1719. (b) T. Valdes-Solis, P. Tartaj, G. Marbanand and A. B. Fuertes, *Nanotechnology* **2007**, *18*, 145603/1.

[31] S. Roy and J. Ghose, *J. Magn. Magn. Mater.* **2006**, *307*, 32.

[32] (a) G. F. Goya, H. R. Rechenberg and J. Z. Jiang, *J. Appl. Phys.* **1998**, *84*, 1101. (b) J. Z. Jiang, G. F. Goya and H. R. Rechenberg, *J. Phys.: Condens. Matter.* **1999**, *11*, 4063.

[33] A. Laobuthee, S. Wongkasemjit, E. Traversa and R. M. Laine, *J. Eur. Ceram. Soc.* **2000**, *20*, 91.

[34] U. Lüders, M. Bibes, K. Bouzehouane, E. Jacquet, J. P. Contour, S. Fusil, J. F. Bobo, J. Fontcuberta A. Barthelemy and A. Fert, *J. Appl. Phys*. **2006**, *99*, 08 K301.

[35] D. Fino, N. Russo, G. Saracco and V. Specchia, *J. Catal*. **2006**, *242*, 38.

[36] Y. Tanaka, T. Ukata, R. Kikuchi, T. Takeguchi, K. Sasaki and K. Eguchi, *J. Catal.* **2003**, *215*, 271.

[37] S. Kameoka, T. Tanabe and A. P. Tsai, *Catal. Lett.* **2005**, *100*, 89.

[38] K. Faungnawakij, Y. Tanaka, N. Shimoda, T. Fukunaga, S. Kawashima, R. Kikuchi and K. Eguchi, *Appl. Catal. A* **2006**, *304*, 40.

[39] K. Faungnawakij, R. Kikuchi, N. Shimoda, T. Fukunaga and K. Eguchi, *Angew. Chem*. **2008**, *120*, 9454.

[40] M. Estrella, L. Barrio, G. Zhou, X. Wang, Q. Wang, W. Wen, J. C. Hanson, A. I. Frenkel and J. A. Rodriguez, *J. Phys. Chem. C* **2009**, *113*, 14411.

[41] B. J. Evans and S. Hafner, *J. Phys. Chem. Solids* **1968**, *29*, 1573.

[42] D. Bonacchi, A. Caneschi, D. Dorignac, A. Falqui, D. Gatteschi, D. Rovai, C. Sangregorio and R. Sessoli, *Chem. Mater.* **2004**, *16*, 2016.

[43] H. Kachkachi, A. Ezzir, M. Nogues and E. Tronc, *Eur. Phys. J. B* **2000**, *14*, 681.

[44] N. N. Greenwood and T. G. Gibb, *Mössbauer Spectroscopy*; Chapman and Hall Ltd: London, **1971**.

[45] A. S. Goldmann, C. Schödel, A. Walther, J. Yuan, K. Loos and A. H. E. Müller, *Macromolecular Rapid Communications* **2010**, *31*, 1608.

[46] F. Natolio, I. Shukoor, V. Ksenofontov, H. C. Schröder, W. E. G. Müller and W. Tremel, *Small* **2007**, *3*, 1734.

[47] M. I. Shukoor, F. Natoli, N. Glube, M. N. Tahir, H. A. Therese, V. Ksenofontov, N. Metz, P. Theato, P. Langguth, J. P. Boissel, H. C. Schröder, W. E. G. Müller and W.

Tremel, *Angew. Chem., Int. Ed.* **2008**, *47*, 4748.

[48] (a) W. Kaim and B. Schwederski, *Bioanorganische Chemie*; Teubner: Stuttgart, **1991**. (b) W. Kaim and B. Schwederski, *Coord. Chem. Rev.* **2010**, *254*, 1580.

[49] U. I. Tromsdorf, O. T. Bruns, S. C. Salmen, U. Beisiegel and H. Weller, *Nano Lett.* **2009**, *9*, 4434.

[50] T. D. Schladt, K. Schneider, M. I. Shukoor, F. Natalio, H. Bauer, M. N. Tahir, S. Weber, L. M. Schreiber, H. C. Schröder, W. E. G. Müller and W. Tremel, *J. Mater. Chem*. **2010**, *20*, 8297.

[51] I. Potavova, R. Mruk, S. Prehl, R. Zentel, T. Basche and A. Mews, *J. Am. Chem. Soc.* **2003**, *125*, 320.

[52] M. Eberhardt, R. Mruk, P. Theato and R. Zentel, *Eur. Polym. J.* **2005**, *41*, 1569.

[53] M. N. Tahir, M. Eberhardt, H. A. Therese, U. Kolb, P. Theato, W. E. G. Müller, H. C. Schröder and W. Tremel, *Angew. Chem. Int. Ed.* **2006**, *45*, 4803.

[54] M. N. Tahir, M. Eberhardt, P. Theato, S. Faiß, A. Janshoff, T. Gorelik, U. Kolb and W. Tremel, *Angew. Chem. Int. Ed.* **2006**, *45*, 908.

[55] A. Coehlo, *Topas Academic V 4.1, Coelho Software*; Brisbane: AUS, **2007**.

[56] R. W. Cheary and A. A. Coelho, *J. Appl. Cryst.* **1992**, *25*, 109.

[57] A. Kirfel and K. Eichhorn, *Acta Crystallogr. A* **1996**, *46*, 271.

[58] S. H. Lee, K. P. Chae, Y. B. Lee and K. S. Oh, *Solid State Commun.* **1990**, *74*, 1.

[59] W. L. Bragg, *Philos. Mag.* **1914**, *28*, 355.

4. Controlling Phase Formation in Solids: Rational Synthesis of Phase Separated Co@Fe_2O_3 Heteroparticles and $CoFe_2O_4$ Nanoparticles

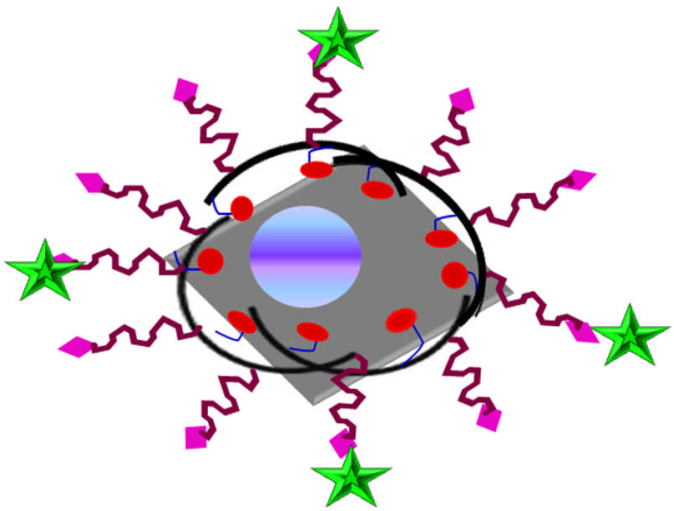

Bahar Nakhjavan[a], Muhammad Nawaz Tahir[a*], Martin Panthöfer[a], Haitao Gao[a], Teuta Gasi[a], Vadim Ksenofontov[a], Robert Branscheid[b], Stefan Weber[c], Ute Kolb[b], Laura Maria Schreiber[c] and Wolfgang Tremel[a*]

[a]*Institut für Anorganische Chemie und Analytische Chemie, Johannes Gutenberg-Universität, Duesbergweg 10-14, D-55099 Mainz, Germany. Fax: +49 6131 39-25605; Tel: +49 6131 39-25135; E-mail: tremel@uni-mainz.de*

[b]*Institut für Physikalische Chemie, Johannes Gutenberg-Universität, Welderweg 11, 55099 Mainz, Germany.*

[c]*Bereich Medizinische Physik, Klinik und Poliklinik für diagnostische und interventionelle Radiologie, Klinikum der Johannes Gutenberg-Universität Mainz. Langenbeckstraße, 1, 55131, Mainz, Germany.*

Chem. Commun. **2011**, *47*, 8898-8900

4.1. Introduction

A long-term goal of solid-state chemists has been to develop comparable kinetic control in the synthesis of new compounds as molecular chemists. Typically, the dominant step of a solid-state reaction needs extended heating at elevated temperature during which the reactants rearrange to form the thermodynamically favored reaction product [1]. High temperature annealing is needed to overcome the diffusion barrier, the limiting key step of solid-state reactions. Kinetic control of a solid-state reaction could be achieved, if diffusion were eliminated as the rate-limiting step and other reaction parameters, such as composition or precursor structure allowed controlling the nucleation event.

Recently, several multicomponent NPs containing a metal and a metal oxide component with different compositions like Pt@Fe_3O_4 [2], Au@Fe_3O_4 [3], Cu@Fe_3O_4 [4], Ag@Fe_3O [5], Au@MnO [6], Pd-Fe_3O_4 [7], CdSe/CdTe/ZnSe [8] with different shapes were reported and received much attention [9]. As the ternary phase diagrams of metals such as Au, Ag or Pt do not contain a significant number of ternary oxide phases, the formation of these heteroparticles by phase separation may be rationalized, but for iron group metals it is very surprising [10]. Other than these, multicomponent NPs, ferrites with the general formula MFe_2O_4 are well established [11].

Wet chemical synthesis of nanoparticles (NPs) offers a unique tool to control the kinetics of phase equilibria, because diffusion barriers become irrelevant on the nanometer scale [12]. As a result, the sequence of phases formed here depends on their relative activation energies for nucleation and compounds in the equilibrium phase diagram may temporarily be skipped if their nucleation energy is too large [13]. In principle, eliminating the diffusion control of a reaction allows studying the sub-solidus regime of phase diagrams. We demonstrate this here by the synthesis of phase separated heteroparticles Co@Fe_2O_3 and the ternary phase $CoFe_2O_4$.

4.2. Results and Discussion

Scheme 4.1 illustrates the course of events. In the first step, Co is nucleated homogeneously, while Fe_2O_3 is nucleated heterogeneously in the second step onto the preformed cobalt NPs that keep on growing with time as shown in Scheme 4.1-i. In contrast, when both reactants are added together, the homo-geneous nucleation and interdiffusion of both components leads to the formation of the ternary phase as shown in Scheme 4.1-ii.

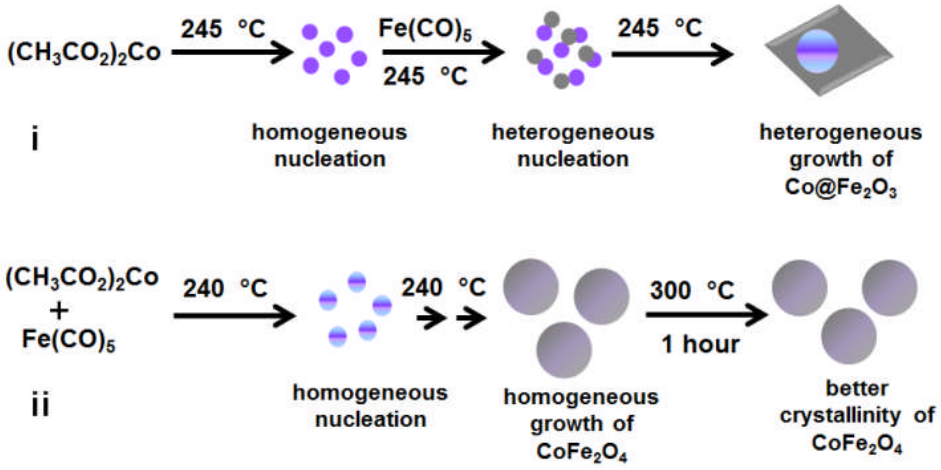

Scheme 4.1. *Demonstration of the synthesis of Co@Fe_2O_3 heterodimer NPs with a rhombohedral shape and spherical $CoFe_2O_4$ NPs.*

Figure 4.1a and b show transmission electron microscopy (TEM) and high resolution (HR) TEM images of the Co@Fe_2O_3 heterodimer NPs with a spherical Co component (Ø ≈ 6-7 nm, darker) attached to a rhombohedral Fe_2O_3 domain (Ø ≈ 15-18 nm, brighter contrast). Figure 4.1c and d show overview TEM and HRTEM images of uniform and monodisperse $CoFe_2O_4$ NPs (average size ~7 nm).

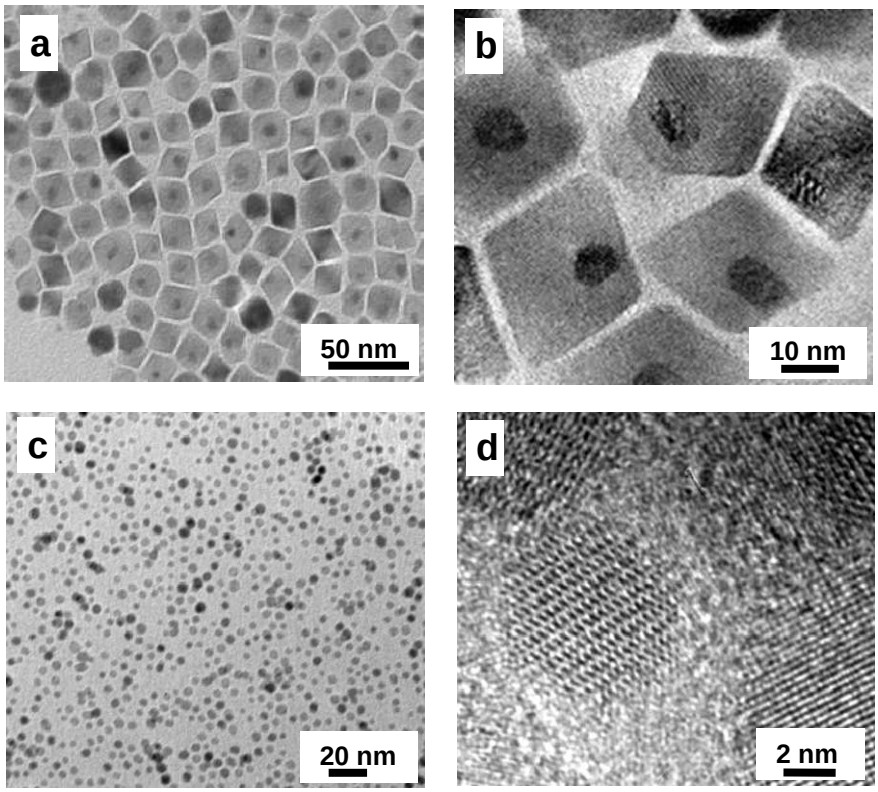

Figure 4.1. *(a & b) Transmission electron microscopy (TEM) and high resolution (HRTEM) images of Co@Fe_2O_3 NPs with rhombohedral Fe_2O_3 domain. (c & d) Overview TEM image and HRTEM image of $CoFe_2O_4$ NPs.*

The elemental composition was determined by line scan EDX (Figure 4.2) using scanning transmission electron microscopy (STEM) combined with energy dispersive x-ray spectroscopy. Due to its higher electron, density cobalt showed a higher contrast than iron oxide. The structure of $CoFe_2O_4$ nanoparticles is also confirmed by electron diffraction pattern (Figure 4.3).

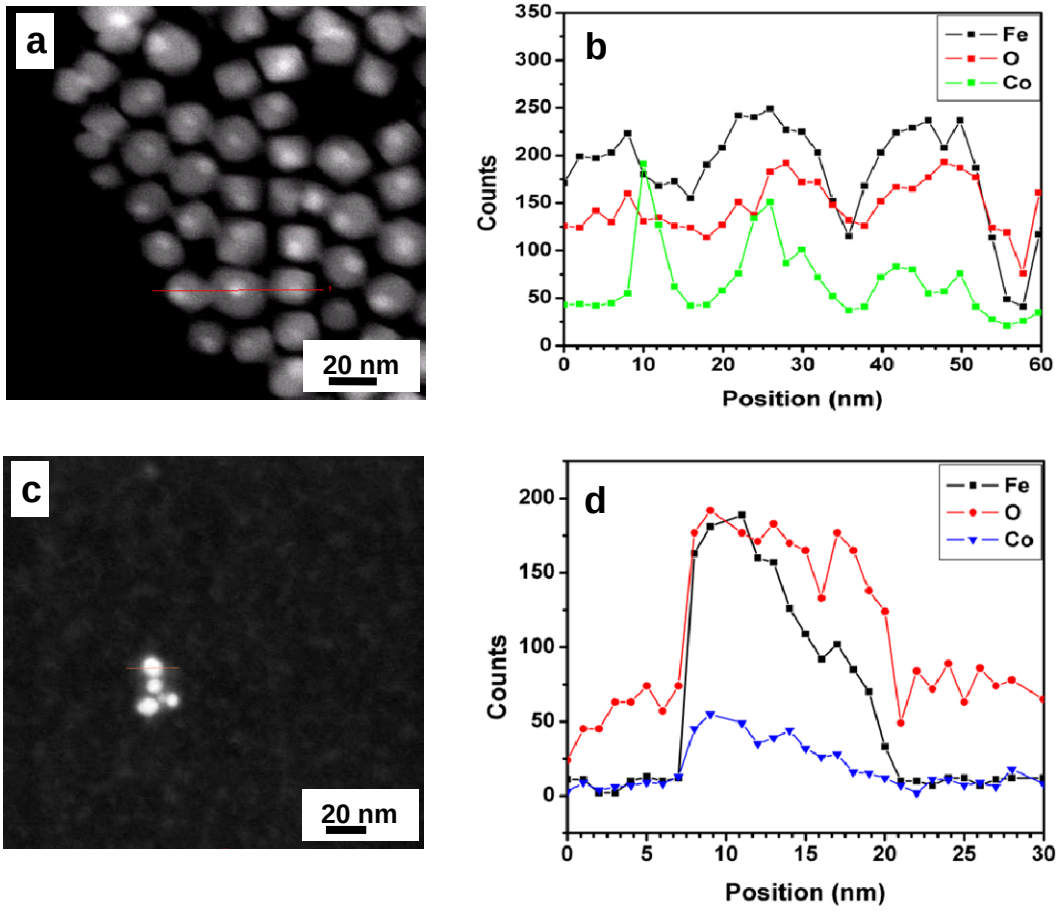

Figure 4.2. *STEM mode images and EDX line scan of $Co@Fe_2O_3$ heterodimer and ternary phase $CoFe_2O_4$ nanoparticles. (a) STEM mode image of $Co@Fe_2O_3$ heterodimer nanoparticles where cobalt shows a bright spot and also Fe_2O_3 shows a dark contrast (b) corresponding EDX line scan which confirms that bright spot cobalt and also confirms the presence of iron and oxygen for less bright nanoparticles. (c) STEM mode image of $CoFe_2O_4$ nanoparticles and (d) the corresponding line scan EDX which confirm that cobalt is distributed uniformly.*

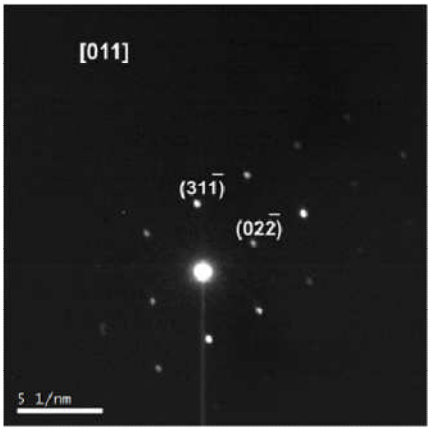

Figure 4.3. *Selected electron diffraction pattern of $CoFe_2O_4$ nanoparticle.*

It is worth mentioning that 15 minutes after the addition of $Fe(CO)_5$, Co@Fe_2O_3 heterodimers were almost formed (Figure 4.4a) and were stable even after heating for 1 hour at elevated temperature like 300ºC (Figure 4.4b). In case of $CoFe_2O_4$ nanoparticles, after heating for 1 hour at 245ºC, spherical nanoparticles with size ~7 nm were obtained but further heating to 300ºC improved the crystallinity of product (Figure 4.4c).

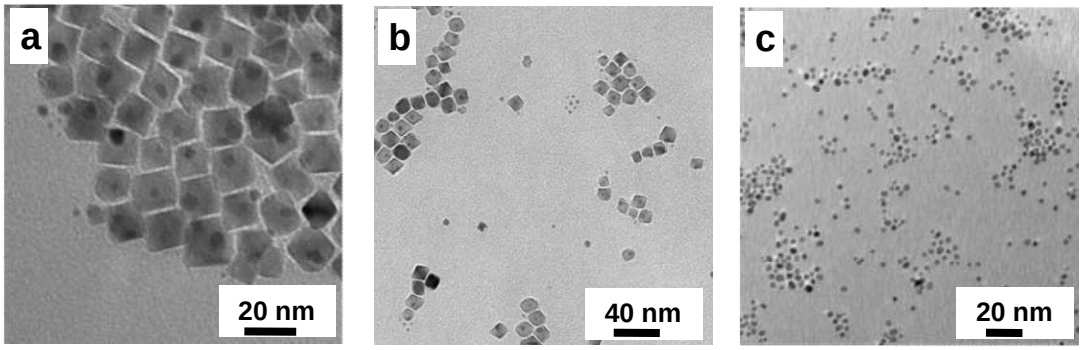

Figure 4.4. *Co@Fe_2O_3 nanoparticles after (a) 15 min,(b)1 h at 300°C and (c) $CoFe_2O_4$ nanoparticles after 1 h at 300°C.*

Representative XRD patterns of Co@Fe_2O_3 heterodimers and $CoFe_2O_4$ NPs are presented in Figure 4.5. According to the powder XRD patterns for Co@Fe_2O_3 (Figure 4.5a), the iron oxide domain consists of nanoparticular γ-Fe_2O_3 (Maghemite, PDF-2:39-1346) of approx.15 nm [14]. Rietveld refinements were performed according to the defect-spinel structure model of maghemite [15]. In order to distinguish between magnetite ($Fe_t^{II}Fe_o^{III}{}_2O_4$) and maghemite ($Fe_t^{III}Fe_o^{III}{}_{1.66}O_4$ = Fe_2O_3) the refinement was performed with 10^6 iterations, each starting

from random seeds of the site occupation factors of the metal cation sites (8*a* (t), 16*d* (o)) and the overall displacement factor held fix at B_{iso} = 1. The global minimum with Rwp = 0.04 and gof = 2.2 corresponds to a virtually full occupation of the 8*a* site (sof = 0.99(2)) and a significant cation-deficiency on the 16*d* site (sof = 0.82(2)), i.e. at composition of $Fe_{21.01}O_{32}$ = $Fe_{1.97}O_3$. X-ray diffraction data of $CoFe_2O_4$ were acquired in order to characterize phase purity of the final product. According to the x-ray powder diffraction patterns (Figure 4.5b) the sample consists of nanoparticular $CoFe_2O_4$ (PDF-2:22-1086) of approx. 7 nm [14]. Rietveld refinements with 10^6 iterations, each starting from random seeds of the site occupation factors of the metal cation sites of the spinel structure type, converge at Rwp = 0.047 and gof = 1.6 in an ordered structure model with all Co-atoms on the 8*c* position. Yet, due to the negligible difference in the atomic form factors of Co and Fe, the refined site occupations factors are not significant within the 3σ confidence interval.

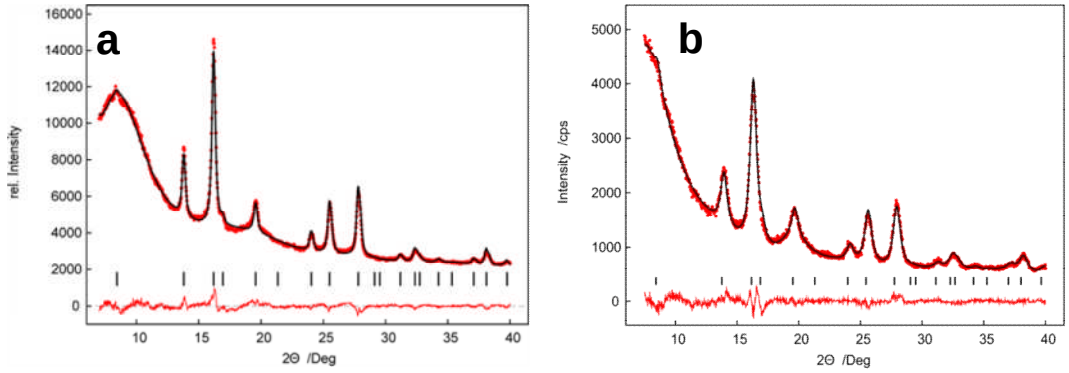

Figure 4.5. *(a) Rietveld plot of Co@Fe_2O_3 NPs (red dots: experimental pattern, black line: calculated pattern, red line: difference, black ticks: reflection positions, observed and calculated pattern are shifted for clarity). (b) Rietveld plot of $CoFe_2O_4$ NPs (red dots: experimental pattern, black line: calculated pattern, red line: difference, black ticks: reflection positions).*

The magnetic properties of the Co@Fe_2O_3 heterodimers and $CoFe_2O_4$ NPs were measured by SQUID magnetometry. Figure 4.6a shows magnetic hysteresis loops of the Co@Fe_2O_3 heterodimers (Ø of the Co domains ≈ 6-7 nm, Ø of the Fe_2O_3 domains ≈ 15-18 nm) recorded at 5 K and 300 K, the temperature dependence of the magnetization for the field cooled (FC) and zero field cooled (ZFC) of Co@Fe_2O_3 heterodimers under applied magnetic fields of 100 Oe are shown as inset. The saturation magnetization of the Co@Fe_2O_3 heterodimer NPs at room temperature was 32 emu/g. The magnetic hysteresis loops along with the temperature

dependence of the magnetization for the field cooled (FC) and zero field cooled (ZFC) (as inset) of $CoFe_2O_4$ NPs are given in Figure 4.6b. The data show ferromagnetic behavior of the $CoFe_2O_4$ NPs with a coercivity of NPs of 800 Oe and a saturation magnetization of 70.1 emu/g

.

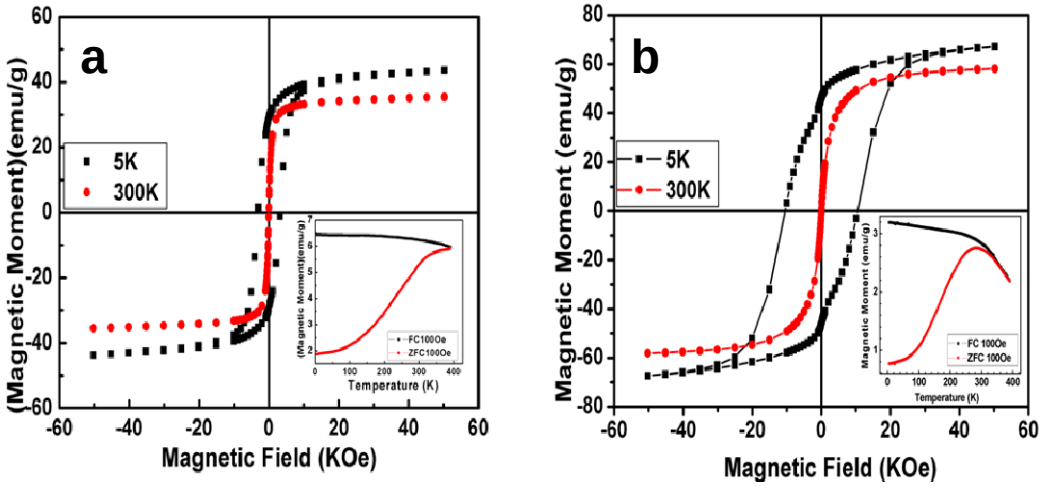

Figure 4.6. *Magnetic hysteresis loops at 5 K and 300 K and (a) Co@Fe_2O_3 heterodimers (b) $CoFe_2O_4$ NPs. Temperature dependence of the magnetization in field-cooling (FC) and zero-field-cooling (ZFC) mode are given in insets.*

The room temperature mössbauer spectrum of the ternary phase $CoFe_2O_4$ (Figure 4.7a) shows a typical spectrum due to the superparamagnetic relaxation effect of the NPs. At 110 K (Figure 4.7b) the spectrum consists of a doublet and a broad distribution magnetic sextet. The former one could be assigned to the superparamagnetic particles and the latter one corresponds to the particles below the blocking temperature. The broadening of the magnetic subspectrum results from the particles size distribution (6-7 nm range). The fit of the mössbauer spectrum using a distribution model at 110 K gives following values of hyperfine parameters for the magnetic subspectrum: isomer shifts IS = 0.4(1) mms^{-1}, hyperfine magnetic field H_{hf} = 510(3) kOe and almost zero value of the quadrupole splitting ΔE_Q. The values of hyperfine parameters correspond to Fe^{3+}. Thus, the mössbauer data are compatible with the presence of cobalt ferrite $(Co^{2+})(Fe_2^{3+})O_4$ [16]. Mössbauer spectroscopic measurements of Co@Fe_2O_3 nanoparticles at 80 K reveal a paramagnetic doublet and static magnetic sextet (Figure 4.7c). The paramagnetic subspectrum with a relative intensity of 13% with IS = 0.44(1) mms^{-1} and quadrupole splitting 0.86(2) mms^{-1} corresponds to superparamagnetic

relaxating particles of three-valence iron oxide. The phase assignment of this iron oxide follows from the values of the hyperfine parameters of the magnetic fraction of the mössbauer spectrum. The fit with a distribution model gives following average parameters: IS = 0.43(4) mms^{-1}, H_{hf} = 515(9) kOe, ΔE_Q = 0.0 mms^{-1}. The parameters are compatible with superparamagnetic particles of maghemite γ-Fe_2O_3 [16].

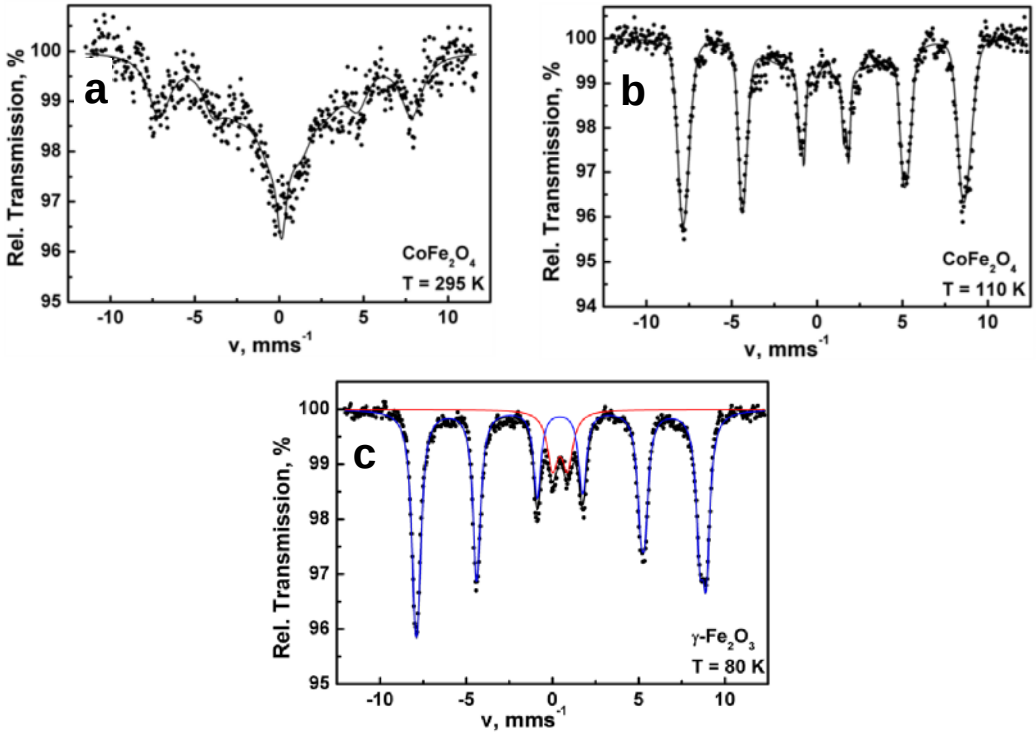

Figure 4.7. *^{57}Fe Mössbauer spectra of (a) $CoFe_2O_4$ NPs recorded at 295 K (b) at 110 K and (c) Co@Fe_2O_3 nanodimers recorded at 80 K.*

In heteroparticles, the close coupling of different components on the nanoscale may significantly improve the application performance or even create new properties: (i) multifunctionality, e.g. by a combination of magnetic and plasmonic NPs [8, 11], (ii) directed self-assembly, achieved by modifying different functional ligands on each surface [8c], (iii) efficient charge separation at the hetero-interface in a single NP [17]. The Co and Fe_2O_3 domains can be functionalized selectively. In order to explore potential applications, we functionalized the NPs with a multidentate [18] copolymer carrying catechol anchor groups and PEG-linkers ($M_r \approx 800$) with free amino groups for further surface conjugation (Figure 4.8a). The polymer functionalized NPs were stable for several days against aggregation and precipitation in various aqueous media including deionized water or PBS buffer solution (Figure 4.8b).

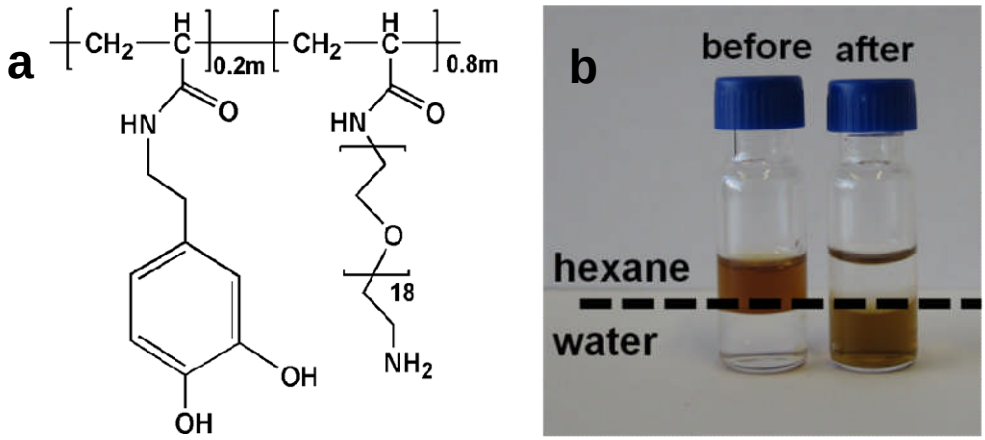

Figure 4.8. *(a) Scheme of polymeric ligand. (b) Digital photograph of Co@Fe_2O_3 solutions before (left) and after (right) surface functionalization in hexane (top layer) and in water (bottom layer).*

The magnetic resonance imaging (MRI) properties of solutions of polymer functionalized $CoFe_2O_4$ (Figure 4.9a) and Co@Fe_2O_3 (Figure 4.9b) NPs in water at different Fe concentrations (determined by AAS) were performed on a clinical 3.0 Tesla scanner (Magnetom Trio, Siemens Medical Solutions, Erlangen, Germany) by means of a T_1 and T_2 measurement using a centric reordered saturation recovery (SR) prepared snapshot fast low angle shot (SR-TurboFLASH) pulse sequence with different preparation times (T_I) ranging from 20 ms up to 8000 ms. Other pulse sequence parameters were as follows: repetition time (T_R) = 3.4 ms, echo time (T_E) = 1.5 ms, flip angle = 20°. Figure 5c and d show a T_1 and T_2-weighted MR image of three different concentrations of polymer functionalized $CoFe_2O_4$ and Co@Fe_2O_3 heterodimer NPs. The functionalized NPs were dissolved in saline solution (concentrations from 0.087 to 0.232 mM for $CoFe_2O_4$ and 0.003 to 0.014 mM for Co@Fe_3O_4 NPs). T_1 and T_2 measurements revealed T_1 and T_2 relaxivities of 232.14 and 413.22 $mM^{-1}ms^{-1}$ for the $CoFe_2O_4$, whereas Co@Fe_2O_3 showed a T_1 relaxivity of 32.69 and an exceptionally large T_2 relaxivity of 1804.46 $mM^{-1}ms^{-1}$, which is many folds higher than commercially available iron oxide based MRI agents [19].

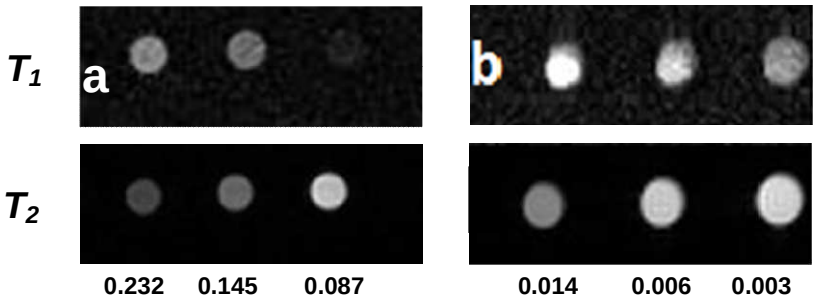

Figure 4.9. *(a & b) T_1 and T_2-weighted MRI images of solutions containing polymer functionalized $CoFe_2O_4$ and Co@Fe_2O_3 NPs (concentrations in mM).*

4.3. Summary and Outlook

Although cytotocxicity assays work for our nanoparticles is in progress, it is well reported that these nanoparticles can be used in living systems [20].

In conclusion, we report a facile method to synthesize phase separated Co@Fe_2O_3 heteroparticles or $CoFe_2O_4$ ternary phase by controlling the diffusion path in the nucleation step. Although the formation of $CoFe_2O_4$ ternary phase [21] is the most likely and it is well reported in the literature, herein we show for the first time the synthesis of Co@Fe_2O_3 heteroparticles.

4.4. Experimental Section

Methods and Material

Iron(0) pentacarbonyl ($Fe(CO)_5$, 99.5%, Acros), cobalt(II) acetate tetrahydrate ($Co(ac)_2.4H_2O$, 99%, Fluka), oleic acid (90%, Aldrich), oleylamine (90%, Acros), 1-octadecene (ODE, 90% Acros), di-tert-butyl dicarbonate ($(Boc)_2O$, >99%, Aldrich), dioxane (p.A. Fisher), H_2N-$PEG_{(800)}$-NH_2 (Aldrich), triethylamine (>99%, Aldrich), 3-hydroxy tyramine hydrochloride (Dopamine.HCl) (98%, Aldrich), trifluoroacetic acid (TFA) (99%, Aldrich), ethanol (99.8%, Roth), toluene (>99%, Aldrich), hexane (p.A. Fisher), dichloromethane DCM (p.A. Fisher), dimethylformamide (DMF) (extra dry, >99.8%, Acros) and diethyl ether (p.A. Fisher) were used as received without further purification.

Synthesis of Rhomboid Co@Fe_2O_3 Heterodimer Nanoparticles

1 mmol cobalt acetate $Co(ac)_2$, 3 mmol oleic acid, 3 mmol oleylamine and 10 mL octadecane were mixed for 20 min before heating under a constant flow of argon (Ar) and using mechanical stirrer. The solution was heated to 245ºC with a constant rate of 3ºC/min. After

reaching to this temperature, 2 mmol $Fe(CO)_5$ was added and the temperature was kept at this temperature for 30 minutes. The product was precipitated by addition of excess of ethanol and collected by centrifugation (9000 rpm, 10 min, RT). The nanoparticles were repeatedly washed by dissolving them in hexane, precipitating them with ethanol and centrifugation (9000 rpm, 10 min, RT). Finally, the product was dissolved in hexane.

Synthesis of Spherical $CoFe_2O_4$ Nanoparticles

1 mmol cobalt acetate $Co(ac)_2$, 3 mmol, oleic acid, 3 mmol oleylamine, 10 mL octadecane and 2 mmol $Fe(CO)_5$ were mixing together for 20 min under argon and with mechanical stirrer. The reaction mixture was heated to 245ºC (heating rate of 3ºC/min) for 1 hour and the resulting solution was washed and precipitated by ethanol. The product was characterized using TEM as shown in figure S4, which confirms the formation of spherical nanoparticles. However to improve the crystallinity of nanoparticles, after discarding the ethanol, the rest product was dissolved again in 5 mL octadecane, 1.5 mmol oleylamine and 1.5 mmol oleic acid and then heated again to 300ºC for another 1 hour. The second time heating improved the crystallinity of nanoparticles. The product was precipitated by addition of excess of ethanol and collected by centrifugation (9000 rpm, 10 min, RT). The nanoparticles were repeatedly washed by dissolving them in hexane, precipitating them with ethanol and centrifugation (9000 rpm, 10 min, RT). Finally, the product was dissolved in hexane.

Synthesis of Boc Protected Bis-Amine $PEG_{(800)}$ (NBoc-$PEG_{(800)}$-NH_2)

A solution of $(Boc)_2O$ (0.02 mol) in 30 mL of anhydrous dioxane was added drop wise to a solution of NH_2-$PEG_{(800)}$-NH_2 (0.1 mol) in 50 mL anhydrous dioxane. The resulting solution was stirred overnight at room temperature. The solvent was evaporated and the oily product obtained was dissolved in 50 mL of water and extracted thrice using 50 mL of CH_2Cl_2. The combined organic phases were washed with a conc. solution of NaCl and dried over anhydrous Na_2SO_4. The resulting organic phase was concentrated by rotary evaporation and viscous, colorless oil was obtained. Further purification was achieved by flash chromatography on silica using a CH_2Cl_2/ethanol mixture (2:1) as eluent.

Preparation of the Polymer

The poly (active ester) poly(pentafluorophenyl acrylate) (PFA) was prepared as reported earlier [22-25]. GPC analysis of the obtained polymer (THF, light scattering detection) gave the following values: M_n = 16,390 g/mol, with PDI = 1.39, with an average of 70 repeating units.

For the synthesis of the multifunctional poly(acrylamides), poly(active ester)

poly(pentafluorophenyl acrylate) (700 mg, 2.94 mmol repeating units) was dissolved in a mixture of 9 mL of dry DMF and 0.7 mL of triethylamine. After that, 3-hydroxytyramine hydrochloride (24 mg) dissolved in 3 mL DMF and 0.4 mL triethylamine was added and the reaction mixture was stirred for 3 hours at 50°C. In the final step the remaining active ester groups were substituted using an excess of NBoc-$PEG_{(800)}$-NH_2 (dissolved in 3 mL dry DMF) and stirring for 5 h at 50°C. The solution was concentrated to about 2 mL and the polymeric ligand was precipitated by addition of cold ethyl ether. The precipitated polymer was centrifuged (9000 rpm, 10 min and RT) and the solvent was decanted. Upon drying, 286 mg of colorless oil was obtained.

Cleavage of the Boc Group

The polymer obtained above was dissolved in CH_2Cl_2 (30 mL). After that, trifluoroacetic acid (2.0 mL) was added and the mixture was stirred at room temperature for 2 h. After that, the reaction solution was treated with mixture of water and hexane (30 mL/50 mL) and vigorously stirred for 30 minutes. The aqueous phase containing the polymer was separated and concentrated to 2 mL and dialysed against deionized water for 2 days at room temperature (cellulose membrane, MWCO = 3,500). Finally, the water was evaporated and the product was redissolved in $CHCl_3$ and to make a stock solution, which was kept at +4ºC.

Functionalization of $Co@Fe_2O_3$ and $CoFe_2O_4$ Nanoparticles

$Co@Fe_2O_3$ and $CoFe_2O_4$ nanoparticles (10 mg) were dispersed in 15 mL of $CHCl_3$ by slowly dropping over 1 h into the above synthesized polymeric ligand solution (20 mg/10 mL, chloroform). The reaction was continuously stirred overnight at room temperature, under inert conditions. The functionalized nanoparticles were precipitated by addition of hexane and separated from unbound polymer and surfactants by centrifugation. These nanoparticles were washed twice by dissolving them in chloroform and precipitating them with hexane. Finally, the particles were stored in or DMF at +4ºC.

Physical Characterization

Electron Microscopy

The size and morphology of the as synthesized $Co@Fe_2O_3$ and $CoFe_2O_4$ nanoparticles were investigated using transmission electron microscopy (TEM, Philips EM 420 instrument with an acceleration voltage of 120 kV). Samples for transmission electron microscopy were prepared by placing a drop of dilute nanoparticle solution in hexane on a carbon coated copper grid. Low-resolution TEM images were recorded on a Philips EM420 microscope operating at an acceleration voltage of 120 kV. High-resolution TEM data and ED patterns

were obtained on a FEI Tecnai F30 S-TWIN with a 300 kV field emission gun.

X-Ray Diffraction

X-ray diffraction patterns were recorded with a Bruker AXS D8 Advance diffractometer equipped with a SolX energy dispersive detector in reflection mode using unfiltered MoKα radiation. Samples were prepared between two layers of Scotch ® Magic tape. X-ray diffraction patterns were recorded in the range of $5 \leq 2\Theta$ /deg ≤ 40 at a step size of $\Delta 2\Theta = 0.025°$ and a step time of $\Delta t = 10.2$s. A set of six pattern was accumulated in order to gain an appropriate signal to noise ration. Crystalline phases were identified according to the PDF–2 database PDF2 using Bruker AXS EVA 10.0 software. Full profile pattern fitting according to Rietveld was performed with TOPAS Academic 4.1 applying the fundamental parameter approach [26]. The magnetic properties of powder samples were measured with a superconductive quantum interference device (SQUID, Quantum Design MPMS XL).

Mössbauer Spectroscopy and Superconducting Quantum Interference Device

Mössbauer spectra were obtained at room temperature 110 K and 80 K with a constant acceleration transmission mössbauer spectrometer and ^{57}Co (Rh) source. A α-Fe foil was used to calibrate the mössbauer spectrometer in a velocity range of ±12 mms^{-1}. Magnetic measurements were carried out using a Quantum Design MPMS-XL SQUID magnetometer.

Magnetic Resonance Imaging

MR signal enhancement effects were measured for the aqueous solutions of functionalized Co@Fe_2O_3 and $CoFe_2O_4$ nanoparticles at different Fe concentrations (measured with AAS) on a clinical 3.0 T MRI scanner (Magnetom Trio, Siemens Medical Solutions, Erlangen, Germany). Signal reception and radio frequency (RF) excitation was performed using 8-channel knee coil. For T_1-measurement, a saturation prepared (SR) snapshot fast low angle shot (SR-TurboFLASH) pulse sequence with repetition time (T_R) / echo time / flip angle = 3.0 ms/1.5 ms/20° was used with varying saturation times starting from 20 ms up to 8000 ms. For measuring the T_2 relaxation time, a multi-echo spin-echo pulse sequence (CPMG, Carr-Purcell-Meiboom-Gill) with a total of 32 echos and $T_R = 5000$ ms was used, the echo time was varied from 7 ms to 224 ms. In a second T_2 measurement T_E was varied from 15 ms up to 480 ms.

4.5. References

[1] J. D. Corbett, *Synthesis of Solid-State Materials*; Clarendon Press: Oxford, **1987**.

[2] C. Wang, H. Daimon and S. Sun, *Nano Lett*. **2009**, *9*, 1493.

[3] (a) H. Yu, M. Chen, P. M. Rice, S. X. Wang, R. L. White and S. Sun, *Nano Lett.* **2005**, *5*, 379. (b) Y. Wei, R. Klajn, A. O. Pinchuk and B. A. Grzybowski, *Small* **2008**, *4*, 1635.

[4] B. Nakhjavan, M. N. Tahir, F. Natalio, H. Gao, K. Schneider, T. Schladt, I. Ament, R. Branscheid, S. Weber, U. Kolb, C. Sönnichsen, L. M. Schreiber and W. Tremel, *J. Mater. Chem.* **2011**, *21*, 8605.

[5] G. Lopes, J. M. Vargas, S. K. Sharma, F. Beron, K. R. Pirota, M. Knobel, C. Rettori and R. D. Zysler, *J. Phys. Chem. C* **2010**, *114*, 10148.

[6] T. D. Schladt, M. I. Shukoor, M. N. Tahir, F. Natalio, K. Schneider, I. Ament, J. Becker, F. Jochum, S. Weber, P. Theato, L. M. Schreiber, C. Sönnichsen, H. C. Schröder, W. E. G. Müller and W. Tremel, *Angew. Chem. Int. Ed*. **2010**, *49*, 3976.

[7] Y. Jang, J. Chung, S. Kim, S. W. Jun, B. H. Kim, D. W. Lee, B. M. Kim and T. Hyeon, *Phys. Chem. Chem. Phys.* **2011**, *13*, 2512.

[8] B. Blackman, D. Battaglia and X. Peng, *Chem. Mater.* **2008**, *20*, 4847.

[9] (a) Y.-W. Jun, J.-S. Choi and J. Cheon, *Chem. Commun*. **2007**, *12*, 1203. (b) L. Carbone and P. D. Cozzoli, *Nano Today* **2010**, *5*, 449.

[10] M. Casavola, A. Falqui, M. A. Garcia, M. Garcia-Hernandez, C. Giannini, R. Cingolani and P. D. Cozzoli, *Nano Lett*. **2009**, *9*, 366.

[11] J. B. Goodenough, *Magnetism and the Chemical Bond*; Interscience: New York, **1963**.

[12] M. Green, *Chem. Commun*. **2005**, *24*, 3002.

[13] M. Noh and D. C. Johnson, *J. Am. Chem. Soc.* **1996**, *118*, 9117.

[14] R. W. Cheary and A. A. Coelho, *J. Appl. Crystallogr*. **1992**, *25*, 109.

[15] M. D. Marco, M. Port, P. Couvreur, C. Dubernet, P. Ballirano and C. Sadun, *J. Am. Chem. Soc.* **2006**, *128*, 10054.

[16] N. N. Greenwood and T. G. Gibb, *Mössbauer Spectroscopy*; Chapman and Hall Ltd: London, **1971**.

[17] L. Carbone, A. Jakab, Y. Khalavka and C. Sönnichsen, *Nano Lett.* **2009**, *9*, 3710.

[18] M. I. Shukoor, F. Natalio, N. Glube, M. N. Tahir, H. A. Therese, V. Ksenofontov, N. Metz, P. Theato, P. Langguth, J.-P. Boissel, H. C. Schröder, W. E. G. Müller and W. Tremel, *Angew. Chem. Int. Ed.* **2008**, *47*, 4748.

[19] (a) U. I. Tromsdorf, O. T. Bruns, S. C. Salmen, U. Beisiegel and H. Weller, *Nano Lett*. **2009**, *9*, 4434. (b) B. Basly, D. F. Flesch, P. Perriat, G. Pourroy and S. B. Colin, *Contrast Media Mol. Imaging* **2011**, *6*, 132.

[20] (a) S. Mohapatra, S. R. Rout, S. Maiti, T. K. Maiti and A. B. Panda, *J. Mater. Chem*. **2011**, *21*, 9185. (b) L. S. Bouchard, M. S. Anwar, G. L. Liu, B. Hann, Z. H. Xie, J. W. Gray, X. Wang, A. Pines and F. F. Chenc, *Proc. Natl. Acad. Sci.* **2009**, *106*, 4085.

[21] (a) R. T. Olsson, G. S. Alvarez, M. S. Hedenqvist, U. W. Gedde, F. Lindberg and S. J. Savage, *Chem. Mater*. **2005**, *17*, 5109. (b) K. S. Martirosyan, L. Chang, J. Rantschler, S. Khizroev, D. Luss and D. Litvinov, *IEEE Trans. Magn.* **2007**, *43*, 3118.

[22] I. Potavova, R. Mruk, S. Prehl, R. Zentel, T. Basche and A. Mews, *J. Am. Chem. Soc.* **2003**, *125*, 320.

[23] M. Eberhardt, R. Mruk, P. Theato and R. Zentel, *Eur. Polym. J.* **2005**, *41*, 1569.

[24] M. N. Tahir, M. Eberhardt, H. A. Therese, U. Kolb, P. Theato, W. E. G. Müller, H. C. Schröder and W. Tremel, *Angew. Chem. Int. Ed.* **2006**, *45*, 4803.

[25] M. N. Tahir, M. Eberhardt, P. Theato, S. Faiß, A. Janshoff, T. Gorelik, U. Kolb and W. Tremel, *Angew. Chem. Int. Ed.* **2006**, *45*, 908.

[26] R. W. Cheary and A. A. Coelho, *J. Appl. Crystallogr.* **1992**, *25*, 109.

5. Heterodimeric $Ni@Fe_2O_3$ Nanoparticles: Controlled Synthesis and Magnetically Recyclable Catalytic Application for Dehalogenation Reactions

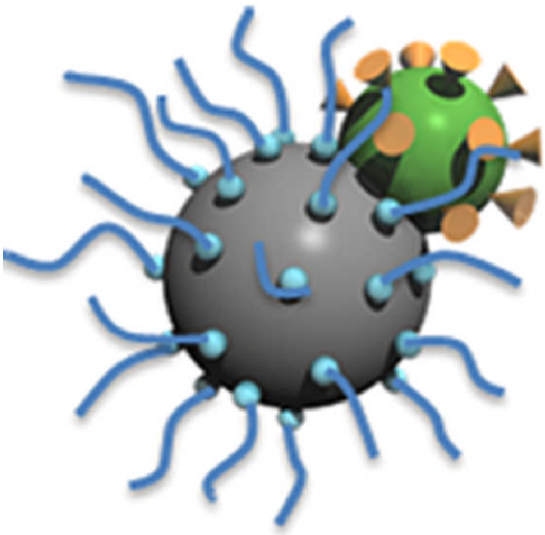

Bahar Nakhjavan[a], Muhammad Nawaz Tahir[a], Filipe Natalio[a], Martin Panthöfer[a], Haitao Gao[a], Rute Andre[a], Teuta Gasi[a], Vadim Ksenofontov[a], Robert Branscheid[b], Ute Kolb[b] and Wolfgang Tremel[a]

[a]*Institut für Anorganische Chemie und Analytische Chemie, Johannes Gutenberg-Universität, Duesbergweg 10-14, D-55099 Mainz, Germany. Fax: +49 6131 39-25605; Tel: +49 6131 39-25135; E-mail: tremel@uni-mainz.de*

[b]*Institut für Physikalische Chemie, Johannes Gutenberg-Universität, Welderweg 11, 55099 Mainz, Germany.*

In preparation

5.1. Introduction

The hybrid nanocrystals containing two or more domains of different materials within the same particle have attracted scientists and technologists because their multifunctional behavior paves the way to the foundation of bottom-up nanotechnologies [1]. The properties of such nanoparticles include the combined properties of the individual components with enhanced chemical reactivity [2]. Among them, heterodimeric nanocrystals composed of metals and semiconductor metal oxides became more popular due to their electronic and optical properties determined by the size of the particles and the extent of confinement ofvalence electrons [3, 4]. Heterodimer nanoparticles containing metal and metal oxide components with different compositions like Pt@Fe_3O_4 [5], Au@Fe_3O_4 [6], Ag@Fe_3O_4 [7] or Au@MnO [8] and with different shapes have been extensively investigated. The formation of these heterodimeric nanoparticles was chemically expected because the ternary phase diagrams of these metals do not contain a significant number of ternary oxide phases. Therefore, the synthesis of these heterodimeric nanoparticles by phase separation can be rationalized. However, unlike other metal and metal oxide heterodimeric nanoparticles, Ni@Fe_2O_3 has not been investigated and a similar synthesis were reported from labile complexes of Fe and Ni in the presence of oleic acid and oleylamine, respectively[9]. Although nickel is more difficult to be reduced compared to nobel metals, recent studies have shown that nickel nanoparticles can also be produced from the direct decomposition of nickel organometallic precursors in some alkylamines such as oleylamine [10] or dodecylamine [11]. Recently, we have focused on the synthesis of heterodimeric nanoparticles of metals like (M=Cu, Co) [12] whose ternary phases with the general formula MFe_2O_4 are well established [13].

As an extension of our work, here we report an one-pot wet chemical synthesis of dumbbell-like Ni@Fe_2O_3 heterodimeric nanocrystals (~5-6 nm for Ni domains and ~15-18 nm for Fe_2O_3 domain) through, the thermally controlled decomposition of metal acetate in surfactant mixture solution. Our synthetic approach relies on the fact that phases can be controlled, depending on their activation energies for nucleation as in nano-regime the diffusion barriers become less significant [14]. We found that the key step on this production of Ni@Fe_2O_3, resides on the formation of intermediate nickel nanoparticles obtained through *in situ* decomposition/reduction of an “organometallic” precursor. In contrast, a direct solid-state approach that relies on the reaction between the components would be limited by the

interdiffusion of the components. Consequently, high temperatures and long reaction times are usually necessary for reactions between bulk components/elements as a result of the high activation energies of diffusion in the solid state.

5.2. Results and Discussion

In the past, it has been reported that Ni(0) complexes were effective catalysts for dehalogenation reactions, i.e., used for performing hydrogenolysis in cooperation with hydrides [15]. In recent years, also Ni nanoparticles either pure or in the alloy form have been used for the remediation of contaminants containing halogens or transfer hydrogenation of carbonyl compounds [16]. However, the applications were restricted due to solubility issues, i.e., only in few solvents these catalysts could be used. The heterodimeric nanoparticles provide two distinct surfaces which can be functionalized specifically which makes the heterodimer nanoparticles multifunctional.

Here in case of Ni@Fe_2O_3 heterodimeric nanoparticles, we explored how Ni domain can be used to deactivate and remove environmental hazardous halogenated pollutants. Moreover, the iron oxide (Fe_2O_3) domain plays a dual role (i) can be specifically functionalized to achieve better solubility in different solvents (most important for environmental purposes is water in which can become soluble), (ii) can be used for magnetic separation of the pollutant from the environment. A mechanism is also proposed where dehalogenation takes place, releasing bromide and the binding of the aromatic backbone to the Ni domains allowing a complete detoxicification of the environment. The synthesis of dumbbell-like Ni@Fe_2O_3 heterodimeric nanoparticles with nickel (Ni) domain (~5-6 nm) and Fe_2O_3 (~15-18 nm) is illustrated in Scheme 5.1. Ni nanoparticle intermediates were nucleated *in situ* by decomposition/reduction of nickel acetate precursor in the presence of oleylamine, oleic acid and trioctylphosphine at temperatures around 130°C and grown by increasing the temperature to 255°C. The Ni nanoparticles are monodisperse with an uniform size of approximately 5 nm as observed by transmission electron microscopy (TEM) image (Figure 5.1a). This can be visually monitored from the color change (green to dark brown). In a step further, Fe_2O_3 domain was nucleated and grown by subsequent injection of iron pentacarbonyl precursor ($Fe(CO)_5$) at 130°C for 30 minutes.

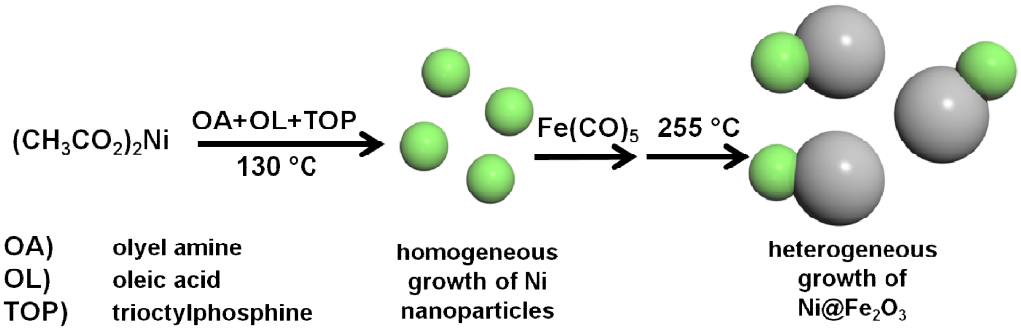

Scheme 5.1. *Synthetic procedure for dumbbell-like Ni@Fe_2O_3 nanoparticles.*

A representative TEM image of the heterodimeric dumbbell-like Ni@Fe_2O_3 nanoparticles is shown in Figure 5.1b. The Ni domain appears with a darker contrast as compared with the Fe_2O_3 domain due to higher electron density. STEM mode image and EDX line scan analysis of Ni@Fe_2O_3 heterodimeric nanoparticles are shown in Figure 5.1(c&d). Taking it together, the brighter and darker areas can be spatially assigned to a Ni and Fe_2O_3 domains confirming the composition of heterodimeric nanoparticles to be Ni@Fe_2O_3 nanostructured material.

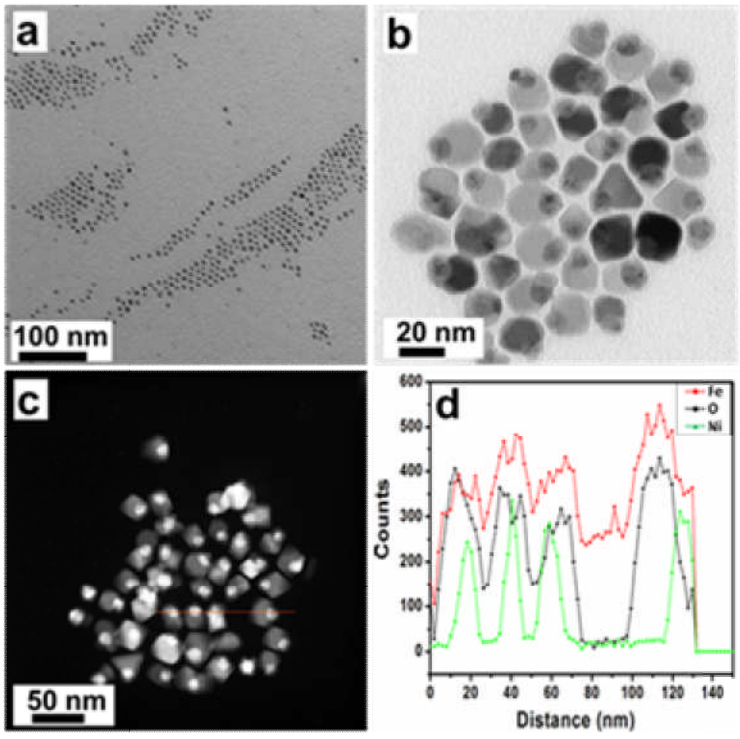

Figure 5.1. *Transmission electron microscopy (TEM) images: (a) nickel and (b) Ni@Fe_2O_3 heterodimer nanoparticles. (c) STEM mode image of Ni@Fe_2O_3 heterodimer nanoparticles where nickel shows a bright spot and also Fe_2O_3 shows a dark contrast (d) corresponding EDX line scan which confirms the presence of nickel, iron and oxygen.*

X-ray powder diffraction patterns recorded from bulk amounts of particles exhibit exclusively Ni and γ-Fe_2O_3 as crystalline phases in approx. amounts of 22(3)%wt. and 78(3)%wt., respectively [17]. The crystallite sizes of 14(1) nm and 3(1) nm match well to the particles' sizes determined from the TEM micrographs. Thus, the constituents of the Ni@Fe_2O_3 heterodimer nanoparticles are nano-single-crystals. The composition of the maghemite domains is Fe_xO with x = 0.609(14), which is slightly too small but, within the limit of error, in accordance with γ-Fe_2O_3 (Figure 5.2).

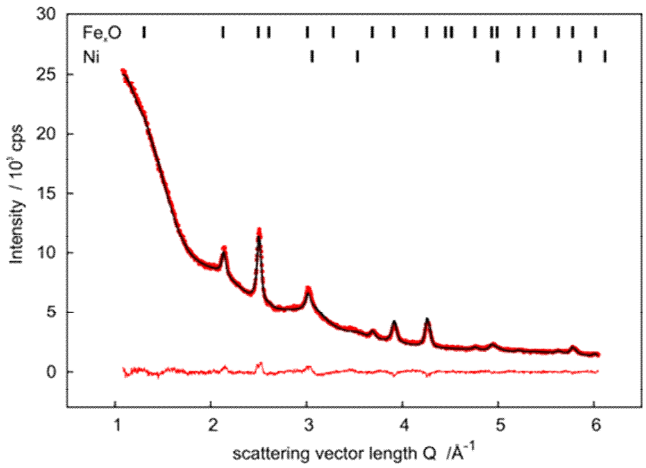

Figure 5.2. *XRD diffraction pattern of a bulk sample of Ni@Fe_2O_3 heterodimer nanoparticle (red dots: observed, black line: calculated, red line: difference, black ticks mark the reflection positions of the constituent phases).*

The magnetic properties of the heterodimeric Ni@Fe_2O_3 nanoparticles studied by measuring the temperature dependent magnetization and hysteresis curves with the superconducting quantum interference device (SQUID) are shown in Figure 5.3. For heterodimeric Ni@Fe_2O_3 nanoparticles, the saturation magnetization at room temperature is 53 emu/g with a coercivity of near zero Oe (Figure 5.3a). They exhibit ferrimagnetic properties at 5 K and superparamagnetic at room temperature. The ZFC magnetization monotonically increases with increasing temperature and the FC magnetization almost does not change. The splitting ZFC and FC curves reach a crossing point around 400 K, indicating a blocking temperature above room temperature (Figure 5.3b).

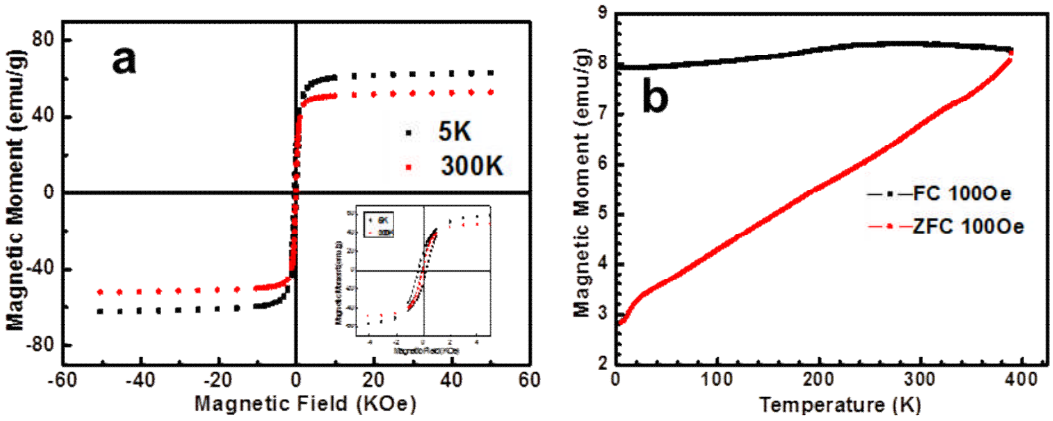

Figure 5.3. *(a) Magnetic hysteresis loops at 5 K and 300 K. (b) Temperature dependence of the magnetization in field-cooling (FC) and zero-field-cooling (ZFC) for $Ni@Fe_2O_3$ nanoparticles.*

Mössbauer spectra were obtained at 300K, 150K, 87 K and 4.2 K with a constant acceleration spectrometer and ^{57}Co (Rh) source. α-Fe foil was used to calibrate the Mössbauer spectrometer in a velocity range of ±10mm/s. The Mössbauer spectrum at 300K (Figure 5.4) shows a distribution of magnetic sextets which can be explained by the particle size distribution, while the Measurement at 150K beside the distribution of magnetic sextets shows one weak doublet (7%), which occurs due to the superparamagnetic relaxation effect of nanometer-size of nanoparticles. The Measurement at 150K, which is the temperature above the Verwey transition, was done, to distinguish magnetite from maghemite phases.

The Mössbauer spectrum of $Ni@Fe_2O_3$ at 87 K (Figure 5.4) shows superposition of magnetic sextetts together with a paramagnetic doublet which corresponds to the superparamagnetic relaxation of nanoparticles with size smaller than 6 nm. At 4.2 K the spectrum consists mainly of two groups of sextetts. The most intensive part (ca. 76%) with isomer shift IS = 0.4(1) mms^{-1} corresonds to maghemite with hyperfine magnetic field distribution in the range between 518 kOe and 525 kOe [18]. A broad magnetic subspectrum with an average hyperfine magnetic field of 463 kOe and IS = 0.78(2) mms^{-1} originates from iron oxide doped with Ni atoms. It could be attributed to the interface region between the pure maghemite phase in the Ni substrate.

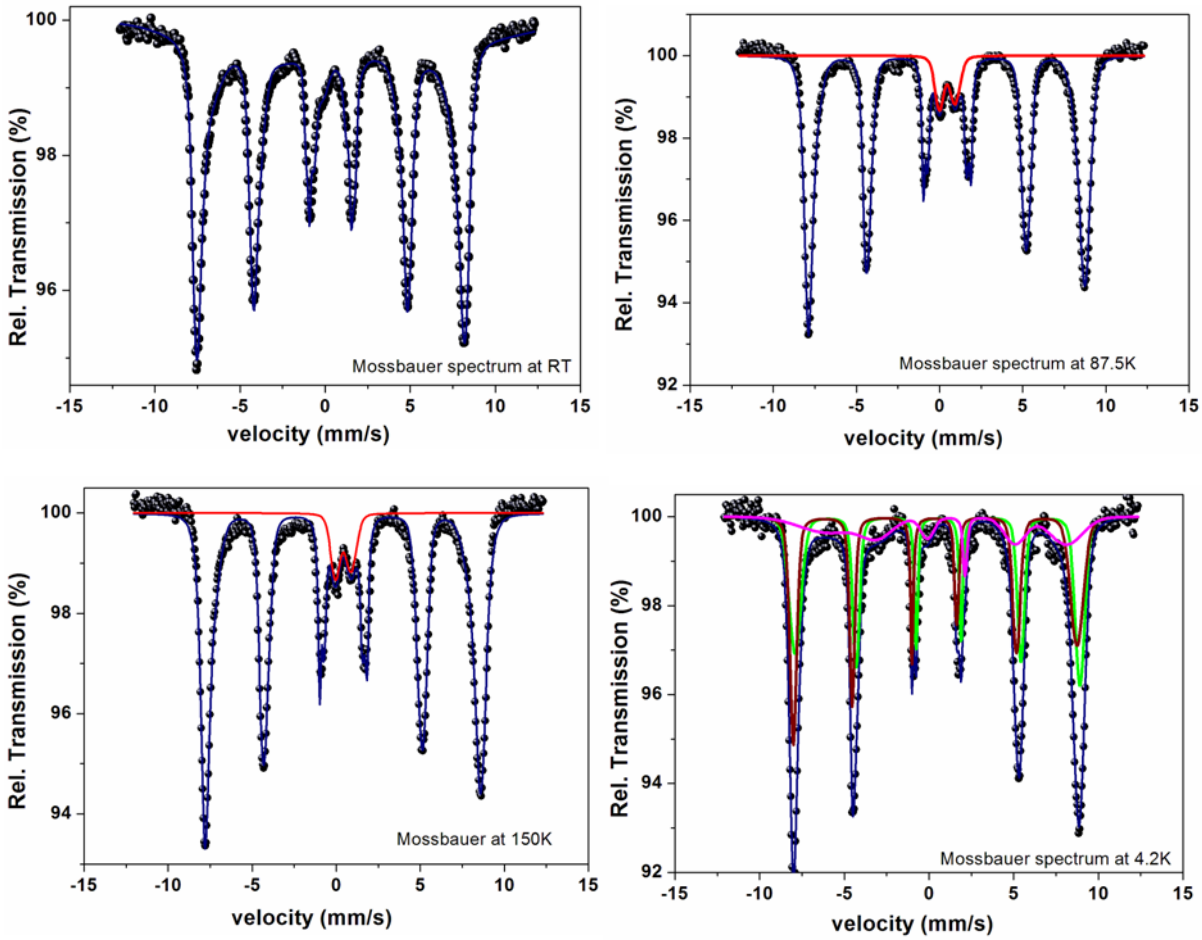

Figure 5.4. *^{57}Fe Mössbauer spectra of Ni@Fe_2O_3 nanoparticles at room temperature, 150K, 87.5K, and 4.2K.*

In order to explore the possible applications of Ni@Fe_2O_3 heterodimeric nanoparticles, the Fe_2O_3 domain was specifically polymer functionalized. For this purpose, the surfactant molecules were replaced by a multidentate polymeric ligand [19] containing catechol anchor groups and PEG (Mr ≈ 800) that carries with free amino groups for further surface conjugation (Figure 5.5) consequently improving nanoparticles solubility in various solvents including water. Figure 5a shows that upon polymer functionalization, Ni@Fe_2O_3 heterodimeric nanoparticles can be tranfered from an organic solvent to water. Upon polymer functionalization, these nanoparticles are stable against aggregation and precipitation especially in aqueous solutions for a couple of weeks.

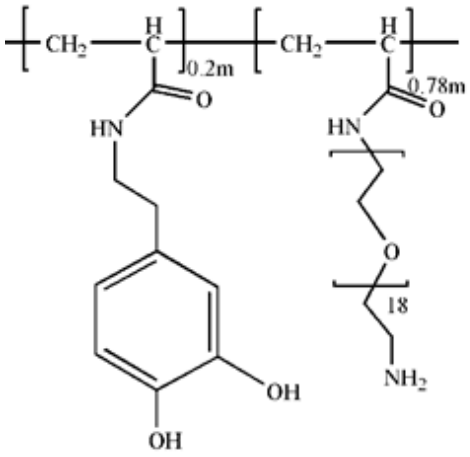

Figure 5.5. *Schematic representation of multifunctional copolymer containing 3-hydroxytyramine (dopamine) as an anchor group and PEG chains containing amine group.*

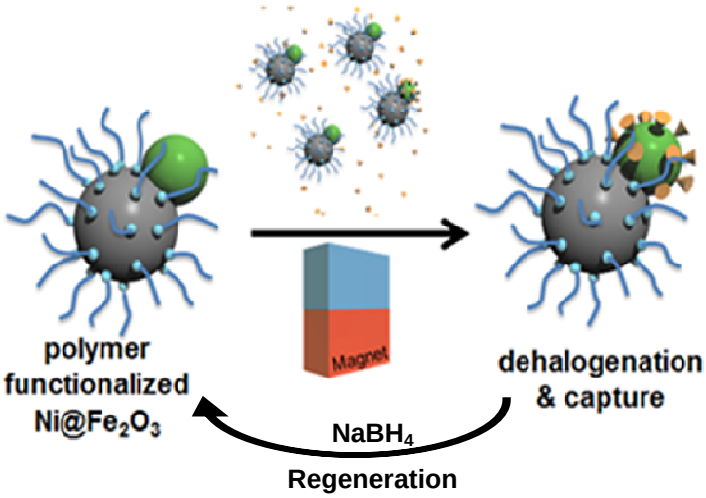

Scheme 5.2. *Schematic representation of catalytic applicability of the heterodimeric $Ni@Fe_2O_3$ nanoparticles. The Fe_2O_3 domain (grey sphere) was functionalized with a multidentade polymeric ligand (blue dots and blue wires) to enhance its water solubility while the Ni domain (green sphere) is free for catalysis. The Ni domain (Ni is in 0 oxidation state) was used for dehalogenation reactions (orange cones are representative of model halogenated compound) and capture of the compound whereas the Fe_2O_3 domain can be used for catalyst retrieval. The catalysts can be regenerated and the dehalogenated molecule by addition of sodium borohydride ($NaBH_4$).*

The advantage to use heterodimeric $Ni@Fe_2O_3$ nanoparticles for "semi-heteregenous" catalysis is that these nanoparticles could be well dispersed in many solvents including water

due to the polymer specific functionalization of the metal oxide domain (Figure 5.6a). Moreover, the heterodimeric character of these nanoparticles allows multifunctional "semi-heteregenous" catalysts concept within the same nanosized structure as the sketch in Scheme 5.2, i.e., *(i)* specific catalytic domain [Ni(0)] and *(ii)* the magnetic domain (Fe_2O_3) for retrieving the catalyst from the reaction after the catalysis has accomplished (Figure 5.6b). The catalytic activity of heterodimeric Ni@Fe_2O_3 nanoparticles was accessed to target only the Ni(0)domain of the NP under an aqueous environment, i.e., the focus was done on dehalogenation reactions mediated by Ni(0) as reported previously for inorganic Ni(0) complexes [20]. There is a high demand for effective dehalogenation reactions in order to eliminate unreactive halogenated aromatic compounds (e.g. polychlorinated biphenyls are persistent environmental poisons) from the environment [21] and replace the widely adopted strategy of pollutant incineration which is not a long term sustainable solution. Important to note that all the processes described so far include only chlorine removal and the consequent release of the regeneration of the catalyst by the use of sodium borohydride ($NaBH_4$) which is also toxic [22].

For this purpose, freshly prepared polymer functionalized heterodimeric Ni@Fe_2O_3 nanoparticles were incubated with a four-bromine containing model compound (e.g. bromophenol blue). The water solubility and the color of this model compound make it suitable for studying the dehalogenation reaction using heterodimeric Ni@Fe_2O_3 nanoparticles under an aqueous environment. Heterodimeric Ni@Fe_2O_3 nanoparticles (0.02mg/mL) were mixed with bromophenol blue solution (4.6 μM) and left for 6h at room temperature with gentle shaking to maximize the reaction. The solution lost the blue initial coloration (to transparent) (Figure 5.6c inset) as observed by naked eye after 6h (Figure 5c inset). To address the question whether the decoloration reaction was mediated by the Ni(0) or another specific interaction/reaction, a set of control experiments were carried out. Ni (5 nm) and Fe_2O_3 nanoparticles (10 nm) were independently mixed with bromophenol blue solution (4.6 μM) and left to react under the above described experimental conditions. Ni nanoparticles induced decoloration of the initial blue solution whereas the Fe_2O_3 nanoparticles did not, suggesting that the decoloration transformation is really due to the Ni domain of the heterodimeric Ni@Fe_2O_3 nanoparticles (Figure 5.7a and b). The study of ligand-metal interactions in the chemisorption of molecules on metal surfaces that are known to perform catalysis, either homogeneously or heterogeneously, as always been a subject of intense study [23] whether to enhance or reduce the activity of the catalyst, normally the first option was

desirable. Ni, specially Ni(0) is noted for the *d*-orbital filling and thus is able to strongly interact with ligands such as phosphorous groups [24] Taking this electronic interaction into account, another set of control experiment was performed in order to confirm the above statement. In a step further, heterodimeric Ni@Fe_2O_3 nanoparticles (0.02mg/mL) were mixed with a phosphate-containing solution (pH 7.2) for 30 min at room temperature. The nanoparticles were washed by making used of their magnetic properties and resuspended in distilled water to obtain the initial concentration. Afterwards, the nanoparticles were mixed with bromophenol blue solution (4.6 μM) and left for 6 h at room temperature. The solution remained with the same blue coloration as the initial solution confirming that the reaction occurs indeed in the Ni domain of the nanoparticles (Figure 5.7c).

The reaction between the heterodimeric Ni@Fe_2O_3 nanoparticles (0.02 mg/mL) and bromophenol blue (4.6 μM) was followed by UV-Vis spectrophotometry for 6h at room temperature (Figure 5.6c). The initial bromophenol blue solution (4.6 μM) shows a blue coloration with maximum wavelength at 590 nm. After 1 h of reaction, the 590 nm band decreases to approximately 20% of the original value and down to *ca.* 50% after 6h of reaction as earlier observed by naked eye experiments confirming that a transformation of the initial bromophenol blue solution occurs in the presence of the nanoparticles. The transformation was further explored by means of mass spectrometry. To the resulting solution, the nanoparticles were magnetically retrieved and the supernatant analyzed by mass spectrometry (MALDI-TOF). The MALDI spectral data showed the absence of bromophenol blue peaks confirming the data obtained earlier by UV-Vis and presence of dehalogenated compounds complexated to Ni. Since it has been reported that Ni based catalyst can be regenerated by treatment with sodium borohydride ($NaBH_4$), the regeneration of heterodimeric Ni@Fe_2O_3 nanoparticles was carried out after the reaction has been accomplished. Mass spectrometry analysis of the resulting solution shows the mass peaks corresponding to completely dehalogenated compound completing the catalytic cycle as depicted in Scheme 5.2.

Additional to the possibility to have a multifunctional “semi-heterogenous” catalyst, the reutilization of the same catalyst was also an issue that was addressed. Reutilization assays were performed by adding bromophenol blue solution (4.6 μM) to the heterodimeric Ni@Fe_2O_3 nanoparticles (0.02 mg/mL) and left to incubate for 1h at room temperature. The absorbance was recorded at 590 nm. Then, the catalyst was retrieved and the procedure repeated for 7 consecutive cycles as shown in Figure 5.6d. A tendency to increase the

absorbance at 590 nm is clearly observed. At the 7th cycle an increase of the absorbance of 30% suggests that the catalyst is losing its ability to mediate bromophenol blue dehalogenation.

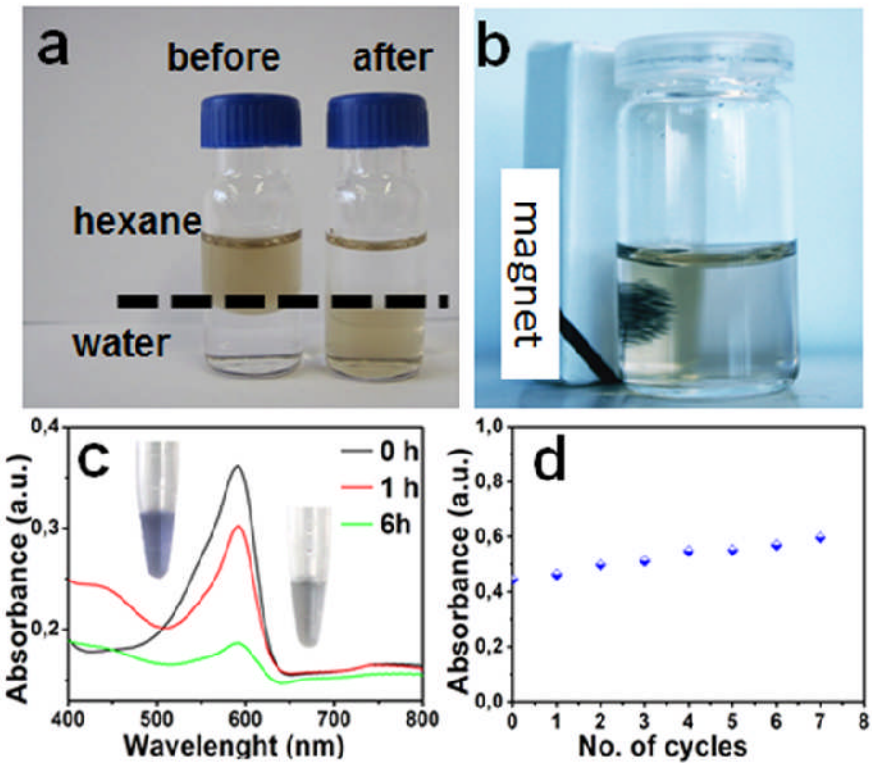

Figure 5.6. *(a) Digital photograph of Ni@Fe_2O_3 solutions before (left) and after (right) ligand exchange in hexane (top layer) and in water (bottom layer). (b) Digital image of the magnetic properties of Ni@Fe_2O_3 NPs. (c) Time course UV-Vis scans of the transformation of the bromophenol blue (4.6 μM) in the presence Ni@Fe_2O_3 NPs (0.02 mg/mL). The reaction was measured for 6h at room temperature. A decrease of the band at 590 nm is clearly observed to be time dependent. Upper inset: digital image of reaction vial where initial blue coloration typical from bromophenol blue is observed at time 0. Lower inset: digital image of reaction vial where loss of coloration occurs after 6h of reaction. (d) Catalyst reutilization capacity was accessed through consecutive cycles (7 in total). The supernatant was retrieved and the absorbance measured at 590nm. An increase of absorbance is clearly observed.*

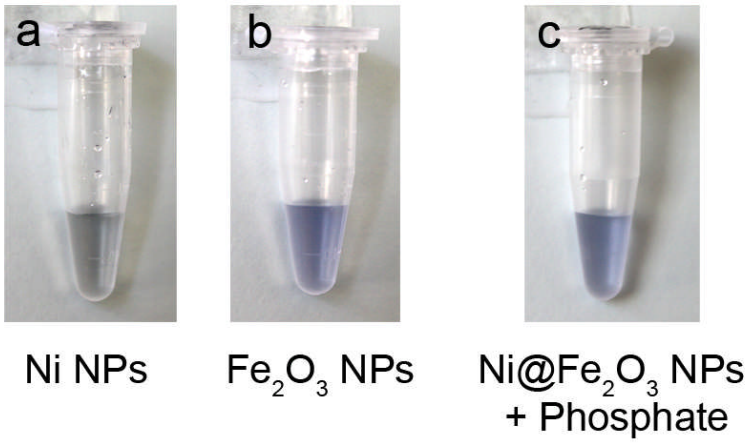

Figure 5.7. *Control experiments. Ni (5 nm) and Fe_2O_3 NPs (10 nm) were independently mixed with bromophenol blue solution (4.6 μM) and left to react for 6h at room temperature. (a) Ni NPs induced decoloration of the initial blue solution. (b) Fe_2O_3 NPs did not suggesting that the decoloration transformation is really due to the Ni part of the Ni@Fe_2O_3 NPs.(c) Ni@Fe_2O_3 NPs (0.02mg/mL) were mixed with a phosphate-containing solution (pH 7.2) for 30 min at room temperature. The nanoparticles were washed by making used of their magnetic properties and resuspended in distilled water to obtain the initial concentration. Afterwards, the nanoparticles were mixed with bromophenol blue solution (4.6 μM) and left for 6 h at room temperature. The solution remained with the same blue coloration.*

According to MALDI-TOF and UV-Vis data (kinetics and reutilizations assays), a possible mechanism for bromophenol blue dehalogenation catalysed by heterodimeric Ni@Fe_2O_3 nanoparticles is proposed. The exposed Ni(0) surface, in the presence of bromophenol blue, forms a π-complex with the aromatic rings transferring an electron leading to the formation of a radical anion and cage pair that will undergo another one-electron transfer. The halogen will be released to the solution and the bromophenol blue will be bonded to the Ni(0) surface. This is clearly observed in the reutilization assays where the "active sites" seem to be blocked as the number of cycles increases. However, these nanoparticles can be used up to 20 times until reaching 100% saturation, releasing innocuous bromide to the solution and efficiently capturing environmental toxic aromatic compounds.

5.3. Summary and Outlook

Multifunctional magnetic nanoparticles are important emerging platforms various applications. Novel phase separated Ni@Fe_2O_3 heterodimeric nanoparticles synthesized here can be used as a semi-heterogeneous catalyst to deactivate and remove environmental hazardous halogenated pollutants. This procedure is proposed where dehalogenation takes place. Therefore, the released bromide and the binding of the aromatic backbone to the Ni domains allow a complete detoxicification of the environment.

5.4. Experimental Section

Methods and Material

Iron(0) pentacarbonyl ($Fe(CO)_5$, 99.5%, Acros), nickel(II) acetate tetrahydrate ($Ni(ac)_2.4H_2O$, 99%, Fluka), oleic acid (90%, Aldrich), oleylamine (90%, Acros), trioctylphosphine ($[CH_3(CH_2)_7]_3P$, 90% Sigma-Aldrich), dioctyl ether (99%, sigma aldrich), tri n-octylamine (98%, Acros), di-tert-butyl dicarbonate ($(Boc)_2O$, >99%, Aldrich), dioxane (p.A. Fisher), H_2N-$PEG_{(800)}$-NH_2 (Aldrich), triethylamine (>99%, Aldrich), 3-hydroxy tyramine hydrochloride (Dopamine.HCl) (98%, Aldrich), trifluoroacetic acid (TFA) (99%, Aldrich), ethanol (99.8%, Roth), toluene (>99%, Aldrich), hexane (p.A. Fisher), dichloromethane DCM (p.A. Fisher), dimethylformamide (DMF) (extra dry, >99.8%, Acros), diethyl ether (p.A. Fisher) were used as received without further purification.

Synthesis of Monodisperse Nickel Nanoparticles

Nickel nanoparticles were synthesized by using 1 mmol nickel(II) acetate, $Ni(ac)_2$, 7 ml oleylamine, 1 mmol trioctylphosphine and 2 mmol oleic acid. They were mixed and stirred for 20 min under the inert condition before increasing the temperature. The mixture was heated to 240ºC for 30 min, and then slowly cooled to room temperature. A black product was precipitated from the solution by adding excessive ethanol, and separated by centrifugation (9000 rpm, 10 min, RT). Finally, the product was dissolved in toluene, flushed with argon (Ar) and stored at +4ºC.

Synthesis of Fe_2O_3 Nanoparticles

Fe_2O_3 nanoparticles were synthesized by using 150 mg iron(III) acetylacetonate, $Fe(acac)_3$, was mixed in dioctyl ether (10 mL) with oleic acid (0.06 mL) and oleylamine (0.18 mL) under argon. Under mechanical stirring, the reaction mixture was heated to 250 °C for 1 hour. A black product was precipitated from the solution by adding excessive ethanol, and

separated by centrifugation (9000 rpm, 10 min, RT). Finally, the product was dissolved in toluene and stored at +4ºC.

Synthesis of Ni@Fe_2O_3 Heterodimer Nanoparticles

The synthesis of Ni@Fe_2O_3 heterodimer nanoparticles was achieved by using 1 mmol nickel acetate $Ni(ac)_2$, 7 ml oleylamine, 1 mmol trioctylphosphine and 2 mmol oleic acid. They were mixed and stirred for 20 min under the inert condition before increasing the temperature. The mixture was heated to 130ºC for 20 min and then 2 mmol $Fe(CO)_5$ was added. After that, the solution rapidly heated to 255ºC for 30 min and then slowly cooled to room temperature. A black product was precipitated from the solution by adding excessive ethanol and separated by centrifugation (9000 rpm, 10 min, RT). Finally, the product was dissolved in toluene, flushed with argon (Ar) and stored at +4ºC.

Synthesis of Boc Protected Bis-Amine $PEG_{(800)}$ (NBoc-$PEG_{(800)}$-NH_2)

A solution of $(Boc)_2O$ (0.02 mol) in 30 mL of anhydrous dioxane was added drop wise to a solution of NH_2-$PEG_{(800)}$-NH_2 (0.1 mol) in 50 mL anhydrous dioxane. The resulting solution was stirred overnight at room temperature. The solvent was evaporated and the oily product obtained was dissolved in 50 mL of water and extracted thrice using 50 mL of CH_2Cl_2. The combined organic phases were washed with a conc. solution of NaCl and dried over anhydrous Na_2SO_4. The resulting organic phase was concentrated by rotary evaporation and viscous, colorless oil was obtained. Further purification was achieved by flash chromatography on silica using a CH_2Cl_2/ethanol mixture (2:1) as eluent.

Preparation of the Polymer

The poly (active ester) poly(pentafluorophenyl acrylate) (PFA) was prepared as reported earlier [25]. GPC analysis of the obtained polymer (THF, light scattering detection) gave the following values: M_n = 16,390 g/mol, with PDI = 1.39, with an average of 70 repeating units.

For the synthesis of the multifunctional poly(acrylamides), poly(active ester) poly(pentafluorophenyl acrylate) (700 mg, 2.94 mmol repeating units) was dissolved in a mixture of 9 mL of dry DMF and 0.7 ml of triethylamine. After that 3-hydroxytyramine hydrochloride (24 mg) dissolved in 3 mL DMF and 0.4 ml triethylamine was added and the reaction mixture was stirred for 3 hours at 50°C. In the final step the remaining active ester groups were substituted using an excess of NBoc-$PEG_{(800)}$-NH_2 (dissolved in 3 mL dry DMF) and stirring for 5 h at 50°C. The solution was concentrated to about 2 mL and the polymeric ligand was precipitated by the addition of cold ethyl ether. The precipitated polymer was centrifuged (9000 rpm, 10 min and RT) and the solvent was decanted. Upon drying, 286 mg

of colorless oil was obtained.

Cleavage of the Boc Group

The polymer obtained above was dissolved in CH_2Cl_2 (30 mL). After that trifluoroacetic acid (2.0 mL) was added and the mixture was stirred at room temperature for 2 h. After that the reaction solution was treated with the mixture of water and hexane (30 mL/50 mL) and vigorously stirred for 30 minutes. The aqueous phase containing the polymer was separated and concentrated to 2 mL and dialysed against deionized water for 2 days at room temperature (cellulose membrane, MWCO = 3,500). Finally, the water was evaporated and the product was redissolved in $CHCl_3$ and to make a stock solution which was kept at +4ºC.

Functionalization of Heterodimer Ni@Fe_2O_3 Nanoparticles

Ni@Fe_2O_3 nanoparticles (10 mg) were dispersed in 15 ml of $CHCl_3$ by slowly dropping over 1 h into the above synthesized polymeric ligand solution (20 mg/10 mL, chloroform). The reaction was continuously stirred overnight at room temperature, under inert conditions. The functionalized nanoparticles were precipitated by addition of hexane and separated from unbound polymer and surfactants by centrifugation. These nanoparticles were washed twice by dissolving them in chloroform and precipitating them with hexane. Finally, the particles were stored in or DMF at +4ºC.

Physical Characterization

Electron Microscopy

The size and morphology of the as synthesized Ni@Fe_2O_3 nanoparticles were investigated using transmission electron microscopy (TEM, Philips EM 420 instrument with an acceleration voltage of 120 kV). Samples for transmission electron microscopy were prepared by placing a drop of dilute nanoparticle solution in hexane on a carbon coated copper grid. Low-resolution TEM images were recorded on a Philips EM420 microscope operating at an acceleration voltage of 120 kV. High-resolution TEM data and ED patterns were obtained on a FEI Tecnai F30 S-TWIN with a 300 kV field emission gun.

X-Ray Diffraction

XRD measurements were performed on a Bruker D8 Advance diffractometer equipped with a Sol-X energy-dispersive detector and operating with Mo Kα radiation. Crystalline phases were identified according to the PDF-2 database, using Bruker AXS EVA 10.0 software. Full profile fits on the basis of the crystal structural models [26, 27] were performed with TOPAS Academic 4.1 [28] applying the fundamental parameter approach.

Mössbauer Spectroscopy and Superconducting Quantum Interference Device

Mössbauer spectra were obtained at room temperature, 150, 87.5 K and 4.2 K with a constant acceleration transmission mössbauer spectrometer and ^{57}Co (Rh) source. A α-Fe foil was used to calibrate the mössbauer spectrometer in a velocity range of ±10 mms^{-1}. Magnetic measurements were carried out using a Quantum Design MPMS-XL SQUID magnetometer.

Catalytic Activity

Polymer functionalized Ni@Fe_2O_3 NPs (0.02mg/mL) were mixed with a solution of bromophenol blue (4.7μM) (Cat. No. B0126, Sigma, Germany) and the reaction was followed for 6h at room temperature by recording continuous scans (200-800nm) at certain time periods (1, 2, 3, 4, 5 and 5h) using a Cary 5G UV-Vis-NIR spectrophotometer (Varian Inc., Palo Alto, CA, USA). As controls, Ni NPs (4 nm) and Fe_2O_3 NPs (10 nm) synthesized as reported elsewhere were mixed with a solution of bromophenol blue (4.7μM) and left to react for 6h at room temperature. Polymer functionalized Ni@Fe_2O_3 NPs (0.02mg/mL) were mixed with phosphate buffered solution (PBS, pH 7.2) for 30 min at room temperature. The supernatant was removed by making use of the magnetic properties of Ni@Fe_2O_3 NPs and these ressuspended in distilled water to obtain the initial concentration (e.g. 0.02mg/mL). To a solution of bromophenol blue (4.7uM), the heterodimeric Ni@Fe_2O_3 nanoparticles were added and the reaction was left to react for 6 at room temperature

Reutilization Assay

Polymer functionalized Ni@Fe_2O_3 NPs (0.02mg/mL) were mixed with a solution of bromophenol blue (4.7μM). After 1h of incubation at room temperature, the absorbance measured at 590 nm using a Cary 5G UV-Vis-NIR spectrophotometer (Varian Inc., Palo Alto, CA, USA). The NPs were retrieved using a magnet, the supernatant removed, a new solution of bromophenol blue (4.7μM) added to the cuvette and after 1h of incubation the absorbance at 590 nm measured. The procedure as repeated for 7 consecutive cycles.

Mass Spectrometry

Polymer functionalized Ni@Fe_2O_3 NPs (0.02mg/mL) were mixed with a solution of bromophenol blue (4.7μM). After 6 h the reaction was stopped by the magnetic removal of the NPs and the supernatant further analyzed. As control, only bromophenol blue (4.7μM) was analyzed in parallel. The MALDI-TOF-CID experiments were performed on an Axima-TOF2 spectrometer (Shimadzu Biotech, Manchester, UK), equipped with a nitrogen laser (337 nm), a high-resolution ion gate for the selection of parent ions and a collision cell. The

width of the window for selecting the parent ion ranged from 2 to 10 Da. Argon was used as the collision gas at a pressure of $8x10^6$ mbar. The pulsed extraction ion source accelerated the ions with an acceleration voltage of 20 kV. All measurements were performed in the positive reflection mode with an accumulation of 441 scans *per* spectrum. The data acquisition, evaluation and generation of the spectra were performed with the software MALDI-MS Shimadzu Biotech Launchpad 2.7.2.20070105 (Kratos Analytical LTD. 2007). The software ACD/ MS fragmenter V10.1 (Advanced Chemistry Development, Inc., Toronto, Ontario, Canada) was used for the interpretation of the fragment spectra.

5.5. References

[1] (a) T. Hyeon, *Chem. Commun.* **2003**, *8*, 927. (b) J. Gao, H. Gu and B. Xu, *Accounts of Chemical Research* **2009**, *42*, 1097.

[2] (a) H. Gleiter and P. Marquardt, *Z. Metallkd.* **1984**, *75*, 263. (b) V. Nandwana, G. S. Chaubey, K. Yano, C.B. Rong and J. P. Liu, *journal of applied physics* **2009**, *105*, 014303. (c) L. V. Brown, H. Sobhani, J. B. Lassiter, P. Nordlander and N. J. Halas, *ACS Nano* **2010**, *4*, 819.

[3] (a) M. Bawendi, M. L. Steigerwald and L. E. Brus, *Annu. Rev. Phys. Chem.* **1990**, *41*, 477. (b) O. P. Rodríguez, U. Pal, M. C. Quiles, L. Rodríguez-Fernandez, M. Garriga and M. I. Alonso, *J. Phys. Chem. C* **2011**, *115*, 6410. (c) D. K. Lim, K. S. Jeon, H. M. Kim, J. M. Nam and Y. D. Suh, *Nature materials* **2010**, *9*, 60.

[4] (a) L. E. *Brus*, *J. Phys. Chem.* **1986**, *90*, 2555. (b) N. Zhao, L. Li, T. Huang and L. Qi, *Nanoscale* **2010**, *2*, 2418. (c) R. Klajn, A. O. Pinchuk, G. C. Schatz and B. A. Grzybowski, *Angew. Chem. Int. Ed.* **2007**, *46*, 8363.

[5] C. Wang, H. Daimon, and S. Sun, *Nano Lett*. **2009**, *9*, 1493.

[6] (a) H. Yu, M. Chen, P. M. Rice, S. X. Wang, R. L. White and S. Sun, *Nano Lett.* **2005**, *5*, 379. (b) Y. Wei, R. Klajn, A. O. Pinchuk and B. A. Grzybowski, *Small* **2008**, *4*, 1635. (c) C. Xu, J. Xie, D. Ho, C. Wang, N. Kohler, E. G. Walsh, J. R. Morgan, Y. E. Chin and S. Sun, *Angew. Chem.* **2008**, *120*, 179; *Angew. Chem. Int. Ed*. **2008**, *47*, 173. (d) Y. Wei, K. J. M. Bishop, J. Kim, S. Soh, and B. A. Grzybowski, *Angew. Chem*. **2009**, *121*, 9477; *Angew. Chem. Int. Ed*. **2009**, *48*, 9477.

[7] G. Lopes, J. M. Vargas, S. K. Sharma, F. Beron, K. R. Pirota, M. Knobel, C. Rettori, and R. D. Zysler, *J. Phys. Chem. C* **2010**, *114*, 10148.

[8] T. D. Schladt, M. I. Shukoor, M. N. Tahir, F. Natalio, K. Schneider, I. Ament, J. Becker, F. Jochum, S. Weber, P. Theato, L. M. Schreiber, C. Sönnichsen, H. C. Schröder, W. E. G. Müller and W. Tremel, *Angew. Chem.* **2010**, *122*, 4068; *Angew. Chem. Int. Ed.* **2010**, *49*, 3976.

[9] S.-H. Choi, H. B. Na, Y. I. Park, K. An, S. G. Kwon, Y. Jang, M.-H. Park, J. Moon, J. S. Son, I. C. Song, W. K. Moon and T. Hyeon, *J. Am. Chem. Soc*. **2008**, *130*, 15573.

[10] (a) H. T. Zhang, G. Wu, X. H. Chen and X. G. Qiu, *Mater. Res. Bull.* **2006**, *41*, 495. (b) B. J. Park, E. Kang, S. Uk. Son, H. M. Park, M. K. Lee, J. Kim, K. W. Kim, H.-J. Noh, J.-H. Park, C. J. Bae, J.-G. Park and T. Hyeon, *Adv. Mater*. **2005**, *17*, 429.

[11] M. Han, Q. Liu, J. H. He, Y. Song, Z. Xu and J. M. Zhu, *Adv. Mater.* **2007**, *19,* 1096.

[12] B. Nakhjavan, M. N. Tahir, F. Natalio, H. Gao, K. Schneider, T. Schladt, , I. Ament, R. Branscheid, S. Weber, U. Kolb, C. Sönnichsen, L. M. Schreiber and W. Tremel, *J. Mater. Chem.* **2011**, *21,* 8605.

[13] (a) J. L. Snoek, *Rev. Tech. Philips* **1946**, *8,* 359. (b) E. F. Bertaut *I. Phys. Radium* **1951**, *12,* 252. (c) K. Stierstadt, *Z. Phys*. **1956**, *146,* 169. (d) J. B. Goodenough and A. L. Loeb, *Phys. Rev*. **1953**, *98,* 391. (e) X. X. Tang, A. Manthiram and J. B. Goodenough, *J. Solid State Chem.* **1989**, *79,* 250.

[14] B. Nakhjavan, M. N. Tahir, M. Panthöfer, H. Gao, T. Gasi, V. Ksenofontov, R. Branscheid, S. Weber, U. Kolb, L. M. Schreiber and W. Tremel, *Chem. Commun.* **2011**, *47,* 8898.

[15] (a) N. Saito, T. Kanbara, T. Sato and T. Yamamoto, *Polymer Bulletin* **1993**, *30,* 285. (b) Y. H. Budnikova and Y. M. Kargin, *Journal of Organometallic Chemistry* **1997**, *536-537*, 265.

[16] (a) Y. H. Tee, L. Bachas and D. Bhattacharyya, *J. Phys. Chem. C* **2009**, *113,* 9454. (b) B. Schrick, J. L. Blough, A. D. Jones and T. E. Mallouk, *Chem. Mater.* **2002**, *14,* 5140. (c) F. Alonso, P. Riente, J. A. Sirvent and M. Yus, *Appl. Catal. A: Gen.* **2010**, *378*, 42.

[17] R. W. Cheary and A. A. Coelho, *J. Appl. Crystallogr*. **1992**, *25,* 109.

[18] N. N. Greenwood and T. G. Gibb, *Mössbauer Spectroscopy*; Chapman and Hall Ltd: London, **1971**.

[19] M. Ali, P. Ramirez, M. N. Tahir, S. Mafe, Z. Siwy, R. Neumann, W. Tremel and W. Ensinger, *Nanoscale* **2011**, *3*, 1894.

[20] Y. Miyazaki and T. Yamamoto, *synthetic metals* **1995**, *69,* 317.

[21] S. E. Manahan, *Environmental Chemistry*; CRC Press Inc: Boca Raton, FL, **1994**.

[22] J. A. Roth, S. R. Dakojl, R. C. Hughes and R. E. Carmody, *Environ. Sci. Technol.* **1994**, *28*, 80.

[23] (a) J. H. Sinfelt, *Rev. Mod. Phys.* **1979**, *51,* 569. (b) A. E. Berkowitz, *IEEE Trans. Magn.* **1986**, *22,* 466. (c) A. Pankhurst and R. J. Pollard, *J. Phys. Condens. Matter*. **1993**, *5,* 8487. (d) F. Bpdker, S. M@rup, and S. Linderoth, *Phys. Rev. Lett.* **1994**, *72,* 282.

[24] C. A. Tolman, *J. Am. Chem. Soc.* **1970**, *92,* 2956.

[25] Potavova, R. Mruk, S. Prehl, R. Zentel, T. Basche and A. Mews, *J. Am. Chem. Soc.* **2003**, *125*, 320.

[26] A. Taylor, *JIMEAP*, **1952**, *81*, 451.

[27] C. Greaves, *J. Solid State Chem.* **1983**, *49*, 325.

[28] A. Coelho, *TOPAS Academic V 4.1*; *Coelho Software:* Brisbane, AUS, **2007**.

6. Synthesis of Monodisperse Dumbbell-Like $Pt@Fe_3O_4$ Nanoparticles

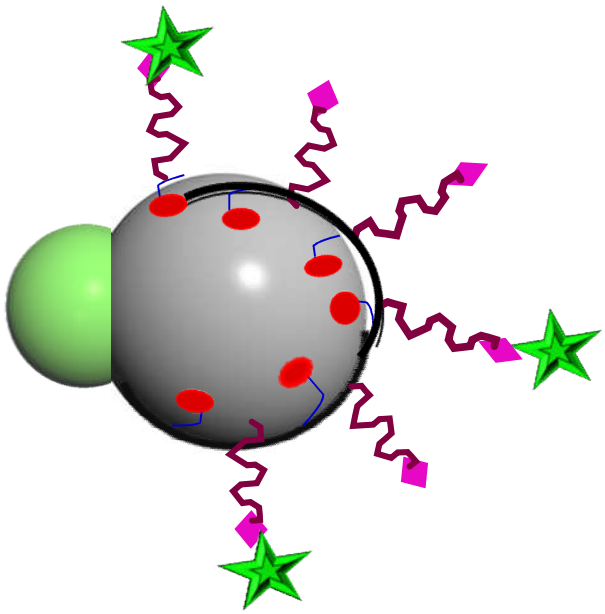

Bahar Nakhjavan[a], Muhammad Nawaz Tahir[a], Robert Branscheid[b], Stefan Weber[c], Ute Kolb[b], Laura Maria Schreiber[c], Wolfgang Tremel[a*]

[a]*Institut für Anorganische Chemie und Analytische Chemie, Johannes Gutenberg-Universität, Duesbergweg 10-14, D-55099 Mainz, Germany. Fax: +49 6131 39-25605; Tel: +49 6131 39-25135; E-mail: tremel@uni-mainz.de*
[b]*Institut für Physikalische Chemie, Johannes Gutenberg-Universität, Welderweg 11, 55099 Mainz, Germany.*
[c]*Bereich Medizinische Physik, Klinik und Poliklinik für diagnostische und interventionelle Radiologie, Klinikum der Johannes Gutenberg-Universität Mainz. Langenbeckstraße, 1, 55131, Mainz, Germany.*

In preparation

6.1. Introduction

Significant attention to develop novel synthetic protocol for nanoparticles is stimulated due to their technological importance, as they demonstrate unique electrical, optical and magnetic behavior, which differ from their respective bulk materials [1-3]. Magnetic nanoparticles with the size in the range between 2 to 10 nm are particularly important because they are potentially useful in terabit magnetic storage, as carriers for biochemical complexes, MRI contrast enhancing agents. [4].

Nobel metal and magnetic materials exhibited interesting optical and magnetic properties such as surface plasmon resonance (SPR) absorption and superparamagnetism, as their size was scaled down to nanometers [5, 6]. Moreover, the engineered heterostructured nanoparticles including magnetic and nobel metals are joined together in the absence of a mediator (i.e. a linking molecule) create a new nanocomponent with multifunctional and novel properties [7, 8].

In recent years, Platinum nanoparticle has attracted so much attention due to their superior properties and potential applications specially as catalysts in fuel cells and for analysis of various types of biomolecules [9-11]. Moreover, it is one of the most researched noble metals because it is very stable and it is resistant to oxidation under ambient atmospheric conditions. Iron-Platinum (FePt) alloys nanoparticles have been widely used in different formulas and in numerous areas due to their magnetic behaviors [12-14]. The bimetallic Fe–Pt nanoparticles are promising candidates, not only for magnetic storage, but also for *in vivo* applications because they show extremely stable behaviors in the presence of oxygen [15].

Consequently, the use of platinum and Fe_3O_4 beside each other can offer unique advantages and applications such as catalytic activities. Herein, we report a facile protocol to synthesize heterodimer nanoparticles of $Pt@Fe_3O_4$. This synthesis was carried out by the thermal decomposition of $Fe(CO)_5$ and reduction of Platinum(II) acetylacetonate in hot organic solvent in the presence of stabilizers. In this present work, the formation of asymmetric $Pt@Fe_3O_4$ heterodimer NPs is explained by the epitaxial growth of iron oxide onto the platinum interfacial area. These nucleation and growth phases at a specific facet lead to an asymmetric dumbbell-like structure. Dumbbell-like nanoparticles demonstrate an important type of heterogeneous nanostructures containing two different particles that are epitaxially linked and have two different types of material surfaces [16].

This $Pt@Fe_3O_4$ nanoparticle was reported for the first time in two-step reaction by producing

platinum nanoparticles separately, in the first step and then the nucleation and growth of iron onto Pt nanoparticles followed by Fe oxidation [17]. However, in this work, we present one pot chemical synthesis route for the nucleation and growth of both components simultaneously which results in the formation of monodisperse, uniform size and morphology Pt@Fe_3O_4 heterodimeric NPs in less time. In spite of the formation of core-shell structures where the second precursor starts to nucleate and grow uniformly around the pre-existing seeds, we obtained asymmetric heterostructures. This procedure can be generalized for the synthesis of more heterodimeric nanoparticles using various chemical precursors.

6.2. Results and Discussion

Transmission electron microscope (TEM) and high resolution transmission electron microscope (HRTEM) images show the synthesized Pt@Fe_3O_4 nanoparticles with 4-6 nm platinum and 4-6 nm iron oxide nanoparticles (Figure 6.1a and b). Figure 6.1b illustrates the epitaxial relation between platinum and iron oxide and confirms the diffusion of lattice fringes by the growth of iron oxide on platinum. Since decomposition temperatures for these two chemical precursors are little far from each other (265ºC for $Pt(acac)_2$ and 180ºC for $Fe(CO)_5$), the combination of $Pt(acac)_2$ reduction and $Fe(CO)_5$ decomposition simultaneously results to these nanoparticles. Octadecane as a solvent, oleylamine as a reductant agent and oleic acid as a stabilizing agent play important roles in shape and size controlling in this work.

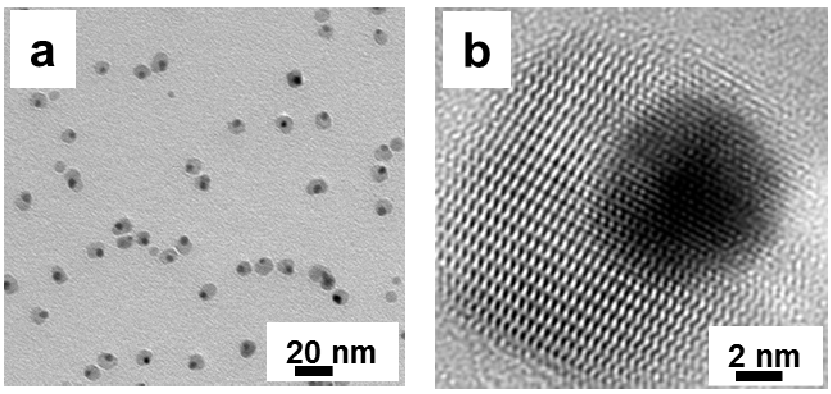

Figure 6.1. *(a) TEM image of Pt@Fe_3O_4 nanoparticles and (b) HRTEM image of an individual nanoparticle.*

The elemental composition was determined by both, line scan EDX and elemental mapping using scanning transmission electron microscopy (STEM) combined with energy dispersive x-ray spectroscopy (EDS). Due to its higher electron density platinum showed brighter spots

compared to magnetite which appears darker in the STEM image in Figure 6.2a. It was also confirmed from the EDX-mapping (Figure 6.2a) that yellow spots (platinum) correspond to the brighter areas of the STEM image in (Figure 6.2a) and darker areas are composed of Fe and O which appears orange brown and red in the EDS elemental mapping. Figure 6.2b represents the EDX line scan profiles of the Pt@Fe_3O_4 nanoparticles.

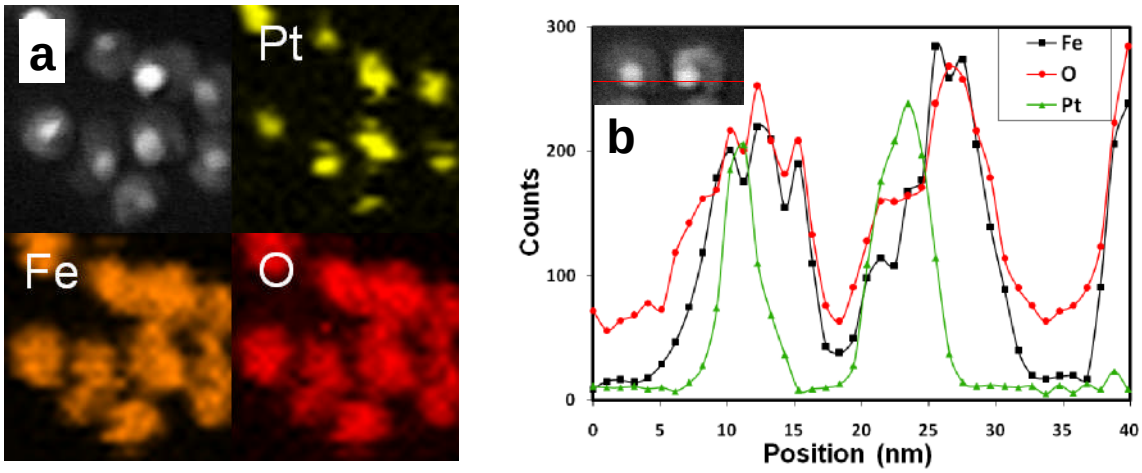

Figure 6.2. *Elemental mapping of synthesized dumbbell-like Pt@Fe_3O_4 heterodimer. (a) STEM mode image and corresponding elemental maps of Pt (yellow), Fe (orange) and O (red) obtained by recording spatial distribution. (b) EDS line scan profiles confirm the presence of platinium, iron and oxygen.*

Figure 6.3 presents the XRD pattern of as synthesized Pt@Fe_3O_4 heterodimer nanoparticles. The positions and relative intensities of the reflections match well with those of standard Fe_3O_4 and Pt powder diffraction data, indicating that the synthesis yielded a nano-heterodimer consisting of magnetite (space group 227, Fd-3m) and Pt (space group 225, Fm-3m).

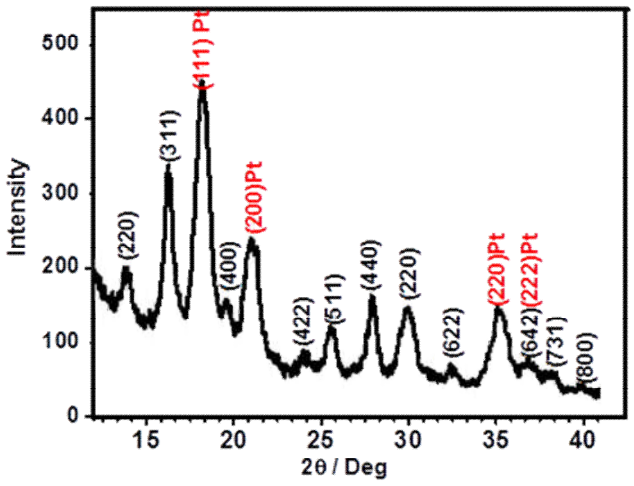

Figure 6.3. *X-ray diffraction patterns of Pt@Fe_3O_4 nanoparticles.*

Figure 6.4a shows the hysteresis loops for the Pt@Fe_3O_4 nanoparticles measured at room temperature and at 5 K. The room magnetization versus field curve for these nanoparticles shows zero coercivity, while the curve exhibits finite coercivity of 119 Oe at 5 K. This is a typical characteristic of nanosized particles which are superparamagnetic at room temperature. Figure 6.4b illustrates the temperature dependence of the magnetization for the field, cooled (FC) and zero field cooled (ZFC) curves. As indicated by the ZFC-FC curves in this figure, the Pt@Fe_3O_4 nanoparticle has a low blocking temperature of 106 K as compared with other heterodimer nanoparticles.

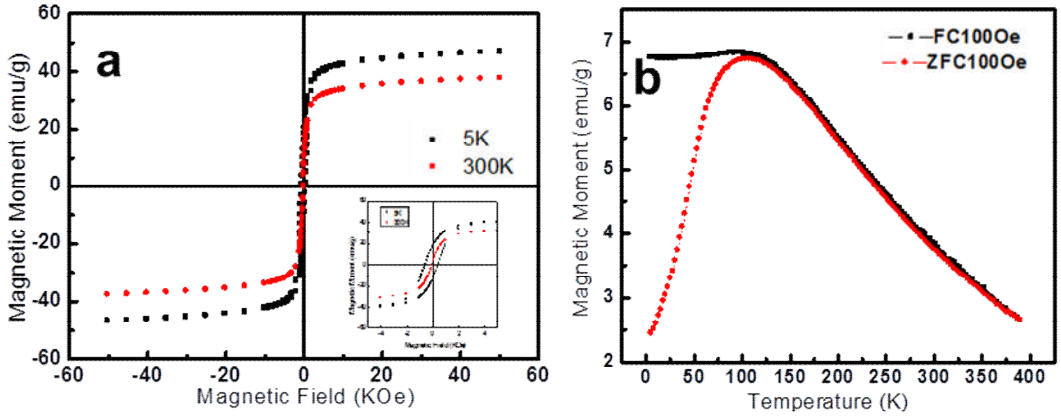

Figure 6.4. *(a) Hysteresis loop of* Pt@Fe_3O_4 *nanoparticles, (b) temperature dependence of magnetization in field cooling (FC) and zero field cooling (ZFC).*

In order to functionalized Pt@Fe_3O_4 nanoparticles, we have used the multifunctional polymeric ligand with catechol anchor groups and PEG-linkers ($M_r \approx 800$) with free amino groups (Figure 6.5a) [18]. After functionalization with multifunctional polymeric ligand, their solubility and stability against aggregation and precipitation in deionized water over weeks made them eligible to be used specifically in biomedical applications (Figure 6.5b).

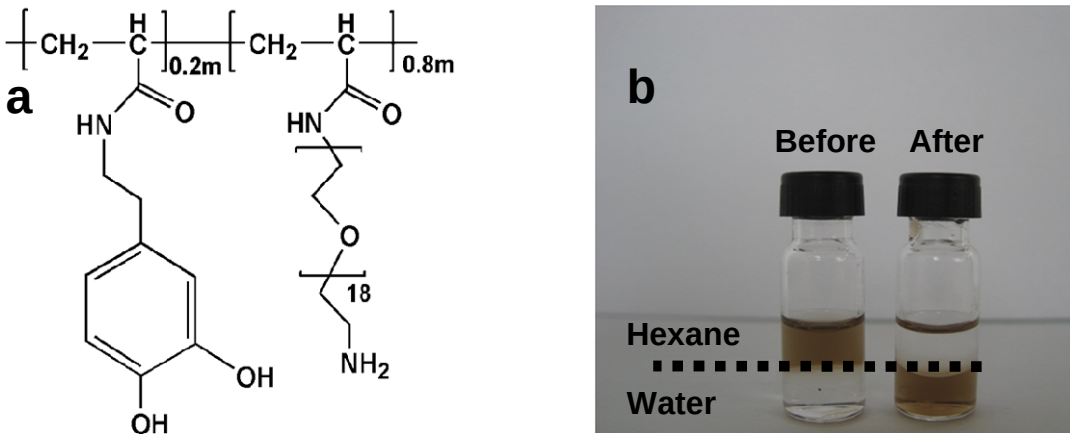

Figure 6.5. *(a) Scheme of polymeric ligand. (b) Digital photograph of Pt@Fe_3O_4 solutions before (left) and after (right) surface functionalization in hexane (top layer) and in water (bottom layer).*

As reported before by Gao et al, these FePt@Fe_2O_3, FePt@Fe_3O_4, Pt@Fe_2O_3 magnetic nanostructures have shown strong MR relaxation enhancement [19]. Therefore, they can open up a new avenue to multimode and multipurpose biomedical applications because of their integrated functions. Concerning biomedical applications, superparamagnetic nanoparticles have attractive as contrast agents for magnetic resonance imaging. Figure 6.6 shows T_1 and T_2-weighted MR image of three different Pt@Fe_3O_4 nanoparticles concentrations. The functionalized NPs were dissolved in saline solution (concentrations from 0.004 to 0.018 mM for Pt@Fe_3O_4. T_1 and T_2 measurements revealed T_1 and T_2 relaxivities of 218.14 and 1621,8 $mM^{-1}ms^{-1}$ for the Pt@Fe_3O_4.

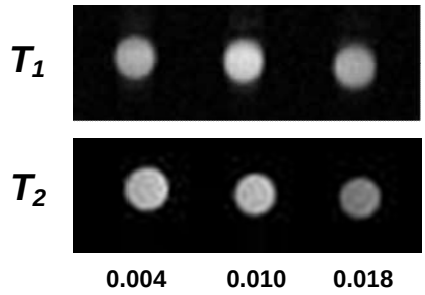

Figure 6.6. *T_1 and T_2-weighted MRI image of solutions containing polymer functionalized $Pt@Fe_3O_4$ NPs (concentrations in mM).*

6.3. Summary and Outlook

In summary, we have shown that a heterodimer of two nanocomponents conatining Pt and iron oxide can be made easily by a one-pot chemical synthesis of two different phase transition temperatures. In futrue, the formation of other multifunctional dimer or trimers should be possible just by understanding different surface chemistry, nucleation and growth procedures. In spite of many disadvantages and limitations for cisplatin, *cis*-diamminedichloro platinum(II), it has been widely used as a powerful therapeutic agent against numerous solid tumors in the biomedical area [20]. These $Pt@Fe_3O_4$ nanoparticles with good solubility and stability in water solution in compare with cisplatin and also with high contrast enhancement in MRI can be a suitable choice in cancer therapy.

6.4. Experimental Section

Methods and Material

Iron(0) pentacarbonyl ($Fe(CO)_5$, 99.5%, Acros), platinum(II) acetylacetonate ($Pt(acac)_2$, 98%, acros), oleic acid (90%, Aldrich), oleylamine (90%, Acros), 1-octadecene (ODE, 90% Acros) di-tert-butyl dicarbonate ($(Boc)_2O$, >99%, Aldrich), dioxane (p.A. Fisher), $H_2N\text{-}PEG_{(800)}\text{-}NH_2$ (Aldrich), triethylamine (>99%, Aldrich), 3-hydroxy tyramine hydrochloride (Dopamine.HCl) (98%, Aldrich), trifluoroacetic acid (TFA) (99%, Aldrich), ethanol (99.8%, Roth), toluene (>99%, Aldrich), hexane (p.A. Fisher), dichloromethane DCM (p.A. Fisher), dimethylformamide (DMF) (extra dry, >99.8%, Acros) and diethyl ether (p.A. Fisher) were used as received without further purification.

Synthesis of $Pt@Fe_3O_4$ Heterodimer Nanoparticles

Under a constant flow of argon (Ar), 1 mmol $Pt(acac)_2$, 3 mmol oleic acid, 3 mmol

oleylamine and 10 ml octadecane were mixed. The solution was heated to 120ºC with a constant rate of 3ºC/min. After reaching to this temperature, 4 mmol $Fe(CO)_5$ was added and the temperature was raised to 280ºC and kept at this temperature for 20 minutes. The product was precipitated by the addition of excess of ethanol and collected by centrifugation (9000 rpm, 10 min, RT). The nanoparticles were repeatedly washed by dissolving them in hexane, precipitating them with ethanol and centrifugation (9000 rpm, 10 min, RT). Finally, the product was dissolved in toluene, flushed with argon (Ar) and stored at +4ºC.

Synthesis of Boc Protected Bis-Amine $PEG_{(800)}$ (NBoc-$PEG_{(800)}$-NH_2)

A solution of $(Boc)_2O$ (0.02 mol) in 30 mL of anhydrous dioxane was added drop wise to a solution of NH_2-$PEG_{(800)}$-NH_2 (0.1 mol) in 50 mL anhydrous dioxane. The resulting solution was stirred overnight at room temperature. The solvent was evaporated and the oily product obtained was dissolved in 50 mL of water and extracted thrice using 50 mL of CH_2Cl_2. The combined organic phases were washed with a conc. solution of NaCl and dried over anhydrous Na_2SO_4. The resulting organic phase was concentrated by rotary evaporation and viscous, colorless oil was obtained. Further purification was achieved by flash chromatography on silica using a CH_2Cl_2/ethanol mixture (2:1) as eluent.

Preparation of the Polymer

The poly (active ester) poly(pentafluorophenyl acrylate) (PFA) was prepared as reported earlier [21-24]. GPC analysis of the obtained polymer (THF, light scattering detection) gave the following values: M_n = 16,390 g/mol, with PDI = 1.39, with an average of 70 repeating units. For the synthesis of the multifunctional poly(acrylamides), poly(active ester) poly(pentafluorophenyl acrylate) (700 mg, 2.94 mmol repeating units) was dissolved in a mixture of 9 mL of dry DMF and 0.7 mL of triethylamine. After that, 3-hydroxytyramine hydrochloride (24 mg) dissolved in 3 mL DMF and 0.4 mL triethylamine was added and the reaction mixture was stirred for 3 hours at 50°C. In the final step the remaining active ester groups were substituted using an excess of NBoc-$PEG_{(800)}$-NH_2 (dissolved in 3 mL dry DMF) and stirring for 5 h at 50°C. The solution was concentrated to about 2 mL and the polymeric ligand was precipitated by the addition of cold ethyl ether. The precipitated polymer was centrifuged (9000 rpm, 10 min and RT) and the solvent was decanted. Upon drying, 286 mg of colorless oil was obtained.

Cleavage of the Boc Group

The polymer obtained above was dissolved in CH_2Cl_2 (30 mL). After that trifluoroacetic acid (2.0 mL) was added and the mixture was stirred at room temperature for 2 h. After that the

reaction solution was treated with the mixture of water and hexane (30 mL/50 mL) and vigorously stirred for 30 minutes. The aqueous phase containing the polymer was separated and concentrated to 2 mL and dialysed against deionized water for 2 days at room temperature (cellulose membrane, MWCO = 3,500). Finally, the water was evaporated and the product was redissolved in $CHCl_3$ and to make a stock solution, which was kept at +4ºC.

Functionalization of $Pt@Fe_3O_4$ Nanoparticles

$Pt@Fe_3O_4$ nanoparticles (10 mg) were dispersed in 15 mL of $CHCl_3$ by slowly dropping over 1 h into the above synthesized polymeric ligand solution (20 mg/10 mL, chloroform). The reaction was continuously stirred overnight at room temperature, under inert conditions. The functionalized nanoparticles were precipitated by the addition of hexane and separated from unbound polymer and surfactants by centrifugation. These nanoparticles were washed twice by dissolving them in chloroform and precipitating them with hexane. Finally, the particles were stored in or DMF at +4ºC.

Physical Characterization

Electron Microscopy

The size and morphology of the naked and surface functionalized $Pt@Fe_3O_4$ nanoparticles were investigated using transmission electron microscopy (TEM, Philips EM 420 instrument with an acceleration voltage of 120 kV). Samples for transmission electron microscopy were prepared by placing a drop of dilute nanoparticle solution in hexane on a carbon coated copper grid. Low-resolution TEM images were recorded on a Philips EM420 microscope operating at an acceleration voltage of 120 kV. High-resolution TEM data and ED patterns were obtained on a FEI Tecnai F30 S-TWIN with a 300 kV field emission gun.

X-Ray Diffraction

X-ray powder diffraction measurements were performed on a Bruker D8 Advance powder diffractometer, operating with Mo-Kα radiation equipped with a Sol-X energy-dispersive detector.

Superconductive Quantum Interference Device

The magnetic properties of powder samples were measured with a superconductive quantum interference device (SQUID, Quantum Design MPMS XL).

Magnetic Resonance Imaging

MR signal enhancement effects were measured for the aqueous solutions of functionalized $Pt@Fe_3O_4$ nanoparticles at different Fe concentrations (measured with AAS) on a clinical 3.0 T MRI scanner (Magnetom Trio, Siemens Medical Solutions, Erlangen, Germany). Signal

reception and radio frequency (RF) excitation was performed using 8-channel knee coil. For T_1-measurement, a saturation prepared (SR) snapshot fast low angle shot (SR-TurboFLASH) pulse sequence with repetition time (T_R) / echo time / flip angle = 3.0 ms/1.5 ms/20° was used with varying saturation times starting from 20 ms up to 8000 ms. For measuring T_2 relaxation time, a multi-echo spin-echo pulse sequence (CPMG, Carr-Purcell-Meiboom-Gill) with a total of 32 echos and T_R = 5000 ms was used, the echo time was varied from 7 ms to 224 ms. In a second T_2 measurement T_E was varied from 15 ms up to 480 ms.

6.5. References

[1] C. B. Murray, C. R. Kagan and M. G. Bawendi, *Science* **1995**, *270*, 1335.

[2] A. P. Alivisatos, *Science* **1996**, *271*, 933.

[3] F. Caruso, *Adv. Mater*. **2001**, *13*, 11.

[4] S. h. Sun, C. B. Murray, D. Weller, L. Folks and A. Moser, *Science* **2000**, *287*, 1989.

[5] C. M. Shen, C. Hui, T. Z. Yang, C. W. Xiao, J. F. Tian, L. H. Bao, S. T. Chen, H. Ding and H. J. Gao, *Chem. Mater.* **2008**, *20*, 6939.

[6] Z. C. Xu, C. M. Shen, Y. L. Hou, H. J. Gao and S. Sun, *Chem. Mater.* **2009**, *21*, 1778.

[7] (a) D. J. Milliron, S. M. Hughes, Y. Cui, L. Manna, J. Li, L.-W. Wang and A. P. Alivisatos, *Nature* **2004**, *430*, 190, (b) L. Carbone and P. D. Cozzoli, *Nano Today* **2010**, *5*, 449, (c) R. Hao, R. Xing, Z. Xu, Y. Hou, S. Gao and S. Sun, *Adv. Mater.* **2010**, *22*, 2729.

[8] (a) Y. Cao and U. Banin, *J. Am. Chem. Soc.* **2000**, *122*, 9692, (b) Y. Pan, J. Gao, B. Zhang, X. Zhang and B. Xu, *Langmuir* **2010**, *26*, 4184.

[9] R. J. Davis and E. G. Derouane, *Nature* **1991**, *249*, 313.

[10] (a) M. Studer, H. U. Blaser and C. Exner, *Adv. Synth. Catal.* **2003**, *245*, 45. (b) M. Che and C. O. Bennett, *Adv. Catal.* **1989**, *36*, 55.

[11] K. Shrivas, K. Agrawal and H. F. Wu, *Analyst* **2011**, *136*, 2852.

[12] F. X. Redl, K. S. Cho, C. B. Murray and S. O'Brien, *Nature* **2003**, *423*, 968.

[13] H. Zeng, J. Li, J. P. Liu, Z. L. Wang and S. H. Sun, *Nature* **2002**, *420*, 395.

[14] S. H. Sun, C. B. Murray, D. Weller, L. Folks and A. Moser, *Science* **2000**, *287*, 1989.

[15] D. Kim, D. Kan, T. Veres, F. Normadin, J. K. Liao, H. H. Kim, S. H. Lee, M. Zahn and M. Muhammad, *Journal of applied Physics* **2005**, *97*, 10Q918.

[16] (a) H. W. Gu, R. K. Zheng, X. X. Zhang and B. Xu, *J. Am. Chem. Soc.* **2004**, *126*, 5664. (b) K. W. Kwon and M. Shim, *J. Am. Chem. Soc.* **2005**, *127*, 10269. (c) H. Yu, M. Chen, P. M. Rice, S. X. Wang, R. L. White and S. H. Sun, *Nano Lett.* **2005**, *5*, 379.

[17] C. Wang, H. Diamon and S. Sun, *Nano Lett.* **2009**, *9*, 1493.

[18] M. I. Shukoor, F. Natalio, N. Glube, M. N. Tahir, H. A. Therese, V. Ksenofontov, N. Metz, P. Theato, P. Langguth, J.-P. Boissel, H. C. Schröder, W. E. G. Müller and W. Tremel, *Angew. Chem. Int. Ed.* **2008**, *47*, 4748.

[19] J. Gao, H. Gu and B. Xu, *accounts of chemical research* **2009**, *42*, 1097.

[20] (a) B. Rosenberg, L. Vancamp and T. Krigas, *Nature* **1965**, *205*, 698. (b) Y. W. Jung

and S. J. Lippard, *Chem. Rev.* **2007**, *107*, 1387. (c) E. Wong and C. M. Giandomenico, *Chem. Rev.* **1999**, *99*, 2451. (d) M. A. Fuertes, C. Alonso and J. M. Perez, *Chem. Rev.* **2003**, *103*, 645.

[21] I. Potavova, R. Mruk, S. Prehl, R. Zentel, T. Basche and A. Mews, *J. Am. Chem. Soc.* **2003**, *125*, 320.

[22] M. Eberhardt, R. Mruk, P. Theato and R. Zentel, *Eur. Polym. J.* **2005**, *41*, 1569.

[23] M. N. Tahir, M. Eberhardt, H. A. Therese, U. Kolb, P. Theato, W. E. G. Müller, H. C. Schröder and W. Tremel, *Angew. Chem. Int. Ed.* **2006**, *45*, 4803.

[24] M. N. Tahir, M. Eberhardt, P. Theato, S. Faiß, A. Janshoff, T. Gorelik, U. Kolb and W. Tremel, *Angew. Chem. Int. Ed.* **2006**, *45*, 908.

7. Conclusion and Outlook

This doctoral thesis presents a simple route for synthesizing of novel various heterodimers and ternary phase ferrite nanoparticles. It is worth to state that the methods used for synthesizing all mentioned nanoparticles are identical called “thermal decomposition”. This procedure is based on the precursor’s decomposition temperatures and reaction conditions. In this work, we tried to control the reaction kinetic by understanding of the nucleation and growth steps. Furthermore, due to their magnetic properties that these nanoparticles have shown they could further be used as magnetic materials for the development of innovative and interesting applications.

After a short introduction about nanotechnology and magnetic nanoparticles in the first chapter, we have described the novel synthesis of $Cu@Fe_3O_4$ heteroparticles with distinct morphologies from organometallic reactants in the second chapter. The shape of magnetic domains can be controlled by choosing the suitable solvent and reaction conditions. They display magnetic and optical properties that are useful for simultaneous magnetic and optical detection. After functionalization, the $Cu@Fe_3O_4$ heterodimers become water soluble. The morphology, structure, magnetic and optical properties of the as synthesized heterodimer nanoparticles were characterized using transmission electron microscopy (TEM), x-ray diffraction (XRD), mössbauer spectroscopy, superconducting quantum interference device (SQUID) and dark field imaging. A special advantage of these heterodimers lies in the fact that the nanodomains of different composition can be used for the formation of nitric oxide (NO) through the Cu domain and heterodimer nanoparticles can be removed from the reaction mixture by means of the magnetic domain (Fe_3O_4).

Since magnetic nanocrystals have attracted great interest for a fundamental understanding of nanomagnetism and for their technological applications, in the third chapter, we have successfully synthesized monodispesed $Cu_xFe_{3-x}O_4$ nanocrystals ($x \sim 0.32$) from $Cu(HCOO)_2$ and $Fe(CO)_5$ using oleic acid and oleylamine as surfactants for the first time. The nanocrystals were characterized by high-resolution transmission electron microscopy (HRTEM), electron diffraction (ED), magnetization studies and mössbauer spectroscopy. $Cu_xFe_{3-x}O_4$ particles are superparamagnetic at room temperature 300 K with a saturation magnetization of 30.5 emu/g. Below their blocking temperature of 60 K, they become ferrimagnetic and at 5 K, they show a coercive field of 122 Oe and a saturation magnetization of 36.1 emu/g. The $Cu_xFe_{3-x}O_4$ nanoparticles were functionalized using a hydrophilic multifunctional polymeric ligand

containing $PEG_{(800)}$ groups and a fluorophore. By virtue of their magnetic properties these nanoparticles may serve as contrast enhancing agents for magnetic resonance imaging (MRI).

In the fourth chapter, we have illustrated a wet chemical approach from organometallic reactants for the targeted synthesis of $Co@Fe_2O_3$ heterodimer and $CoFe_2O_4$ ferrite nanoparticles. They display magnetic properties that are useful for magnetic MRI detection. These nanostructures were characterized by transmission electron microscopy (TEM), high resolution transmission electron microscopy (HRTEM), x-ray diffraction (XRD), mössbauer spectroscopy, superconducting quantum interference device (SQUID) and electron diffraction (ED). After functionalization, they were studied in magnetic resonance imaging. The results show that they have this ability to be used as a MRI agent in comparison with commercial iron oxides.

In the fifth chapter, we have reported the simple synthesis of $Ni@Fe_2O_3$ heterodimeric nanocrystals through controlled and one-pot thermal decomposition of metal acetate and carbonyl precursors. As mentioned above, they were characterized by TEM, HRTEM, XRD, mössbauer and SQUID. Moreover, they were designed to play a catalytic role for dehalogenation reactions due to their due both magnetic and recyclable properties.

We have then presented the synthesis of dumbbell-like $Pt@Fe_3O_4$ nanoparticles. Although, these nanoparticles have been reported before the procedure described in the sixth chapter is more simple, straightforward and quick. After surface modification with specific ligand, they were used in MRI a contrast agent.

Conclusion and outlooks, methods and instrumentations and appendix are shown respectively in the seventh, eighth and ninth chapters.

This thermal decomposition temperature synthetic method, which has been used, for all nanoparticles in this thesis can be extended to the synthesis of other heterodimer or heterotrimer nanomaterials such as Ni@MnO or $Cu@Cu@Fe_3O_4$ and etc. Moreover, these multidomain particles can be used as building blocks for higher-order structures. Finally, these nanoparticles can be a promising candidate for molecular imaging when addressed to specific cells by using specific surface functionalization startegy.

Over the past decade, the synthesis of magnetic nanoparticles including different components and compositions with a wide range of size and shape has changed to an innovative and inventive subject. However, the synthesis of high quality magnetic nanostructured with a controlled procedure, and detailed understanding of reaction mechanism are still challenges to be developed in the near future. In the synthesis of initial magnetic metal and metal oxide

nanoparticles, toxic and costly precursors often used were problematic issues. Moreover, these nanoparticles were not water soluble and stable against agglomeration over some days. After several years attempt and efforts all these difficulties could be solved and replaced by the formation of water soluble and stable metal oxides or even metallic nanoparticles with simple and nontoxic precursors.

Metallic nanoparticles have a higher magnetization in comparison with their oxidic counterparts. In addition, these metallic nanoparticles have shown higher reactivity and toxicity which are beneficial for various applications but not for direct application in biomedicine. As a result, metallic nanoparticles should be coated or protected with a polymer or silica layer against the surrounding environment.

It is believed that the monodisperse magnetic nanostructures in different forms such as bi and multi metallic oxides, dopped material and metal oxides nanocomposites will show a wide range of applications mostly including information technology, biotechnology and biomedicine. For being used in biomedicine, they should be transferred to the aqueous phase after synthesizing in organic media. Therefore, functionalization with a specific ligand is one of the most important steps in the application of these magnetic nanoparticles in this area.

8. Methods and Instrumentations

8.1. Transmission Electron Microscopy

Transmission electron microscopy (**TEM**) is a microscopy technique whereby a beam of electrons is transmitted through an ultra thin specimen, interacting with the specimen as it passes through. From the interaction of the transmitted electrons through the specimen; the image is magnified and focused onto an imaging device, for example, a fluorescent screen, on a layer of photographic film, or to be detected by a sensor such as a CCD camera [1].

A TEM contains several components, including a vacuum system in which the electrons travel, an electron emission source for the generation of the electron stream, a series of electromagnetic lenses, as well as electrostatic plates. The latter two allow the operator to guide and manipulate the beam as required. In addition, it is a device to allow the insertion into, motion within and removal of specimens from the beam path. Imaging devices are subsequently used to create an image from the electrons that exit the system [2].

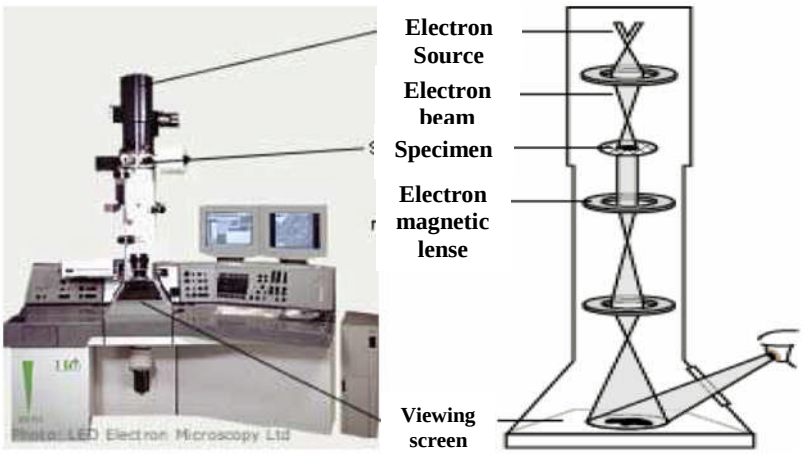

Figure 8.1. *Transmission Electron Microscope [2].*

The basic setup of TEM is displayed in Figure 8.1. It works very much like a standard light microscope: The light source is replaced by an electron gun. Either field emission or thermionic guns are put to use here. Before the sample, the condenser lense system focuses the electron beam and after the sample several further electromagnetic lens systems are

needed for increasing resolution, correcting astigmatism, and to shift the beam. The image is finally displayed on a fluorescent screen and recorded using photographic films or nowadays mostly CCD cameras. Due to the substantially shorter wavelength of electrons compared to visible light the resolution of TEMs can be much higher than in light microscopes (Abbe limit) and goes down to a few Ångström [3].

Scanning transmission electron microscopes (STEM) is a subgroup of TEMs. In these, electron optics focuses the beam into a spot with dimensions below nanometer size. This is then scanned across the sample and the picture is acquired point by point. It is especially useful for analysis techniques like energy dispersive x-ray spectroscopy [3].

In this doctoral work, TEM was carried out on a Philips EM420 instrument with a twin lens and a Philips CM12 with a twin lens at an acceleration voltage of 120 kV. High resolution images were taken with a Philips FEI TECNAI F30 ST electron microscope (field-emission gun, 300 kV extraction voltage) equipped with an Oxford EDX (energy-dispersive x-ray) spectrometer with a Si/Li detector and an ultrathin window for elemental analysis.

8.2. X-Ray Diffraction

X-ray scattering techniques are a family of non-destructive analytical techniques, which reveal information about the crystallographic structure, chemical composition and physical properties of materials. These techniques are based on observing the scattered intensity of an x-ray beam hitting a sample as a function of incident and scattered angle, polarization and wavelength or energy (Figure 8.2).

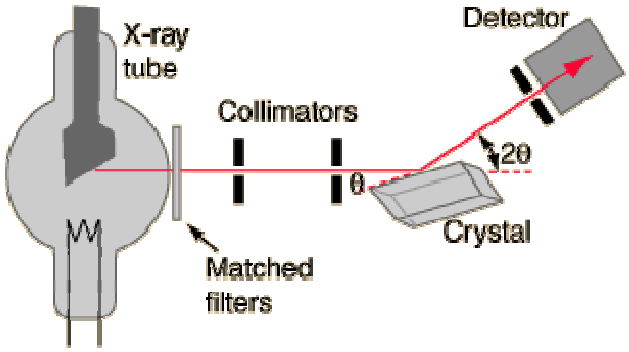

Figure 8.2. *A schematic view of X-Ray Diffraction [3].*

X-ray diffraction yields the atomic structure of materials and is based on the elastic scattering of x-rays from the electron clouds of the individual atoms in the system. The most comprehensive description of scattering from crystals is given by the dynamical theory of diffraction. This technique has been used in two forms for single-crystal and powder samples:
Single-crystal x-ray diffraction is a technique used to solve the complete structure of crystalline materials, ranging from simple inorganic solids to complex macromolecules, such as proteins.
Powder diffraction (XRD) is a technique used to characterize the crystallographic structure, crystallite size (grain size) and the preferred orientation in polycrystalline or powdered solid samples [4].
Herein, x-ray diffraction patterns were recorded with a Bruker AXS D8 Advance diffractometer equipped with a SolX energy dispersive detector in reflection mode using unfiltered MoKα radiation. Samples were prepared between two layers of Scotch ® Magic tape.

8.3. Superconducting Quantum Interference Device

A **SQUID** is a very sensitive magnetometer used to measure extremely weak magnetic fields, based on superconducting loops containing Josephson junctions.
SQUIDs are sensitive enough to measure fields as low as 5 aT (5×10^{-18} T) within a few days of averaged measurements. Their noise levels are as low as 3 $fT\cdot Hz^{-½}$. For comparison, a typical refrigerator magnet produces 0.01 tesla (10^{-2} T) and some processes in animals produce very small magnetic fields between 10^{-9} T and 10^{-6} T. Recently invented SERF atomic magnetometers are potentially more sensitive and do not require cryogenic refrigeration but are orders of magnitude larger in size (~1 cm^3) and must be operated in a near-zero magnetic field. Figure 8.3 show the function a SQUID in the presence of a magnetic field.
There are two main types of SQUID: direct current (DC) and radio frequency (RF). RF SQUIDs can work with only one Josephson junction, which might make them cheaper to produce, but are less sensitive [5].

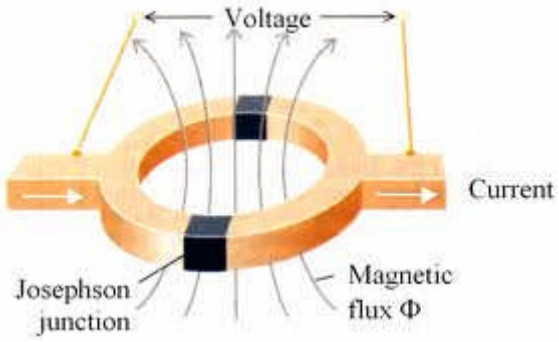

Figure 8.3. *Superconducting Quantum Interference Device scheme.*

The magnetic properties of powder samples in this thesis were measured with a superconductive quantum interference device (SQUID, Quantum Design MPMS XL).

8.4. Mössbauer

Mössbauer spectroscopy is a spectroscopic technique based on the mössbauer effect. This effect consists in the recoil-free, resonant absorption and emission of gamma rays in solids. Like NMR spectroscopy, mössbauer spectroscopy probes tiny changes in the energy levels of an atomic nucleus in response to its environment. Typically, three types of nuclear interaction may be observed: an isomer shift, also known as a chemical shift; quadrupole splitting; and, magnetic or hyperfine splitting, also known as the Zeeman effect. Due to the high energy and the extremely narrow line widths of gamma rays, mössbauer spectroscopy is one of the most sensitive techniques in terms of energy (and hence frequency) resolution, capable of detecting change in just a few parts per 10^{11}. It is formed by three main parts; a source that moves back and forth to generate a doppler effect, a collimator that filters out non-parallel gamma rays and a detector (Figure 8.4).

During mössbauer absorption spectroscopy, the source is accelerated through a range of velocities using a linear motor to produce a Doppler effect and scan the gamma ray energy through a given range. A typical range of velocities for ^{57}Fe, for example, may be ±11 mm/s (1 mm/s = 48.075 neV). In the resulting spectra, gamma ray intensity is plotted as a function of the source velocity. At velocities corresponding to the resonant energy levels of the sample, a fraction of the gamma rays are absorbed, resulting in a drop in measured intensity and a corresponding dip in the spectrum. The number, positions and intensities of the dips (also called peaks; dips in transmitted intensity are peaks in absorbance) provide information about

the chemical environment of the absorbing nuclei and can be used to characterize the sample [6].

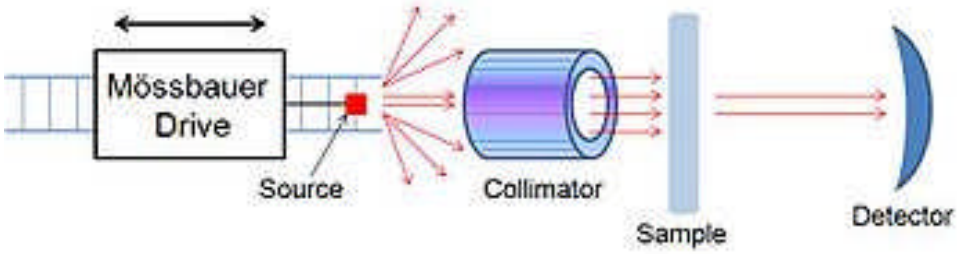

Figure 8.4. *A schematic view of Mössbauer Spectrometer.*

Mössbauer spectra were obtained at room temperature, 110 K, 80 K and 4.2 K with a constant acceleration transmission mössbauer spectrometer and ^{57}Co (Rh) source in this doctoral dissertation.

8.5. Magnetic Resonance Imaging

MRI is a medical imaging technique used in radiology to visualize detailed internal structures. MRI makes use of the property of nuclear magnetic resonance (NMR) to image the nuclei of atoms inside the body.

An MRI machine uses a powerful magnetic field to align the magnetization of some atoms in the body and radio frequency fields to systematically alter the alignment of this magnetization. MRI provides good contrast between the different soft tissues of the body, which makes it especially useful in imaging the brain, muscles, the heart and cancers compared with other medical imaging techniques such as computed tomography (CT) or x-rays.

The body is largely composed of water molecules. Each water molecule has two hydrogen nuclei or protons. When a person is inside the powerful magnetic field of the scanner, the magnetic moments of some of these molecules become aligned with the direction of the field. A radio frequency transmitter is briefly turned on, producing a further varying electromagnetic field. The photons of this field have just the right energy, known as the resonance frequency, to be absorbed and flip the spin of the aligned protons in the body. The frequency at which the protons resonate depends on the strength of the applied magnetic field. After the field is turned off, those protons, which absorbed energy, revert to the original

lower-energy spin-down state. Now a hydrogen dipole has two spins, 1 high spin and 1 low. In low spin both dipole and field are in parallel direction and in high spin case it is anti parallel. They release the difference in energy as a photon and the released photons are detected by the scanner as an electromagnetic signal, similar to radio waves [7].

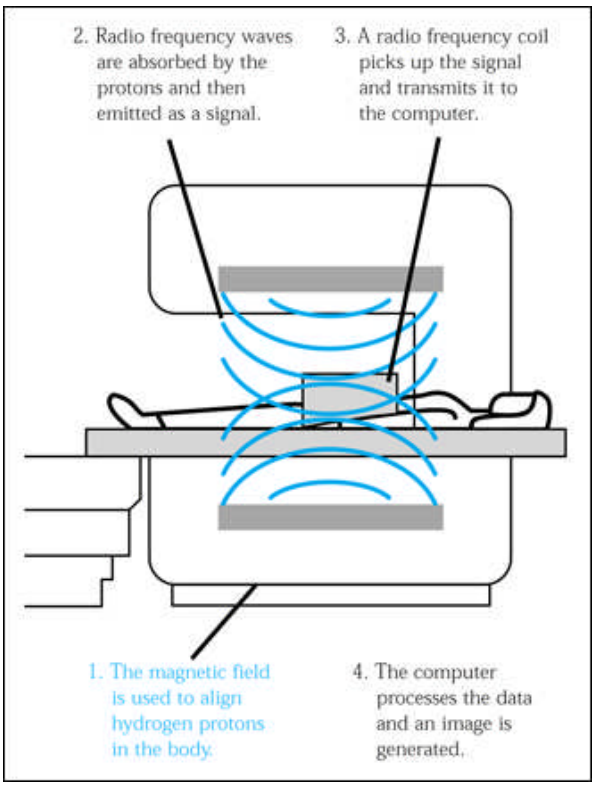

Figure 8.5. *Magnetic Resonance Imaging [8].*

In order to measure the magnetic resonance imaging, different concentrations of polymer functionalized nanoparticles were performed on a clinical 3.0 Tesla scanner (Magnetom Trio, Siemens Medical Solutions, Erlangen, Germany) in this doctoral thesis.

8.6. References

[1] http://en.wikipedia.org/wiki/Transmission_electron_microscopy

[2] http://teacherschoice.files.wordpress.com/2010/12/electron-microscopy1.pdf

[3] L. Reimer, *Energy-Filtering Transmission Electron Microscopy*; Springer: Berlin, **1995**.

[4] http://hyperphysics.phy-astr.gsu.edu/hbase/quantum/bragg.html

[5] http://en.wikipedia.org/wiki/X-ray_scattering_techniques

[6] http://en.wikipedia.org/wiki/SQUID

[7] http://en.wikipedia.org/wiki/M%C3%B6ssbauer_spectroscopy

[8] http://en.wikipedia.org/wiki/Magnetic_resonance_imaging

[9] http://www.bitterrootimaging.com/MRI-workings.html

9. Appendix

9.1. List of Figures

concentrations of nitric acid (HNO_3) ranging from 5-250 μM (final concentration). A clear increase on NO is observed in the presence of higher concentrations of HNO_3. (b) Keeping HNO_3 concentration constant(10 μM final concentration) and varying the $Cu@Fe_3O_4$ heterodimers concentration. (1-100 μg). Again, a clear increment is observed in a nanoparticle dependent manner. Inset: digital image of a solution containing 10 μM of HNO_3 and 100 μg of $Cu@Fe_3O_4$ (slightly alkaline pH) under a UV lamp (excitation 365 nm). A bluish fluorescence is observed. (c) Magnetic properties of $Cu@Fe_3O_4$ nanoparticles for recovering after the reaction by making use of Fe_3O_4 domain. (d) Cycles of reutilization of nanoparticles for the formation of nitric oxide (NO). A significant decrease can be observed during consecutive cycles.

Figure 2.10. T_1 and T_2-weighted MRI images of solutions containing polymer functionalized $Cu@Fe_3O_4$ nanoparticles (concentrations in mM) with cloverleaf and cube shaped morphologies, respectively.

Figure 3.1. (a) TEM image of a representative sample and (b) HRTEM image of two individual copper ferrite nanoparticles (the inset shows the electron diffraction pattern). (c) Particle size distribution obtained by averaging the sizes of approx. 100 nanoparticles.

Figure 3.2. XRD diffraction pattern (black), Rietveld-refinement (blue) and difference curve (red) of "$CuFe_2O_4$" (Bragg maxima at $2\Theta \approx 21°$ are due to the (220) reflection of the Si single crystal used a sample holder).

Figure 3.3. (a) Hysteresis loop of $CuFe_2O_4$ nanoparticles, (b) temperature dependence of magnetization in field cooling (FC) and zero field cooling (ZFC).

Figure 3.4. ^{57}Fe Mössbauer spectra of a nanopowder $Cu_xFe_{3-x}O_4$ recorded at (a) 295 K, (b) 80 K and (c) 4.2 K.

Figure 3.5. (a) Schematic representation of multifunctional copolymer containing 3-hydroxytyramine (dopamine) as an anchor group for the binding of metal oxides, pip-NBD as a fluorophore and PEG chains containing amine group to improve the solubility of functionalized nanoparticles. (b) Digital photograph of $Cu_xFe_{3-x}O_4$ solutions before (left) and after (right) ligand exchange in hexane (top layer) and in water (bottom layer). (c) Fluorescence microscope images of NBD-polymer functionalized $Cu_xFe_{3-x}O_4$ nanoparticles (green fluorescence).

Figure 3.6. T_1 and T_2 weighted MRI images of solutions containing polymer functionalized $Cu_xFe_{3-x}O_4$ nanoparticles (concentrations in mM Fe).

Figure 4.1. (a & b) Transmission electron microscopy (TEM) and high resolution (HRTEM)

images of $Co@Fe_2O_3$ NPs with rhombohedral Fe_2O_3 domain. (c & d) Overview TEM image and HRTEM image of $CoFe_2O_4$ NPs.

Figure 4.2. STEM mode images and EDX line scan of $Co@Fe_2O_3$ heterodimer and ternary phase $CoFe_2O_4$ nanoparticles. (a) STEM mode image of $Co@Fe_2O_3$ heterodimer nanoparticles where cobalt shows a bright spot and also Fe_2O_3 shows a dark contrast (b) corresponding EDX line scan, which confirms that bright spot cobalt and also confirms the presence of iron and oxygen for less bright nanoparticles. (c) STEM mode image of $CoFe_2O_4$ nanoparticles and (d) the corresponding line scan EDX, which confirm that cobalt is distributed uniformly.

Figure 4.3. Selected electron diffraction pattern of $CoFe_2O_4$ nanoparticle.

Figure 4.4. $Co@Fe_2O_3$ nanoparticles after (a) 15 min, (b) 1 h at 245°C and (c) $CoFe_2O_4$ nanoparticles after 1 h at 245°C.

Figure 4.5. (a) Rietveld plot of $Co@Fe_2O_3$ NPs (red dots: experimental pattern, black line: calculated pattern, red line: difference, black ticks: reflection positions, observed and calculated pattern are shifted for clarity). (b) Rietveld plot of $CoFe_2O_4$ NPs (red dots: experimental pattern, black line: calculated pattern, red line: difference, black ticks: reflection positions).

Figure 4.6. Magnetic hysteresis loops at 5 K and 300 K and (a) $Co@Fe_2O_3$ heterodimers (b) $CoFe_2O_4$ NPs. Temperature dependence of the magnetization in field-cooling (FC) and zero-field-cooling (ZFC) mode are given in insets.

Figure 4.7. ^{57}Fe Mössbauer spectra of (a) $CoFe_2O_4$ NPs recorded at 295 K (b) at 110 K and (c) $Co@Fe_2O_3$ nanodimers recorded at 80 K.

Figure 4.8. (a) Scheme of polymeric ligand. (b) Digital photograph of $Co@Fe_2O_3$ solutions before (left) and after (right) surface functionalization in hexane (top layer) and in water (bottom layer).

Figure 4.9. (a & b) T_1 and T_2-weighted MRI images of solutions containing polymer functionalized $CoFe_2O_4$ and $Co@Fe_2O_3$ NPs (concentrations in mM).

Figure 5.1. Transmission electron microscopy (TEM) images: (a) nickel and (b) $Ni@Fe_2O_3$ heterodimer nanoparticles. (c) STEM mode image of $Ni@Fe_2O_3$ heterodimer nanoparticles where nickel shows a bright spot and also Fe_2O_3 shows a dark contrast (d) corresponding EDX line scan which confirms the presence of nickel, iron and oxygen.

Figure 5.2. XRD diffraction pattern of a bulk sample of $Ni@Fe_2O_3$ heterodimer nanoparticle (red dots: observed, black line: calculated, red line: difference, black tics mark the reflection positions of the constituent phases).

Figure 5.3. (a) Magnetic hysteresis loops at 5 K and 300 K. (b) Temperature dependence of the magnetization in field-cooling (FC) and zero-field-cooling (ZFC) for Ni@Fe_2O_3 nanoparticles.

Figure 5.4. ^{57}Fe Mössbauer spectra of Ni@Fe_2O_3 nanoparticles at room temperature, 150K, 87.5K, and 4.2K.

Figure 5.5. Schematic representation of multifunctional copolymer containing 3-hydroxytyramine (dopamine) as an anchor group and PEG chains containing amine group.

Figure 5.6. (a) Digital photograph of Ni@Fe_2O_3 solutions before (left) and after (right) ligand exchange in hexane (top layer) and in water (bottom layer). (b) Digital image of the magnetic properties of Ni@Fe_2O_3 NPs. (c) Time course UV-Vis scans of the transformation of the bromophenol blue (4.6 μM) in the presence Ni@Fe_2O_3 NPs (0.02 mg/mL). The reaction was measured for 6h at room temperature. A decrease of the band at 590 nm is clearly observed to be time dependent. Upper inset: digital image of reaction vial where initial blue coloration typical from bromophenol blue is observed at time 0. Lower inset: digital image of reaction vial where loss of coloration occurs after 6h of reaction. (d) Catalyst reutilization capacity was accessed through consecutive cycles (7 in total). The supernatant was retrieved and the absorbance measured at 590 nm. An increase of absorbance is clearly observed.

Figure 5.7. Control experiments. Ni (5 nm) and Fe_2O_3 NPs (10 nm) were independently mixed with bromophenol blue solution (4.6 μM) and left to react for 6h at room temperature. (a) Ni NPs induced decoloration of the initial blue solution. (b) Fe_2O_3 NPs did not suggesting that the decoloration transformation is really due to the Ni part of the Ni@Fe_2O_3 NPs.(c) Ni@Fe_2O_3 NPs (0.02mg/mL) were mixed with a phosphate-containing solution (pH 7.2) for 30 min at room temperature. The nanoparticles were washed by making used of their magnetic properties and resuspended in distilled water to obtain the initial concentration. Afterwards, the nanoparticles were mixed with bromophenol blue solution (4.6 μM) and left for 6 h at room temperature. The solution remained with the same blue coloration.

Figure 6.1. (a) TEM image of Pt@Fe_3O_4 nanoparticles and (b) HRTEM image of an individual nanoparticle.

Figure 6.2. Elemental mapping of synthesized dumbbell-like Pt@Fe_3O_4 heterodimer. (a) STEM mode image and corresponding elemental maps of Pt (yellow), Fe (orange) and O (red) obtained by recording spatial distribution. (b) EDS line scan profiles confirm the presence of platinum, iron and oxygen.

Figure 6.3. X-ray diffraction patterns of Pt@Fe_3O_4 nanoparticles.

9.2. List of Schemes

9.3. Abbreviations

NPs	Nanoparticles
MNPs	Magnetic Nanoparticles
PEG	Poly Ethylene Glycol
PFA	Pentafluorophenyl acrylate
NO	Nitric Oxide
FC	Field Cooling
ZFC	Zero Field Cooling
DAN	2,3-Diaminonaphthalene
NBD	7-nitrobenzofurazan

9.4. Supplementary Information

Mössbauer Data

Sample	CS (mm/s)	Δ (mm/s)	H (kOe)	w_+
$Cu@Fe_3O_4$	0.25(1)	0	488(2)	0.28(2)
nanocubes	0.57(1)	0	452(2)	0.41(2)
$Cu@Fe_3O_4$	0.28(1)	0	485(2)	0.31(2)
asymmetric	0.60(1)	0	448(2)	0.36(2)

Appendix 1. *Mössbauer data.*

Light Scattering

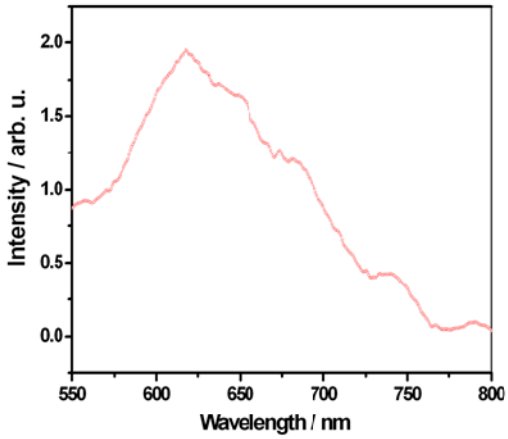

Appendix 2. *Typical scattering spectrum of a single cube shaped $Cu@Fe_3O_4$, revealing a resonance wavelength of approximately $\lambda res \approx 620$ nm.*

FT-IR

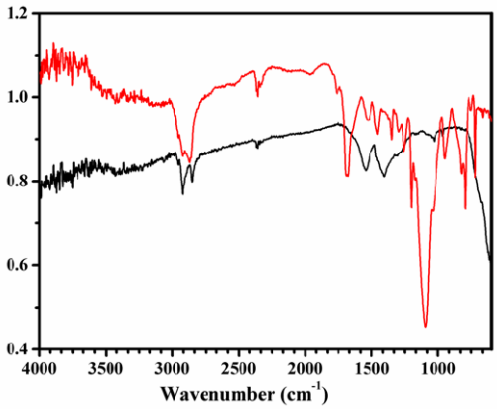

Appendix 3. *FT-IR spectra of as synthesized* $Cu_xFe_{3-x}O_4$ *nanoparticles (black line) and polymeric ligand functionalized nanoparticles (red line).*